Fundamental Studies of Organic Silicon Combustion Chemistry and Characterizing the Presence of Silicon Species in Landfill and Sludge Gas

by

Qinghui Meng

A dissertation submitted in partial fulfillment
of the requirements for the degree of
Doctor of Philosophy
(Mechanical Engineering)
in the University of Michigan
2023

Doctoral Committee:

Professor Margaret S. Wooldridge, Chair
Professor Krzysztof J. Fidkowski
Associate Professor Mirko Gamba
Dr. Robert S. Tranter, Argonne National Laboratory
Professor Angela Violi

Qinghui Meng

mqh@umich.edu

ORCID iD: 0000-0001-8604-6189

Dedication

I dedicate this Ph.D. thesis to my beloved family and friends, whose unwavering love and boundless encouragement have been the pillars of strength sustaining me through this academic journey. Your belief in me during moments of self-doubt and the countless lessons I've learned from each of you have shaped not only this work but also the person I have become.

Acknowledgements

This Ph.D. journey has marked a distinct period in my life. Navigating life away from home, adapting to an entirely new environment, and enduring the challenges of a worldwide pandemic, I recognize that I would not have been able to complete this transformative journey without the support of numerous individuals. I extend my heartfelt gratitude to those who have directly contributed to my work, providing technical expertise, as well as those who have offered emotional and life support.

Foremost, I express my deepest appreciation to my advisor, Professor Margaret Wooldridge, for her unwavering guidance, mentorship, and boundless support throughout the entire research process. Her expertise, encouragement, and invaluable insights have not only shaped the trajectory of this study but have also molded me into a capable researcher.

My gratitude extends to both current and former labmates, whose collaboration and camaraderie have made the research environment both stimulating and enjoyable. The shared experiences, discussions, and collective efforts have undeniably enriched my Ph.D. journey.

I also wish to convey my sincere appreciation to collaborators at Argonne National Lab, including Dr. Robert Tranter, Dr. Colin Banyon, Dr. Alan Kastengren, and Dr. Keunsoo Kim. Working with them has been a special and unforgettable experience, and conducting experiments at the Advanced Photon Source has not only enriched the technical aspects of this research but has also provided a unique learning opportunity.

Special acknowledgment goes to the members of my dissertation committee, Professor Margaret Wooldridge, Professor Krzysztof Fidkowski, Professor Mirko Gamba, Dr. Robert Tranter, and Professor Angela Violi, for their time, expertise, and constructive feedback. Their insights have been pivotal in refining the focus and depth of this research, fostering a deeper and broader reflection on my work. I am particularly grateful to Professor Mirko Gamba and his student Rahul Ramesh for lending their flame speed measurement instrument and sharing their knowledge and expertise.

Heartfelt thanks are extended to the Mechanical Engineering staff for their administrative support and assistance throughout my academic journey. Their professionalism and efficiency have greatly facilitated the logistical aspects of this research. Special appreciation goes to electronics technician Aaron Borgman from Aerospace Engineering for his exceptional support and education in building essential electronics for my work.

I would also like to extend my thanks to local landfill-gas-to-energy operators, who provided valuable information for this research and allowed me to collect gas from their sites for analysis.

To my dear friends, both within and outside the academic sphere, thank you for being a source of encouragement, understanding, and laughter. Your friendship has added immeasurable joy to this challenging endeavor. Many of you have be my peer mentors and has great influence on my personal growth.

Last but certainly not least, I owe an immeasurable debt of gratitude to my family. Their unconditional love, unwavering support, and belief in my abilities have been the bedrock upon which this academic achievement stands. Their sacrifices and encouragement have been my driving force.

This journey would not have been possible without the collective contributions of each individual mentioned. Thank you all for being an integral part of this significant milestone in my academic and personal growth.

Funding Acknowledgements:

Table of Contents

List of Tables

List of Figures

List of Appendices

Abstract

Organic silicon species play important roles as reactants in waste-to-energy systems and in material synthesis processes. This research addresses some of the critical challenges posed by silicon species in biogas, which hinder energy recovery due, in part, to silica production during combustion. Despite over a decade of recognizing the impact of silicon compounds on biogas utilization, comprehensive characterization of their presence in biogas is lacking. In addition, understanding combustion chemistry of silicon compounds is essential to evaluate and mitigate their impacts on biogas combustion and improve material synthesis, but detailed reaction mechanisms and thermochemistry data of these chemicals remain scarce and have high uncertainties and known discrepancies with experimental observations.

This study aims to fill key knowledge gaps by advancing the understanding of silicon species including their presence in biogas and fundamental combustion chemistry of some canonical compounds. The technical approach for characterizing waste-to-energy concerns included statistical analysis of biogas data reported in the literature, on-site analysis at landfill gas energy facilities, and qualitative interviews with waste-to-energy stakeholders. For advancing the reaction chemistry, flat flame burners and ignition studies were used. The fundamental laboratory combustion experiments focused on trimethylsilanol (TMSO) and hexamethyldisiloxane (HMDSO) due to the canonical structure of these silicon compounds. Burner studies leveraged well-established initial and boundary conditions and novel application of recent diagnostic advances to measure in situ temperature at unprecedented spatial resolution. The ignition studies

leveraged the simplified geometry and well-established data interpretation methods to consider chemistry effects on flame speeds.

Key outcomes of this work include a new database on silicon species concentrations in biogas. The longitudinal study showed widespread presence of silicon species in global and U.S. biogas systems. TMSO, octamethylcyclotetrasiloxane (D4) and decamethylcyclopentasiloxane (D5) were identified as sentinel species, where their concentrations were identified correlated with total silicon species concentrations. The database established in this work provide an important quantitative foundation for technology development to recover silicon species from biogas and to develop methods for silica abatement and mitigation. In addition, the new correlations discovered between specific and total silicon species concentrations provide new opportunities for developing methods to monitor silicon species and potentially improve waste-to-energy facilities, e.g., by reducing maintenance costs associated with mitigating the presences of these species in biogas.

In laboratory burner studies, x-ray fluorescence (XRF) spectroscopy was applied to measure the in-situ temperature fields for the first time in flames with silicon reactants. Findings provide direct insight into the reaction pathways consuming TMSO and HMDSO. Specifically, TMSO and HMDSO reactions were initiated in low-temperature low-oxygen regions. The results indicate radicals from the methane flame system initiate reactions with TMSO and HMDSO through H-abstraction pathways. Additionally, gas sampling measurements identified TMSO as an intermediate of HMDSO reactions, contrary to recently proposed reaction mechanisms in the literature. Surprisingly, the flame speed measurements showed no significant impact from HMDSO on methane flame speeds at the conditions studied, suggesting transport effects may dominate the HMDSO chemistry. The results are the first attempt to measure siloxane flame speeds and provide important knowledge on how to conduct further measurements in the future with

improved accuracy. The original findings of the burner and ignition studies provide new insights into the combustion chemistry of silicon species (namely the radical interaction and production pathways), and provide quantitative data to further advance reaction theory and kinetics.

Chapter 1 The Importance of Organic Silicon Species in Engineering Systems

1.1 Introduction

Biogas from waste sources, such as landfill gas and sludge gas from waste water treatment plants, is a sustainable energy resource. With the need to reduce fossil fuel usage and the associated carbon emissions, increasing energy production from waste gas sources is a great way to displace fossil fuel use and mitigate the impact from landfills and waste water treatment plants. Energy production from waste-based biogas can simultaneously benefit multiple areas such as renewable energy production, greenhouse gas emissions reduction and waste management. However, the successful and economical utilization of landfill and sludge gas has been challenged by their complicated compositions [1]-[3], especially components such as hydrogen sulfide and organic silicon species. While hydrogen sulfide is widely treated in the preprocessing of the biogas, organic silicon species such as silanols and siloxanes are typically not treated in biogas because complete removal of those chemicals can be difficult and costly [4][5]. The major problem caused by silicon species in biogas is the formation of silica particles during oxidation. In combustion-based energy production processes from biogas, silica particles formed in the flame will quickly deposit on internal surfaces of the combustion equipment [6]-[8]. With the accumulation of silica deposits, the efficiency of energy production is affected [9][10], and with time silica can damage combustion facilities [11].

Prior work on siloxanes in biogas[1] include case studies on siloxane concentrations [12]-[15], impacts on combustion facilities [7][8][11][16], experimental tests on siloxane removal efficiency [17]-[20], as well as review studies on siloxane removal techniques and economic analysis [5][21]-[23]. The results from these studies have shown that siloxanes have been observed in biogas for nearly two decades and have created obstacles for energy production from biogas. To be specific, there are multiple ways that siloxanes can affect the combustion facilities, including damage caused by abrasive silica particles [24][25], the failure of combustion sensors [7], soft paste residuals in engines damaging surfaces and adversely effecting engine performance and contamination of lubricant oils [11] increasing maintenance costs and frequency. And although there are techniques for siloxane removal such as adsorption, absorption, condensation and etc. [22][23][26], applying the methods and technologies in real world operations is limited, primarily due to the high costs required by biogas pretreatment systems[5].

The exiting studies of siloxane concentrations, impacts and removal technologies provide a foundation for qualitative understanding that the presence of siloxanes is a problem in several systems. What is missing from the current literature is a quantitative understanding of the presence of siloxanes in biogas. Moreover, trends in concentrations of each silicon species are not available and can provide additional insight into the chemistry forming siloxanes in biogas, how and which species to monitor to assess concentrations, and other key parameters required for designing use and mitigation technologies. It is also valuable to understand siloxanes' worldwide occurrence in biogas in order to address their overall negative impacts on global applications of the waste-to-energy industry. As the results of the current thesis will show, the substantial variation in siloxane

---

[1] For convenient, in this dissertation, when biogas is mentioned, it specifically refers to biogas from waste sources such as landfill and sludge gas; in addition, when refer to the word 'siloxanes', it represents all typical silicon species in biogas including trimethylsilanol, linear and cyclic siloxanes as listed in **Table 2.1** in **Chapter 2**.

concentrations from different sites motivates statistical analysis to reveal patterns and relationships, which help formulate strategies for their monitoring, prevention, and removal.

Besides the limited comprehensive knowledge on the presence of siloxanes in biogas, there are also gaps in understanding the combustion chemistry of siloxanes. Prior works have used hydrocarbon analogies as initial efforts to propose reaction pathway [27]-[29]. In some circumstances, hydrocarbon analogy can provide insight on siloxane reactions, such as the initial H-abstraction mechanism and final pyrolysis products. However, because of the fundamental difference in bonding between silicon and carbon, the elementary reaction chemistry is quite different. For example, the chemical bond energy between silicon-based bonds and carbon-based bonds are quite different, and reaction mechanisms developed from hydrocarbon analogy do not capture siloxanes reaction behavior, particularly of intermediate species formed [30]. Previous experimental studies have observed unique combustion phenomenon for siloxane species [31][32], and there are some proposed siloxane pathways which captures the experimental phenomenon [33]. However, most of the experimental studies have been limited to a small parametric space of state conditions, and diverse experimental methods can dramatically advance siloxane reaction chemistry and provide a missing foundation to the theory of siloxane pyrolysis and oxidation chemistry. The current work addresses this gap in fundamental siloxane chemistry using different experimental methods to amplify the effects of siloxanes in methane combustion systems. The new data provide the basis for hypothesizing new reaction pathways and provide the basis for validation of theory in the future. The experimental methods and outcomes presented in this work are all new and original and were selected to leverage the strengths of the facilities and methods. For example, x-ray diagnostics provide new vital in-situ temperature measurements of flames that have been well studied previously using other diagnostics. Thus, the new temperature measurements provide

new data that complement and leverage prior work. Consequently, new reaction pathways can be theorized based on the combined information – reaction pathways that could not have been previously conjectured without the new data.

The overall goal of this dissertation is to advance the understanding necessary to improve outcomes from waste-to-energy facilities and related applications that use siloxane and silanol compounds. This objective is met by quantitatively evaluating the presence of silicon species in landfill gas and sludge gas, and through studies aimed at elucidating the fundamental chemistry controlling oxidation and pyrolysis of organic silicon compounds.

1.2 Silicon Compounds as An Emerging Problem in Waste-to-Energy Processes

Organic silicon species have been observed in landfill gas and sludge gas for many years all over the world [9][12][14][34]-[38] and the damage these compounds have on combustion equipment has been widely studied. In the 2004 SWANA Landfill Gas Symposium, Wheless et al. [4] reported siloxane concentrations observed in landfill gas, reviewed sampling and measurement methods, reviewed removal techniques and summarized the cost of removal. This work mentioned that silicon compounds not only affect the combustion equipment, but they can also cause failure of catalysts for post-combustion emission treatment. Dewil et al. [9] reviewed the atmospheric chemistry of siloxanes and the fate of the chemicals during wastewater treatment. Dewil et al. showed the dramatic effect of how burning a siloxane rich gas clogged a boiler. Nair et al. [10] studied the impact of siloxane on an internal combustion engine experimentally, and found that silica particles formed by siloxane oxidation covered the engine internal surfaces (piston heads, oxygen sensors and spark plugs) and collected in the engine oil. In another study by Nair et al. [7] on a residential furnace, silica particles were found accumulated on the furnace surfaces (flame sensors, condenser coils and tailpipes) and in the water condensed on the flue vent. Álvarez-Flórez

et al. [11] analyzed several types of damage in internal combustion engines caused by siloxanes, including silica layer formed on combustion chamber surfaces, scratches and soft residuals on cylinder liners, damage to piston heads and erosion in compressor blades. Álvarez-Flórez et al. mentioned the damage was mainly caused by the thin layer of silica deposits formed on surfaces and the soft paste formed by reactions between the silicon compounds and engine oil or methane. Recently, Yang et al. [16] studied the effect of organic silicon species on landfill gas dioxygen catalysts, and Konkol et al. [8] and Östürk et al. [24] investigated the elements in the deposits formed during biogas utilization in engines.

Previous studies have discovered the negative impact of silicon chemicals in biogas, and some of them have reported siloxane concentrations at specific sites. However, there are only a few reviews which summarize the findings in the past literature [1][26], and there remains a lack of systematic analysis on the information reported in past literature. Considering the large number of on-going and planned waste-to-energy projects, it is beneficial to have a systematic review and statistical analysis that describes the presence and trends of silicon compounds in landfill gas and sludge gas.

Despite the issues caused by siloxanes in the waste-to-energy process, these compounds are valuable chemicals as precursors for silicon material synthesis [39]. In addition, trimethylsilanol (TMS) and hexamethyldisiloxane (L2) are highly energetic and ignitable. Past studies have discovered that TMS and L2 can reduce the ignition delay time of syngas [32][33]. If the amount of silicon chemicals in biogas continuously increase, harvesting the chemicals from biogas and reusing them as particle synthesis precursors or combustion additives can be another value-added pathway for waste systems.

Either for understanding and mitigating impacts caused by silicon compounds in waste-to-energy process or for evaluating these chemicals as a potential resource, it is necessary to have a clear understanding of the presence and trends of siloxanes in biogas. While many studies have documented local issues and concerns regarding silicon-containing compounds on waste gas (e.g., specific assessment of total silicon levels, etc.), to date there are no attempts to integrate the data in the literature and to summarize the past and expected trends. Therefore, one objective of this study was to systematically and quantitatively assess the types and trends of silicon species found in biogas. **Chapter 2** of this thesis achieved this goal through analyzing the concentrations of siloxanes in the literature and industrial reports, including total siloxane concentrations at different regions in the world, the publication year of the data, statistical analysis of correlations between specific species, and etc. In addition, local landfill sites operators were interviewed and their concerns toward siloxanes were recorded. Furthermore, siloxane concentrations in landfill gas from two landfill sites located in the Midwest of U.S. were measured over a period of two years and the data are reported and compared with the literature in this chapter.

1.3 Combustion Effects and Chemistry

Chapter 2 demonstrated that the siloxane chemicals have become a critical issue in biogas-to-energy processes. Since the majority of biogas-to-energy projects utilize combustion-based method, it is important and valuable to study the combustion phenomenon and chemistry of silicon-based compounds.

Most studies for silicon chemical reactions are focusing on their roles as precursors for silica particle synthesis. Therefore, a large amount of work studies the $SiO \rightarrow SiO_2$ chemistry [29][30][40][41]. In those papers, the initial reactions of the silicon compounds/precursors were usually simplified and are not considered accurate representations of the elementary chemistry.

For example, in the experimental study on counterflow methane-air flames with HMDSO in 1996, Chagger et al. [29] suggested a simplified HMDSO oxidation path starting with HMDSO decomposition reactions with OH, O_2 and HO_2 radicals into C_3H_9SiO, following by a further decomposition of C_3H_9SiO into SiO. Chagger et al. [29] used hydrocarbon analogies to estimate the reaction rates of HMDSO decompositions and stated that the greatest uncertainty was related to the decomposition reactions. In 2017, Feroughi et al. [30] used both experimental and numerical methods to study SiO_2 formation in a HMDSO-seeded hydrogen-oxygen flat flame, using laser-induced fluorescence to measure gas phase silicon oxide (SiO) in the flame. The simulation was focused on reaction paths from SiO to SiO_2 developed by Miller et al. [41][41], Britten et al. [42] and Zachariah et al. [43], and the initial reactions of HMDSO were represented by a one-step global reaction $HMDSO + OH \rightarrow 2SiO + 6CH_3 + H$. The results of this work show that simulated SiO profile does not predict the experimental SiO data, and Feroughi et al. [30] have proposed that this could due to the simplified HMDSO reaction path. Both of the studies show the proposed simplified HMDSO decomposition paths do not accurately describe the real reaction pathways, which directly and therefore impacts the prediction of subsequent SiO and SiO_2 reactions.

Due to the insufficiency of using simplified siloxane reaction models, recent studies put more effort on studying the initial reactions of siloxanes. Mansfield et al. [32] observed that 100 ppm TMSO added to syngas reduced the syngas autoignition time in a rapid compression facility (RCF) by 50-70 % at 15 atm and proposed the promoting effect is related to HO_2 kinetics. Schwind et al. [31][33] extended this study to HMDSO and observed that HMDSO had a similar promoting effect on syngas autoignition delay times. Schwind et al. proposed the reaction of HMDSO is initiated by H-abstraction by free radicals, followed by $R \rightarrow RO_2 \rightarrow QOOH$ paths which produced OH radicals promoting syngas ignition. In the recent study by Karakaya et al. [44] in 2023, initial

reactions of TMSO were proposed by using quantum chemistry calculations, and more information on metastable nanoparticles in the flame were provided. Karakaya et al. [44] proposed TMSO reactions are initiated by H-abstraction by interactions with OH, H and O radicals, followed by two major reaction paths including the abstraction of CH_3 radicals and addition of O_2. Both Schwind et al. [33] and Karakaya et al. [44] have proposed H-abstraction mechanisms for siloxane oxidations. In addition, reactive force field (ReaxFF) molecular dynamics simulations by Huang et al. [45] proposed a detailed HMDSO reaction sequence. However, the reaction mechanism in the work by Huang et al. is not fully consistent with the pathways proposed by Schwind et al. In summary, a consistent reaction mechanism, describing TMSO and HMSDO combustion chemistry both qualitatively and quantitatively is still missing from the literature. And, there is a critical lack of validation data and experimental measurements that can be used to propose theory and validate mechanisms and thermochemistry data.

In terms of prior work on siloxane pyrolysis chemistry, there are few experimental studies documenting few observable results. Cherneshev et al. [46] used gas-liquid chromatography and mass spectroscopy to study HMDSO pyrolysis at temperatures 948 K in a hollow quartz tube, and suggested the reactions were dominated by the dissociation of Si-O bonds and formation of dimethylsilanone ($C_2H_6Si=O$), followed by formations of larger linear and cyclic siloxane groups. In addition, Almond et al. [47] studied vacuum (10^{-3}-10^{-4} torr) pyrolysis of linear and cyclic siloxanes at 1000 K in a silica chamber and also proposed that the formation of dimethylsilanone is the favored pathway for decomposition of larger siloxane species. However, the experimental methods used by these two works have relatively long residence times for the siloxane species compared with the time scales found in combustion chemistry, bringing into question the relevance and applicability to combustion systems. The residence time for HMDSO in the experiments by

8

Cherneshev et al. [46] was 30 s in the reactor. In the work by Almond et al. [47], the authors used infrared spectroscopy to measure the composition of condensed products on a cesium iodide window. The spray time for condensed product formation was 60-90 mins. To obtain information on siloxane pyrolysis products at combustion relevant conditions, Schwind et al. [33] conducted shock tube pyrolysis studies for TMSO and HMDSO and proposed possible pathways including the formation of dimethylsilanone. Other pyrolysis pathways for HMDSO include production of CH_3 radicals through dissociation of Si-C bond, production of H radicals through dissociation of C-H bond, formation of TMSO and $(CH_3)_2Si=CH_2$, and production of H_2 through dissociation of C-H bonds on two methyl groups. None of the previous studies above have suggested any Arrhenius kinetic rates for the decomposition reactions or confirmed dominant reaction pathways. In a recent work in 2022, Chen et al. [48] completed ReaxFF simulations on HMDSO pyrolysis at 2500 K and 3000 K, providing insights on possible Si-containing fragments formed in the process. As the results presented in this thesis will show, a major pathway in this work is proposed to be the production of CH_3 radicals through dissociation of the Si-C bond. This path is included in the pathways proposed by Schwind et al.; however, other important paths including the formation of dimethylsilanone and TMSO have not been proposed previously.

In conclusion, even with the efforts and progress made by previous studies, the relevant thermochemistry data and reaction mechanism of siloxane and silanol oxidation are still limited and have not been well validated. The interactions of silicon organic species with methane reactions also remain unclear and this gap is particularly problematic for biogas utilization. Thus, this work seeks to provide additional fundamental insights into the reaction chemistry of HMDSO and TMSO at conditions relevant to landfill gas and sludge gas applications, and for the development of hierarchical chemistry for this important class of compounds. With an

understanding of the scope of the problem and the fact that energy production from biogas is mainly through combustion methods, the following **Chapter 3 - Chapter 5** focus on understanding the reaction chemistry of two canonical silicon species – trimethylsilanol (TMSO) and hexamethyldisiloxane (HMDSO). These species are critical to biogas systems and provide foundation to developing siloxane chemistry due to the chemical structures they represent. The technical approach used to elucidate the fundamental chemistry of these compounds was to create state conditions relevant to combustion systems using facilities with well-known initial and boundary conditions, to facilitate advanced diagnostics to measure flow mixing and temperature in burner studies and flame speeds in ignition studies. These combustion characteristics have not been studied previously and the results provide additional insights into the reaction pathways important in these canonical siloxane combustion systems.

The studies presented in **Chapter 3** and **Chapter 4** used a flat flame burner to investigate the addition of siloxane and silanol to methane flames. Due to the large number of particles formed inside the flame, traditional diagnostic methods, like thermocouples and gas sampling, do not work well for *in-situ* measurements. To obtain the information within a flame with condensed phase particles, a novel combustion diagnostic method x-ray fluorescence (XRF) spectroscopy was used. Before applying this method to complex siloxane and silanol flames, **Chapter 3** demonstrated the process and results from an initial study characterizing the flow and temperature profiles of methane flat flames using XRF measurements. Specifically, a flat-flame burner equipped to allow siloxanes to be introduced to the flame system using a separate central flow tube was used for the XRF studies.

Flat flame burners are valuable tools for fundamental combustion studies and have been used extensively for studies of particle formation [49]-[53], combustion chemistry [54], and

diagnostic tool development and calibration [55], to name a few major research applications. A major advantage of 1D burners is that they can have well-defined governing equations and initial and boundary conditions, which makes it possible to emulate more complex combustion processes accurately. Among the different types of flat flame burners, a multi-element diffusion burner (MEDB, by Research Technologies, also called a Hencken burner) can provide highly uniform, stable and nearly adiabatic combustion conditions. Furthermore, separating the fuel and oxidizer flows eliminates the risk of flashback, while the rapid mixing of fuel and oxidizer above the surface of the burner can still be described by premixed equilibrium models. The inclusion of a central fuel tube (separate from the bulk fuel flow) also enables secondary fuel studies, including the study of particle forming precursors [49][51]-[53]. By stretching the central flame, different reaction zones can be studied via measurements at different heights.

While many studies have used MEDBs as platforms for combustion research, few have evaluated the flow and temperature fields near the surface of the MEDB or other flat flame burners. In the earlier work by De Goey et al. [56], operating conditions to create adiabatic flames using flat flame burners were presented. Due to the lack of advanced non-intrusive measurement techniques, the study used the uniformity of burner plate temperature to confirm adiabatic flame conditions. Later work by Hancock et al. [57] applied coherent anti-Stokes Raman scattering (CARS) spectroscopy to measure the axial temperature profile of a larger (38 mm square) MEDB burner with H_2 as the fuel. Measurements at 3.81 cm axial height above the burner (HAB) showed good agreement with equilibrium calculations for different equivalence ratios, and demonstrated that MEDBs are excellent tools for diagnostic development and calibration. Konnov et al. [58] used particle-image velocimetry (PIV) measurements to study the effects of pressure on spatial uniformity of the flame structures of a flat flame burner. The velocity field from 0.54 mm to 3.39

mm HAB was measured, showing that the burner was able to form a uniform 1-D flame front; however, fluctuations and non-uniformities in the flow speeds (in magnitude and direction) were observed. The study by Konnov et al. [58] also noted that it was impossible to measure the flow field below 0.5 mm HAB with this method due to strong reflection of the laser light sheet from the burner surface. The study by Belmont et al. [59] used OH planar laser-induced fluorescence (OH PLIF) to quantify the disruption of the flame when a sampling probe was inserted into the flame at heights from 9 to 23 mm above the burner surface. The measurements showed flame front displacements from 0.5 to 2.7 mm due to physical sampling. In more recent studies by Wang et al. [60] and Gu et al. [61], the impact of heat losses on temperature uniformity were investigated. Both studies found it was common for flame temperature to be lower than the predicted adiabatic temperature due to heat transfer effects.

These past studies demonstrate quantitative information with high spatial resolution, including temperature, velocity, and species concentration data, is valuable for flat flame burner research applications. The previous studies also show the value of non-intrusive methods that do not disrupt the flow and that can interrogate regions close to the surface of the burner, particularly below 0.5 mm HAB.

The objective of **Chapter 3** was to characterize the combustion system created by an MEDB using high-fidelity, non-intrusive measurements, in particular to provide new data on the mixing region near the surface of the burner. The technical approach used Kr Kα x-ray fluorescence (XRF) spectroscopy as an in-situ, non-invasive diagnostic method to quantify the combustion system, including fuel and air mixing very near the surface of the burner (e.g., within 2 mm of the burner surface) and temperature profiles of the burner flame. XRF has traditionally been used for non-destructive elemental analysis of solid and liquid samples in material and

biological areas [62]. However, in recent years, researchers have extended XRF to gas phase measurements [63]-[66] due to the attractive features of the method, including high energy penetration, insensitivity to temperature spectral broadening and high spatial fidelity.

Another benefit of this technique is that x-rays effectively only interact with the Kr tracer in the flow. Consequently, if there are particles generated during combustion, they have no impact on the signal [65]. Although the work in **Chapter 3** did not produce particles in the flame, this is a necessary feature for future gas-phase studies of systems with condensed phase reactants and products. Highly resolved XRF scans from multiple planar locations and at different heights above the burner surface were used in the current work to characterize the MEDB flow at reacting and non-reacting conditions. The results are compared with model predictions for a 1D system.

Chapter 4 presents the investigation of TMSO and HMDSO flames using a MEDB and measurement methods including XRF developed in **Chapter 3**. In **Chapter 4**, XRF measurements were explored as a means to measure temperature in laminar synthesis flames with high silica particle densities using hexamethyldisiloxane (HMDSO, $C_6H_{18}OSi_2$) and trimethylsilanol (TMSO, $C_3H_{10}OSi$) as the silica particle precursors, mainly focusing on the precursor reaction region near the burner surface (height above burner HAB < 20 mm). This work also verified the XRF technique's capability with high fidelity gas temperature measurement with condensed phase. The results from the XRF measurement in this study form the basis for more detailed analysis of siloxane chemistry related to silica particle synthesis and waste-to-energy process.

In **Chapter 4**, HMDSO and TMSO were observed to start reactions at relatively low temperatures. A hypothesis has been suggested that this phenomenon is caused by radicals penetrating into the central jet flow from the methane main flame. In prior work by Schwind [33] using the University of Michigan rapid compression facility, it was proposed that the initial

reactions of HMDSO are dominated by H-abstraction from a methyl group by free radicals such as H, OH, HO$_2$, and CH$_3$. In addition, in the low-temperature oxidation kinetics study by Wang et al. [67] on dimethyl ether (DME), a potential hydrocarbon surrogate for HMDSO, a model has been developed that at temperatures under 593 K, 93% of DME is consumed through H-abstraction by OH radicals and 6% of DME was consumed through H-abstraction by H radicals. Although the full HMDSO mechanism cannot be developed from DME reactions due to differences in the bonding and structures, the study by Wang et al. [67] may be a good reference to conjecture HMDSO initial reactions at low temperatures because of the commonality of the methyl groups where H-abstraction may initiate in both chemicals.

Although these studies provide some guesses on the reaction mechanism of HMDSO, the H-abstraction hypothesis has not been verified. A recent HMDSO oxidation mechanism developed by Huang et al. [45] using reactive force field (ReaxFF) proposed other initial reaction paths, which mainly include methyl group abstraction (29.8%) and O$_2$ addition (10.8%), and H-abstraction pathways only contribute to 5.4% of the total number of initial chemical events. The discrepancy between HMDSO reactions proposed by the different studies and between experimental and simulation results underscores the needs for validating and improving the reaction mechanism.

In **Chapter 5**, in order to investigate HMDSO reactions in additional flame systems with less complex flame geometries than the MEDB systems described in **Chapter 3** and **Chapter 4**, laminar flame speed experiments were conducted using a spherical laminar flame speed apparatus. Comparing with the MEDB flames in **Chapter 3** and **Chapter 4**, spherical propagating flames have reduced complexity and well-established models for data analysis [68]-[71]. As with the burner studies, methane flames were used for reference experiments and trace addition of HMDSO was added to assess the perturbation of the methane system by the HMDSO chemistry. Sensitivity

analysis of methane flame speeds helps to identify the key reactions that have largest impact on the flame speed and the potential impact of HMDSO on these reactions (e.g., via radical production) can be considered. Importantly, HMDSO flame speeds have never been measured previously. Thus, this work lays the foundation for subsequent studies that can develop new experimental protocols for novel and detailed experimental campaign on flame speed measurements for siloxanes.

Chapter 6 presents the conclusion of main findings of this dissertation work and recommendations for further research.

1.4 Citations

[1]   S. Rasi, J. Läntelä, J. Rintala, Trace compounds affecting biogas energy utilisation–A review, Energy Conversion and Management. 52 (2011) 3369–3375.

[2]   I. Bragança, F. Sánchez-Soberón, G.F. Pantuzza, A. Alves, N. Ratola, Impurities in biogas: Analytical strategies, occurrence, effects and removal technologies, Biomass and Bioenergy. 143 (2020) 105878.

[3]   A. Golmakani, S.A. Nabavi, B. Wadi, V. Manovic, Advances, challenges, and perspectives of biogas cleaning, upgrading, and utilisation, Fuel. 317 (2022) 123085.

[4]   E. Wheless, Siloxanes in Landfill and Digester Gas Update, (2004) 10.

[5]   J.N. Kuhn, A.C. Elwell, N.H. Elsayed, B. Joseph, Requirements, techniques, and costs for contaminant removal from landfill gas, Waste Management. 63 (2017) 246–256.

[6]   A. Jalali, M.M.Y. Motamedhashemi, F. Egolfopoulos, T. Tsotsis, Fate of Siloxane Impurities During the Combustion of Renewable Natural Gas, Combustion Science and Technology. 185 (2013) 953–974.

[7]   N. Nair, A. Vas, T. Zhu, W. Sun, J. Gutierrez, J. Chen, F. Egolfopoulos, T.T. Tsotsis, Effect of Siloxanes Contained in Natural Gas on the Operation of a Residential Furnace, Ind. Eng. Chem. Res. 52 (2013) 6253–6261.

[8]   I. Konkol, J. Cebula, J. Bohdziewicz, K. Piotrowski, P. Sakiewicz, M. Piechaczek-Wereszczyńska, A. Cenian, Mineral Deposit Formation in Gas Engines During Combustion of Biogas from Landfills and Municipal WWTP, Ecological Chemistry and Engineering S. 27 (2020) 347–356.

[9]   R. Dewil, L. Appels, J. Baeyens, Energy use of biogas hampered by the presence of siloxanes, Energy Conversion and Management. 47 (2006) 1711–1722.

[10]   N. Nair, X. Zhang, J. Gutierrez, J. Chen, F. Egolfopoulos, T. Tsotsis, Impact of Siloxane Impurities on the Performance of an Engine Operating on Renewable Natural Gas, Ind. Eng. Chem. Res. 51 (2012) 15786–15795.

[11]   J. Álvarez-Flórez, E. Egusquiza, Analysis of damage caused by siloxanes in stationary reciprocating internal combustion engines operating with landfill gas, Engineering Failure Analysis. 50 (2015) 29–38.

[12]   Y. Takuwa, T. Matsumoto, K. Oshita, M. Takaoka, S. Morisawa, N. Takeda, Characterization of trace constituents in landfill gas and a comparison of sites in Asia, J Mater Cycles Waste Manag. 11 (2009) 305–311.

[13]   K. Badjagbo, M. Héroux, M. Alaee, S. Moore, S. Sauvé, Quantitative Analysis of Volatile Methylsiloxanes in Waste-to-Energy Landfill Biogases Using Direct APCI-MS/MS, Environ. Sci. Technol. 44 (2010) 600–605.

[14]   B. Tansel, S.C. Surita, Differences in volatile methyl siloxane (VMS) profiles in biogas from landfills and anaerobic digesters and energetics of VMS transformations, Waste Management. 34 (2014) 2271–2277.

[15]   M. Ghidotti, D. Fabbri, C. Torri, Determination of linear and cyclic volatile methyl siloxanes in biogas and biomethane by solid-phase microextraction and gas chromatography-mass spectrometry, Talanta. 195 (2019) 258–264.

[16]   Z. Yang, Z. Chen, H. Gong, W. Wu, X. Wang, L. Chen, X. Yang, Effect of siloxane on performance of the Pt-doped γ-Al2O3 catalyst for landfill gas deoxygen, Fuel. 249 (2019) 161–168.

[17]   J. Läntelä, S. Rasi, J. Lehtinen, J. Rintala, Landfill gas upgrading with pilot-scale water scrubber: Performance assessment with absorption water recycling, Applied Energy. 92 (2012) 307–314.

[18]   O. Sevimoğlu, B. Tansel, Composition and source identification of deposits forming in landfill gas (LFG) engines and effect of activated carbon treatment on deposit composition, Journal of Environmental Management. 128 (2013) 300–305.

[19]   A. Divsalar, N. Entesari, M.N. Dods, R.W. Prosser, F.N. Egolfopoulos, T.T. Tsotsis, A UV photodecomposition reactor for siloxane removal from biogas: Modeling aspects, Chemical Engineering Science. 192 (2018) 359–370.

[20]   A. Divsalar, L. Sun, M.N. Dods, H. Divsalar, Richard.W. Prosser, F.N. Egolfopoulos, T.T. Tsotsis, Feasibility of Siloxane Removal from Biogas Using an Ultraviolet Photodecomposition Technique, Ind. Eng. Chem. Res. 57 (2018) 7383–7394.

[21]   M. Schweigkofler, R. Niessner, Removal of siloxanes in biogases, Journal of Hazardous Materials. 83 (2001) 183–196.

[22]   M. Ajhar, M. Travesset, S. Yüce, T. Melin, Siloxane removal from landfill and digester gas – A technology overview, Bioresource Technology. 101 (2010) 2913–2923.

[23]   G. Soreanu, P. Seto, Approaches concerning siloxane removal from biogas * A review, CANADIAN BIOSYSTEMS ENGINEERING. 53 (2011) 18.

[24]   Ö. Östürk, O. Sevimoğlu, Identification of major and minor elements by multiple analysis responsible for deposit formation on engine utilizing landfill gas, Fuel. 277 (2020) 118125.

[25]   S.C. Surita, B. Tansel, Preliminary investigation to characterize deposits forming during combustion of biogas from anaerobic digesters and landfills, Renewable Energy. 80 (2015) 674–681.

[26]   N. de Arespacochaga, C. Valderrama, J. Raich-Montiu, M. Crest, S. Mehta, J.L. Cortina, Understanding the effects of the origin, occurrence, monitoring, control, fate and removal of siloxanes on the energetic valorization of sewage biogas—A review, Renewable and Sustainable Energy Reviews. 52 (2015) 366–381.

[27] M.J. Almond, R. Becerra, S.J. Bowes, J.P. Cannady, J.S. Ogden, R. Walsh, A mechanistic study of cyclic siloxane pyrolyses at low pressures, Phys. Chem. Chem. Phys. 10 (2008) 6856.

[28] S. Peukert, P. Yatsenko, M. Fikri, C. Schulz, High-Temperature Rate Constants for the Reaction of Hydrogen Atoms with Tetramethoxysilane and Reactivity Analogies between Silanes and Oxygenated Hydrocarbons, J. Phys. Chem. A. 122 (2018) 5289–5298.

[29] H. Chagger, D. Hainsworth, P. Patterson, M. Pourkashanian, A. Williams, The formation of SiO2 from hexamethyldisiloxane combustion in counterflow methane-air flames, in: Symposium (International) on Combustion, Elsevier, 1996: pp. 1859–1865.

[30] O.M. Feroughi, L. Deng, S. Kluge, T. Dreier, H. Wiggers, I. Wlokas, C. Schulz, Experimental and numerical study of a HMDSO-seeded premixed laminar low-pressure flame for SiO2 nanoparticle synthesis, Proceedings of the Combustion Institute. 36 (2017) 1045–1053.

[31] R.A. Schwind, M.S. Wooldridge, Effects of organic silicon compounds on syngas auto-ignition behavior, Combustion and Flame. 212 (2020) 234–241.

[32] A.B. Mansfield, M.S. Wooldridge, The effect of impurities on syngas combustion, Combustion and Flame. 162 (2015) 2286–2295.

[33] R. Schwind, Understanding the Combustion Chemistry of Siloxanes: Reaction Kinetics and Fuel Interactions, PhD Thesis, 2019.

[34] M. Schweigkofler, R. Niessner, Determination of Siloxanes and VOC in Landfill Gas and Sewage Gas by Canister Sampling and GC-MS/AES Analysis, Environ. Sci. Technol. 33 (1999) 3680–3685.

[35] E.A. McBean, Siloxanes in biogases from landfills and wastewater digesters, Can. J. Civ. Eng. 35 (2008) 431–436.

[36] S. Rasi, J. Lehtinen, J. Rintala, Determination of organic silicon compounds in biogas from wastewater treatments plants, landfills, and co-digestion plants, Renewable Energy. 35 (2010) 2666–2673.

[37] B. Tansel, S.C. Surita, Differences in volatile methyl siloxane (VMS) profiles in biogas from landfills and anaerobic digesters and energetics of VMS transformations, Waste Management. 34 (2014) 2271–2277.

[38] L. Rivera-Montenegro, E.I. Valenzuela, A. González-Sánchez, R. Muñoz, G. Quijano, Volatile Methyl Siloxanes as Key Biogas Pollutants: Occurrence, Impacts and Treatment Technologies, Bioenerg. Res. (2022).

[39] H.G.P. Lewis, T.B. Casserly, K.K. Gleason, Hot-filament chemical vapor deposition of organosilicon thin films from hexamethylcyclotrisiloxane and octamethylcyclotetrasiloxane, Journal of the Electrochemical Society. 148 (2001) F212.

[40] M.S. Wooldridge, P.V. Torek, M.T. Donovan, D.L. Hall, T.A. Miller, T.R. Palmer, C.R. Schrock, An experimental investigation of gas-phase combustion synthesis of SiO2 nanoparticles using a multi-element diffusion flame burner, Combustion and Flame. 131 (2002) 98–109.

[41] T. Miller, M. Wooldridge, J. Bozzelli, Computational modeling of the SiH3+ O2 reaction and silane combustion, Combustion and Flame. 137 (2004) 73–92.

[42] J.A. Britten, J. Tong, C.K. Westbrook, A numerical study of silane combustion, in: Symposium (International) on Combustion, Elsevier, 1991: pp. 195–202.

[43] M.R. Zachariah, W. Tsang, Theoretical Calculation of Thermochemistry, Energetics, and Kinetics of High-Temperature SixHyOz Reactions, J. Phys. Chem. 99 (1995) 5308–5318.

[44]   Y. Karakaya, H. Somnitz, A. Hermsen, M. Gonchikzhapov, T. Kasper, Revisiting the initial reaction rates for TMS combustion and a new evidence for metastable silica nanoparticles in the gas-phase synthesis, Applications in Energy and Combustion Science. 14 (2023) 100152.

[45]   Y. Huang, H. Chen, A detailed reaction mechanism for hexamethyldisiloxane combustion via experiments and ReaxFF molecular dynamics simulations, Int J of Chemical Kinetics. (2023) kin.21698.

[46]   E.A. Chernyshev, T.L. Krasnova, A.P. Sergeev, E.S. Abramova, Siloxanes as sources of silanones, Russ Chem Bull. 46 (1997) 1586–1589.

[47]   M.J. Almond, R. Becerra, S.J. Bowes, J.P. Cannady, J.S. Ogden, N.A. Young, R. Walsh, A mechanistic study of the low pressure pyrolysis of linear siloxanes, Phys. Chem. Chem. Phys. 11 (2009) 9259.

[48]   Y. Chen, H. Chen, J. Wang, Y. Huang, Chemical kinetics of hexamethyldisiloxane pyrolysis: A ReaxFF molecular dynamics simulation study, International Journal of Chemical Kinetics. 54 (2022) 413–423.

[49]   M.S. Wooldridge, P.V. Torek, M.T. Donovan, D.L. Hall, T.A. Miller, T.R. Palmer, C.R. Schrock, An experimental investigation of gas-phase combustion synthesis of SiO2 nanoparticles using a multi-element diffusion flame burner, Combust. Flame 131 (2002) 98–109.

[50]   D. Khatri, A. Gopan, Z. Yang, A. Adeosun, R.L. Axelbaum, Characterizing early stage sub-micron particle formation during pulverized coal combustion in a flat flame burner, Fuel 258 (2019) 115995.

[51]   S.D. Bakrania, T.A. Miller, C. Perez, M.S. Wooldridge, Combustion of multiphase reactants for the synthesis of nanocomposite materials, Combust. Flame 148 (2007) 76-87.

[52]   S.D. Bakrania, C. Perez, M.S. Wooldridge, Methane-assisted combustion synthesis of nanocomposite tin dioxide materials, Proc. Combust. Inst. 31 (2007) 1797-1804.

[53]   T.A. Miller, S.D. Bakrania, C. Perez, M.S. Wooldridge, A new method for direct preparation of tin-dioxide nanocomposite materials, J. Mater. Res. 20 (2005) 2977-2987.

[54]   F.N. Egolfopoulos, N. Hansen, Y. Ju, K. Kohse-Höinghaus, C.K. Law, F. Qi, Advances and challenges in laminar flame experiments and implications for combustion chemistry, Prog. Energy Combust. Sci. 43 (2014) 36–67.

[55]   N.R. Grady, R.W. Pitz, C.D. Carter, K.-Y. Hsu, Raman scattering measurements of mixing and finite-rate chemistry in a supersonic reacting flow over a piloted, ramped cavity, Combust. Flame 165 (2016) 310–320.

[56]   L.P.H. De Goey, A. Van Maaren, R.M. Quax, Stabilization of adiabatic premixed laminar flames on a flat flame burner, Combust. Sci. Technol. 92 (1993) 201-207.

[57]   R.D. Hancock, K.E. Bertagnolli, R.P. Lucht, Nitrogen and hydrogen CARS temperature measurements in a hydrogen/air flame using a near-adiabatic flat-flame burner, Combust. Flame 109 (1997) 323-331.

[58]   A.A. Konnov, R.Riemeijer, V.N. Kornilov, L.P.H. De Goey, 2D effects in laminar premixed flames stabilized on a flat flame burner, Exp. Therm. Fluid Sci. 47 (2013) 213-223.

[59]   E. Belmont, T. Ombrello, M. Brown, C. Carter, J. Ellzey, Experimental and numerical investigation of freely propagating flames stabilized on a Hencken Burner, Combust. Flame 162 (2015) 2679-2685.

[60] P. Wang, X. Luo, Q. Li, Heat transfer study of the Hencken burner flame, Flow Turbul. Combust. 101 (2018) 795-819.

[61] M. Gu, S. Wang, G. Wang, Q. Wang, X. Liu, F. Qi, C.S. Goldenstein, Improved laser absorption spectroscopy measurements of flame temperature via a collisional line-mixing model for CO_2 spectra near 4.17 μm, Appl. Phys. B 128 (2022) 1-12.

[62] B. Beckhoff, ed., Handbook of practical X-ray fluorescence analysis, Springer, Berlin ; New York, 2006.

[63] R.S. Tranter, A.L. Kastengren, J.P. Porterfield, J.B. Randazzo, J.P.A. Lockhart, J.H. Baraban, G.B. Ellison, Measuring flow profiles in heated miniature reactors with x-ray fluorescence spectroscopy, Proc. Combust. Inst. 36 (2017) 4603–4610.

[64] N. Hansen, R.S. Tranter, K. Moshammer, J.B. Randazzo, J.P. Lockhart, P.G. Fugazzi, T. Tao, A.L. Kastengren, 2D-imaging of sampling-probe perturbations in laminar premixed flames using Kr x-ray fluorescence, Combust. Flame 181 (2017) 214-224.

[65] M.J. Montgomery, H. Kwon, A.L. Kastengren, L.D. Pfefferle, T. Sikes, R.S. Tranter, Y. Xuan, C.S. McEnally, In situ temperature measurements in sooting methane/air flames using synchrotron x-ray fluorescence of seeded krypton atoms, Sci. Adv. 8.17 (2022) eabm7947.

[66] C. Banyon, M.J. Montgomery, H. Kwon, A.L. Kastengren, L.D. Pfefferle, T. Sikes, Y. Xuan, C.S. McEnally, R.S. Tranter, Temperature measurements of heavily-sooting ethylene/air flames using synchrotron x-ray fluorescence of krypton, Combust. Flame (in press). DOI: 10.1016/j.combustflame.2022.112494

[67] Z. Wang, X. Zhang, L. Xing, L. Zhang, F. Herrmann, K. Moshammer, F. Qi, K. Kohse-Höinghaus, Experimental and kinetic modeling study of the low- and intermediate-temperature oxidation of dimethyl ether, Combustion and Flame. 162 (2015) 1113–1125.

[68] D. Bradley, P.H. Gaskell, X.-J. Gu, Burning velocities, Markstein lengths, and flame quenching for spherical methane-air flames: a computational study, Combustion and Flame. 104 (1996) 176–198.

[69] F.N. Egolfopoulos, N. Hansen, Y. Ju, K. Kohse-Höinghaus, C.K. Law, F. Qi, Advances and challenges in laminar flame experiments and implications for combustion chemistry, Progress in Energy and Combustion Science. 43 (2014) 36–67.

[70] Z. Chen, On the accuracy of laminar flame speeds measured from outwardly propagating spherical flames: Methane/air at normal temperature and pressure, Combustion and Flame. 162 (2015) 2442–2453.

[71] M. Faghih, Z. Chen, The constant-volume propagating spherical flame method for laminar flame speed measurement, Science Bulletin. 61 (2016) 1296–1310.

Chapter 2 Characterizing the Presence, Impact and Potential of Siloxanes in U.S. Landfill Gas

2.1 Introduction
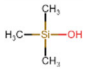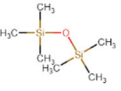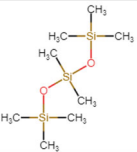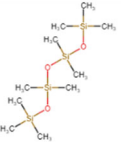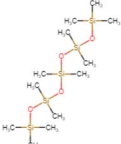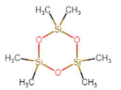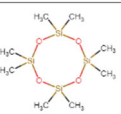
As the world faces challenges of climate change, environmental degradation, and the depletion of finite fossil fuels, transitioning to sustainable energy solutions has become imperative. One renewable and sustainable energy source that has gained increased attention in recent years is biogas [1]-[4]. Biogas is produced through the natural decomposition of organic matter such as municipal solid waste, municipal wastewater, animal manure and crops in anaerobic environments [5]-[7]. Among the different type of biogas, landfill gas and sludge gas from waste water treatment plants (WWTP) offer a sustainable and eco-friendly solution to energy generation, waste management, and greenhouse gas reduction [8]-[12]. In the remaining part of this paper, biogas specifically refers to landfill gas and sludge gas from WWTP. The compositions of landfill gas and sludge gas are complex and depend on the waste materials and decomposition process, and mainly include methane and carbon dioxide and trace amounts of nitrogen, hydrogen, oxygen, moisture, hydrogen sulfide and volatile organic compounds [13]-[15]. The successful utilization of biogas is significantly complicated by some of the trace compounds, for example, organic silicon species including silanols and siloxanes. The chemical structures and information on silicon compounds commonly found in biogas are shown in **Table 2.1**. Most of the silicon species are siloxanes except TMSO, therefore to be concise, when discussing siloxanes in the following paragraphs, TMSO is also included.

The presence of silicon-based chemicals in biogas was not widely noted in the last century, but has been increasingly observed in the last two decades [22]-[25]. This is likely caused by the increased use of siloxanes in industrial and commercial applications, which is supported by the patent search results presented in **Figure 2.1**. The final destinations of many silicon-containing products are ultimately trash and wastewater systems, and they rapidly accumulate in landfills and WWTPs, causing a continuous release of volatile organic silicon compounds into landfill and sludge gas [26][27].
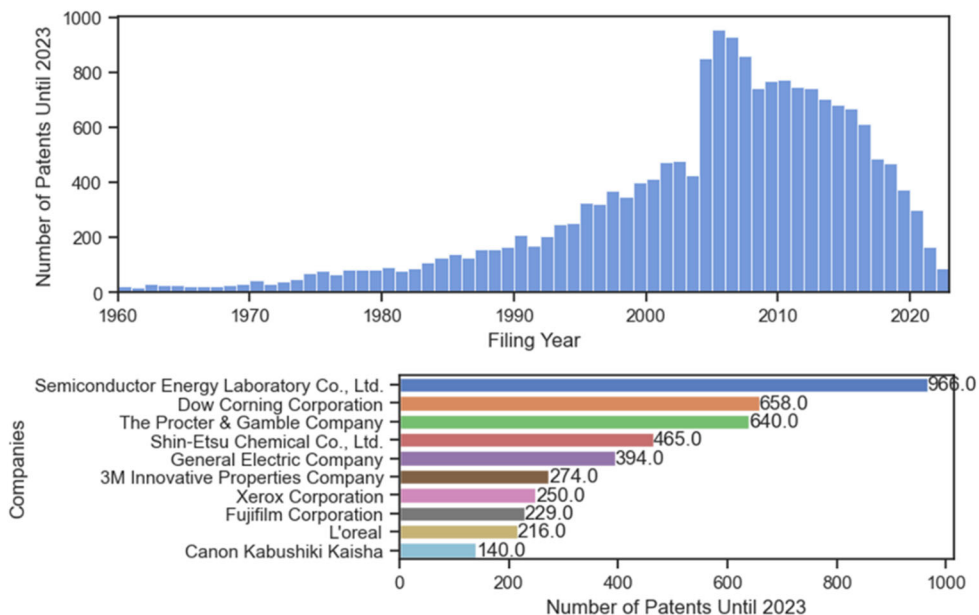
Figure 2.1 Analysis of Google Patent search results with the keyword 'siloxane'. Search URL: https://patents.google.com/?q=%28siloxane%29&country=US. The top figure shows the number of patents filed each year between 1960 and October 12, 2023. The bottom figure shows the top 10 companies filing the most patents until October 12, 2023.

Table 2.1 Thermodynamic data on trimethylsilanol and siloxanes
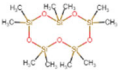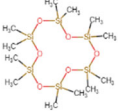
Symbol	Compound	Acronym	Chemical formula	Molecular weight (g/mol)	SiO₂ yield (mg/mg)	O₂ required (mol/mol)	Boiling point (°C)	Vapor pressure at 25°C (mbar)
	Trimethylsilanol	TMSO	$C_3H_{10}OSi$	90.197	0.666	6	99	29.351 [16] [2]
	Hexamethyldisiloxane	L2	$C_6H_{18}OSi_2$	162.379	0.740	12	100-101	55.640 [17] [3]
	Octamethyltrisiloxane	L3	$C_8H_{24}O_2Si_3$	236.54	0.762	15	153	4.453 [18]
	Decamethyltetrasiloxane	L4	$C_{10}H_{30}O_3Si_4$	310.69	0.773	20	194-195	0.50 [19]
	Dodecamethylpenta-siloxane	L5	$C_{12}H_{36}Si_5O_4$	384.84	0.781	24	230	0.060 ± 0.05 [20]
	Hexamethylcyclotri-siloxane	D3	$C_6H_{18}O_3Si_3$	222.462	0.810	12	134	6.137 [21] [4]
	Octamethylcyclotetra-siloxane	D4	$C_8H_{24}O_4Si_4$	296.62	0.810	16	175-176	1.245± 0.062[20]

[2] Ref. [16] reported incorrect linear fitting equation of TMSO vapor pressure data. The equation applied here is $log_{10} P_{mm} = 9.3568 - 2389.4/T$, from linear regression of reported data in this reference.

[3] Calculated from equation (2) in ref. [17]

[4] Multiple websites (http://www.thegoodscentscompany.com/data/rw1249951.html, https://www.gelest.com/wp-content/uploads/product_msds/SIH6105.1-msds.pdf) have reported D3 vapor pressure data under room temperature using liquid vapor pressure equation in ref. [21]. However, D3 is solid under room temperature room pressure, with a melting point around 65 °C. Therefore, the solid vapor pressure equation in ref. **Error! Reference source not found.** should be used.

	Decamethylcyclopenta-siloxane	D5	$C_{10}H_{30}O_5Si_5$	370.77	0.810	20	210	0.204 ± 0.011[20]
	Dodecamethylcyclohexa-siloxane	D6	$C_{12}H_{36}O_6Si_6$	444.92	0.810	22	245	0.0226 ± 0.0144 [20]

Organic silicon species are generally non-toxic and have low concentrations in biogas; usually less than 50 mg/m^3. However, during combustion, the silicon chemicals are oxidized and form condensed-phase silica particles in the combustion equipment. The silica particles deposit on the surrounding surfaces and accumulate over time, which results in damage of flare equipment, engine components like pistons and cylinder heads, and fouling of heat exchangers. The deposits generally increase potential of equipment failure and require higher maintenance costs [28]-[34]. In addition, the silicon compounds can also contaminate lubricating oils, creating a soft paste that also leads to increased maintenance [32]. Considering 85% of currently operational landfill gas energy projects in the U.S. directly utilize combustion methods (i.e., projects directly using landfill gas and not upgrading landfill gas to renewable natural gas) [35], the potential damage and economical loss caused by organic silicon compounds is substantial.

Currently, there are no standard regulations toward removing siloxanes from biogas. However, multiple companies have specified maximum siloxane limits for their power equipment when used with biogas, as shown in **Table 2.2** [36]-[38]. A key challenge is that historically siloxanes are not monitored in biogas, and the presence of siloxanes may be underestimated.

Table 2.2 Total siloxane limit for waste-to-energy equipment

Publication Year	Equipment	Manufacturer	Unit	Siloxane Limitations	Ref.
2002	IC engine		mg/m^3	11 - 25	[36]
2002	IC engine		mg Si/m^3	10 - 15	[36]
2004	IC engine	Caterpillar	mg/m^3	28	[37]
2004	IC engine	Jenbacher	mg/m^3	10	[37]
2004	IC engine	Waukesha	mg/m^3	25	[37]
2004	IC engine	Deutz	mg/m^3	5	[37]
2004	Turbine	Solar Turbines	mg/m^3	0.1	[37]
2004	Turbine	Ingersoll-Rand Microturbines	mg/m^3	0.06	[37]
2004	Turbine	Capstone Microturbines	mg/m^3	0.03	[37]
2004	Fuel Cell		ppbv	100	[37]

Year	Technology	Model	Units	Value	Ref
2006	IC engine		ppm in CH4	9 - 44	[38]
2006	Turbine		ppm in CH4	0.087	[38]
2006	Turbine	Microturbine	ppm in CH4	0.01	[38]
2006	Fuel Cell	MCFC	ppm	1	[38]
2006	IC engine	Stirling engine	ppm in CH4	0.42	[38]
2008	IC engine		mg/m^3	2.8	[36]
2015	IC engine	Jenbacher	mg/m^3	12	[22]
2015	IC engine	Waukesha	mg/m^3	30	[22]
2015	IC engine	Tech3solution	mg/m^3	5	[22]
2015	Fuel Cell		mg/m^3	0.05 - 0.1	[22]
2015	Natural Gas Grid		mg/m^3	0.5 - 10	[22]

Siloxane treatment technologies are expensive and include traditional methods such as absorption, adsorption, and deep chilling and emerging methods such as biotrickling filters, catalysts, and membranes [22][23][39]-[42]. However, from the literature and local field visits, siloxanes are typically not a priority in the pre-processing of biogas (e.g., compared with hydrogen sulfides). In addition, for the sites with siloxane removal equipment, there is limited information about the effectiveness of the removal methods, associated costs, and ultimate fate of the removed siloxanes. If the removed siloxanes are returned back to landfill, it is possible the siloxanes will re-enter the landfill gas in the long term.

Despite the issues caused by siloxanes in the waste-to-energy process, these compounds are valuable chemicals as precursors for silicon material synthesis [43]. In addition, trimethylsilanol (TMS) and hexamethyldisiloxane (L2) are highly energetic and ignitable. Past studies have discovered that TMS and L2 can reduce the ignition delay time of syngas [44][45]. If the amount of silicon chemicals in biogas continuously increase, harvesting the chemicals from biogas and reusing them as particle synthesis precursors or combustion additives can be another

value-added pathway for waste systems. While the concentrations are low in biogas, the outcomes of the current work provide vital information required to determine the feasibility of gas recovery for any groups interested in developing such technologies and processes.

Either for understanding and mitigating impacts caused by silicon compounds in waste-to-energy process or for evaluating these chemicals as a potential resource, it is necessary to have a clear understanding of the presence and trends of siloxanes in biogas. While many studies have documented local issues and concerns regarding silicon-containing compounds on waste gas (e.g., specific assessment of total silicon levels, etc.), to date there are no attempts to integrate the data in the literature and to summarize the past and expected trends. ~~Therefore, the objective of~~ This study ~~was to~~ systematically and quantitatively assesses the types and trends of silicon species found in biogas using data reported in open literature, industrial reports, and from stakeholder feedback, and compares these results with new data from U.S. landfills acquired over a two-year period. The objective of this work is to utilize the collected data to provide the first large scale interpretation of the presence of siloxanes that can be used to enable the design of systems to improve waste-to-energy projects. The technical approach included evaluating the effects of geographic location, temporal trends, types and levels of silicon-containing compounds, and estimating associated silica production. The results are discussed in terms of expected trends in the future.

2.2 Methods

The current work collected previous data in the literature on siloxanes in biogas facilities around the world and collected new data from landfills in the U.S. Feedback from local landfill operators on concerns (if any) on silicon-containing species in landfill gas was also collected. The feedback was solicited via informal semi-structured interviews. Landfill operators were initially

contacted using contact email addresses found on public access web sites. Meetings were conducted by web conferencing and phone calls to perators willing to be interviewed. A general list of guiding questions was initially provided to the operators, then the conversation was allowed to follow the operator's interests, concerns and experiences.

2.2.1 Landfill Gas Sampling and Measurement

Several operators of landfill energy production sites in the U.S. were approached to hear concerns regarding silicon compounds in actual landfill gas and to determine willingness to share archived silicon data collected at their sites. Some facilities were also willing to allow gas-sampling measurements to assess the presence of silicon compounds and to characterize the composition over time. A gas sampling procedure was established and continued for two years, per one to fourth months from 2022 to 2023. Briefly, sample bags were cleaned and prepared before collection by evacuation. The sample bags were connected to access ports on the biogas ducts upstream of the turbine or engine at each landfill site. The slight positive pressure of the landfill gas was sufficient to fill the sample bag. The sample bags were brought back to the University of Michigan and the contents were analyzed using calibrated gas chromatographs. Two sample bags were typically filled at each visit. The major components of landfill gas were identified and quantified including siloxanes and methane. Additional details are provided below.

The gas samples were collected from two U.S. landfills in the Midwest, designated as site A and site B. Both landfills started operating within the last century. Site A uses two reciprocating engines to produce electricity from landfill gas with no H_2S removal. Site B uses a gas turbine to produce electricity from landfill gas after H_2S removal. Gas samples from both sites were collected upstream of the engine and can be considered characteristic of the unprocessed gas for site A and of the processed gas (after H_2S removal) for site B. Measurements of gas samples collected before

and after H2S removal showed no significant changes in the siloxane levels, indicating the H2S treatment did not affect the silicon compounds. Gas sampling bags (Cole-Parmer Kynar Gas Sampling Bag) were used to collect the landfill gas at ambient temperatures (nominally 20 °C) and transfer the samples to the analytical laboratory at the University of Michigan. On the day before each sampling trip, the bags were connected to a gas manifold and flushed with nitrogen a minimum of three times to remove any residuals. The bags were then evacuated and labeled for use the next day. At each landfill site, the bags were filled with landfill gas and sealed by septum valves on the bags. The bags were shipped back to the university laboratory within two to four hours and were isolated from light to prevent photochemical reactions until all measurements were completed within the following one to five days.

Measurements were made by using gas chromatography with a flame ionization detector (GCFID) and gas chromatography mass spectrometry (GCMS). GCFID was used to quantify the siloxane levels using calibration standards and mass spectrometry (GCMS) was used to identify unknown chemicals in the landfill gas. Calibrations were established for TMSO, L2, L3, L4, D3, D4 and D5 using reference compounds (Sigma-Aldrich with 97-98% purity) and custom gas mixtures made using a dedicated mixing facility at the University of Michigan.

2.2.2 Systematic Analysis of Prior Reported Data on Silicon Compounds in Biogas

A comprehensive literature review was conducted to identify relevant studies that reported original information of siloxanes in landfill gas and sludge gas from waste water digesters and landfills [28][36][49]-[83]. Data preprocessing, unit conversions, estimations, and statistical analysis were then conducted. Studies were selected based on the presence of either original measurement data or, in some cases unpublished data were shared. Relevant information was

extracted from the sources, including the average, minimum, maximum, and standard deviation of each silicon compound (when species specific data were reported), the total amount of silicon compounds, the limit of detection (LOD) or limit of quantitation (LOQ), sampling year, geographic location, facility type, and sampling and measurement methods used. The complete list of data attributes is provided in **Table 2.3**.

Table 2.3 Data attributes collected for silicon compounds in waste water treatment plant (WWTP) and landfill gas facilities

Data Attributes	Explanation
Pub Year	Publication year of the data source
Location	Geographic location of the landfill or WWTP site. If details were not reported, the country of the primary author was used
LOD/LOQ	Limit of Detection/Limit of Quantitation of silicon compound measurements
DL_Units	Units of the reported LOD/LOQ, e.g., mg/m^3
Sam_Year	Year the gas samples were acquired and analyzed
Data_Units	Units of the reported siloxane concentrations
(Siloxane)_min*	Minimum value of siloxane species concentration observed
(Siloxane)_max*	Maximum value of siloxane species concentration observed
(Siloxane)_ave*	Average value of siloxane species reported; if a range was not reported, the single value was used as the average
(Siloxane)_stdev*	Standard deviation of siloxane species concentration
Total_min	The reported or calculated minimum concentration of all siloxane species
Total_max	The reported or calculated maximum concentration of all siloxane species
Total_ave	The reported or calculated average concentration of all siloxane species
Total_Si_min	The reported or calculated minimum silicon concentration
Total_Si_max	The reported or calculated maximum silicon concentration
Total_Si_ave	The reported or calculated average silicon concentration
Sam_Site	Sampling site type (L: Landfill; W: WWTP)
Sam_Position	Sampling position (e.g. raw gas, before engine; after gas pre-treatment)
Sam_Method	Sampling method (e.g. Tedlar bags, canister, impinge, etc.)
Mea_Method	Measurement method (e.g. GCMS, GCPID, APCI-MS and etc.)
Notes	Anything to be aware of
Pdf_Source	If there's a pdf version of data source available (0: no available; 1: available)
Source_MLA	The original data source reference in format of MLA
Data_From	If the pdf version of the original data source is not available, indicating where the numerical data are from (i.e., the article that used the data and

[*](Siloxanes) represents species abbreviations as listed in **Table 2.1**

Due to differences in reporting and measurement protocols, attempts to standardize the data were made. First, measurements were typically reported in the literature as concentration, i.e., mass of silicon-compound per unit volume of biogas (e.g., mg/m^3, $\mu g/L$ or $\mu g/m^3$) or as volume fraction of silicon in biogas (e.g., ppmv). To enable meaningful comparisons, all data were converted to silicon concentration in biogas in units of mg/m^3 and ppmv for this work. In addition, the concentration values were examined to ensure they were within the theoretically calculated maximum limits based on the vapor pressures of the individual compounds at 25 °C as listed in **Table 2.1**. No data exceeding these limits were discovered in the dataset.

The dataset was subjected to statistical analysis (Python pandas library [46]). Aggregate statistics, including average, minimum, maximum and standard deviations were determined for key parameters, as listed in **Table 2.3**. In cases where only minimum and maximum values were reported, the average of the maximum and minimum was used as the nominal value of the parameter.

Geographical information was extracted from the data sources (Python-based OpenCage Geocoder [47]). This process involved determining the country and continent where the sample data were acquired, and when sampling location details were lacking, the country of the first authors' affiliation was used as a surrogate.

Statistical methods were employed to investigate potential correlations between various reporting factors, including geographic location, year, concentrations of individual silicon species, total silicon concentrations, and other parameters.

Before data processing, an assessment of the data source quality was performed to evaluate the quality of the data set. The result of the assessment is shown in **Figure 2.2**. The percentage values represent the number of available data divided by the total number of rows in the dataset. Specifically, the dataset includes information from 38 unique sources, including 34 papers from the literature. While detailed speciation data are more limited, and therefore have lower statistical confidence, the total silicon data and other key parameters are well represented in the sources. Notably, WWTP and landfill gas facilities are nearly equally represented in the reporting.
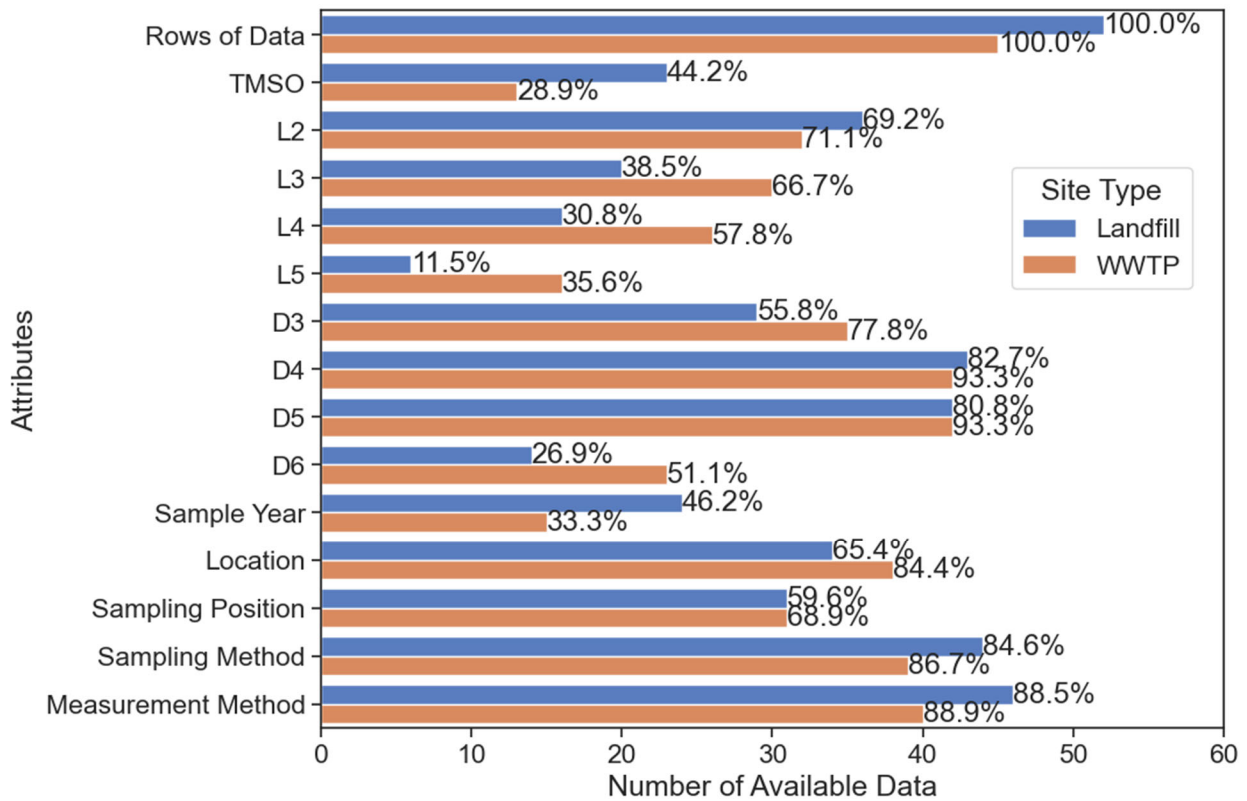
Figure 2.2 Number of available data (52 rows of data for landfill, 45 rows of data for WWTP). The percentage of available data for each attribute is shown at right side of each bar.

2.3 Results and Discussion

2.3.1 Feedback from Midwest Landfill Energy Operators

As part of the current work, landfill gas operators and management organizations were contacted and were asked to describe concerns (if any) regarding the composition of their landfill

gas and any information they could share on silicon organic compounds. Operators provided data and feedback on key issues. Silicon compounds were present in the landfill gas and caused significant issues requiring increased maintenance of the power equipment. **Figure 2.3** shows photos of a cylinder head and spark plugs from a commercial engine operating with landfill gas at Site C. Layers of white powder were present at multiple locations and caused damage to the valves. The composition of the particles removed from the engine head was determined using scanning electron microscopy energy dispersive spectroscopy. The results indicate C composition of 51.52% by mole and 35.50% by mass; Si of 11.81 % by mole and 19.03% by mass; O of 29.64% by mole and 27.21% by mass. A scanning electron microscope (SEM) image of the particulates is shown in **Figure 2.4**. and indicates the deposits were a coarse powder with particles generally less than 20 μm in size. The major elements in the deposits are carbon, silicon and oxygen, and the proportions indicate the deposits were mainly accumulation of silica (SiO_2) and primarily carbonaceous soot particles.

Data on silicon contamination of engine oil was also shared from one of the landfill sites. **Figure 2.5** shows the total concentration of silicon compounds in the engine oil in two power units as a function of operating time (equivalent miles of engine operation) at landfill site A. The silicon in the oil increased significantly (over a factor of four from the start of the data collection to the end) and proportionally with the engine operating hours. The silicon contamination of the engine oil required the local landfill site operator to replace the engine oil with twice the frequency compared with sites without silicon compounds in the landfill gas.

Figure 2.3 Photos of landfill gas piston engine parts showing white powder deposits attributed to silica. Left: cylinder head after scrubbing and cleaning to remove deposits. Note the damage to the valves due to particle accumulation; Right: spark plugs showing white particle accumulation attributed to silica.

SEM HV: 10.0 kV	View field: 883 µm		MIRA3 TESCAN
BI: 15.00	Det: SE	200 µm	
SEM MAG: 391 x	WD: 14.42 mm		(MC)²

C %	O %	Si %	S %	Ca %	Sb %
51.52	29.64	11.81	1.95	3.04	1.10
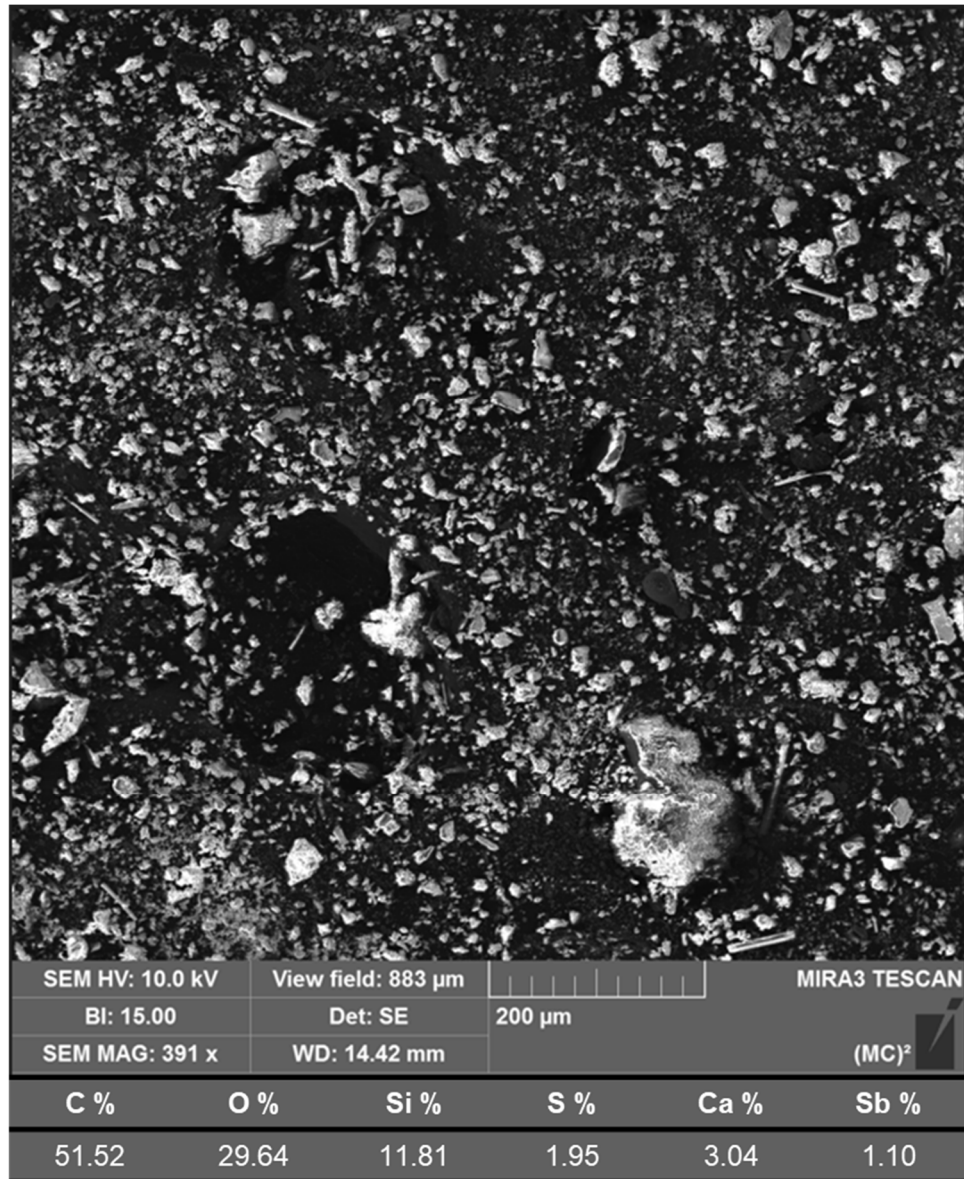
Figure 2.4 Scanning electron microscope (SEM) **i**mage and elemental mole composition results for particles removed from landfill gas engine cylinder head at landfill site A.
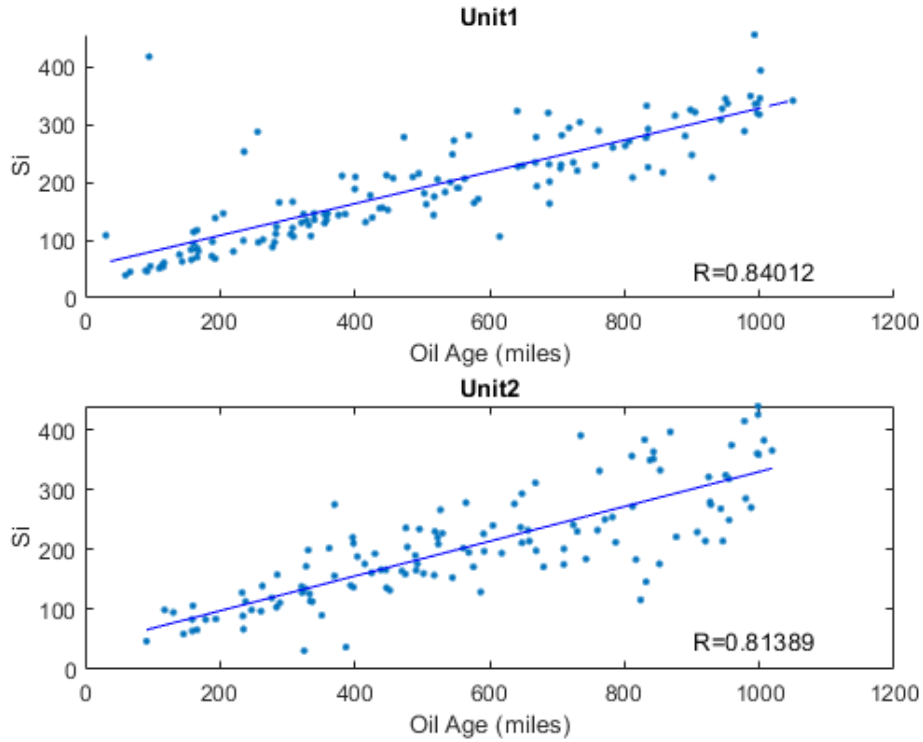
Figure 2.5 Normalized silicon concentration in engine oil from two piston engine units operating at landfill site C.

2.3.2 Sampling Results at two U.S Landfills
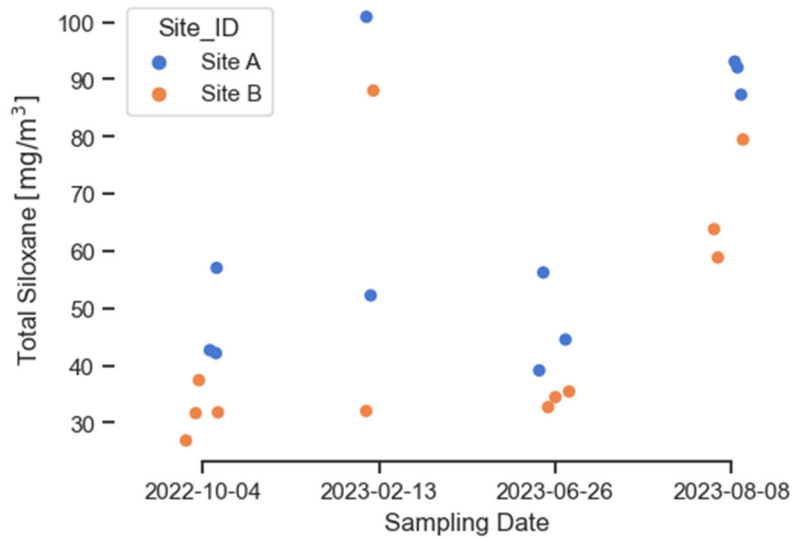
Figure 2.6 Total siloxane concentrations (including TMSO) in landfill gas from two U.S. landfill sites from 2022-2023

Total siloxane concentrations in landfill gas samples collected at two U.S. landfill sites are shown in **Figure 2.6** with the sampling date. TMSO, L2 – L4, D3 – D5 were detected, and the total concentrations were calculated as the sum of TMSO and other siloxane concentrations. The variations of data for each sampling trip is large mainly due to GC measurement uncertainties. There was a GC injection volume change since 2023-06-26, which reduces the fluctuation of GC peak areas. Compared between all sampling trips, no obvious trend was observed. However, there was an increase of total siloxane concentrations from 2023-06-26 to 2023-08-08, which could possibly due to change of ambient temperature at the landfill site. Future monitoring of the silicon compounds concentrations is necessary to evaluate its correlation with temperature changes from season to season.
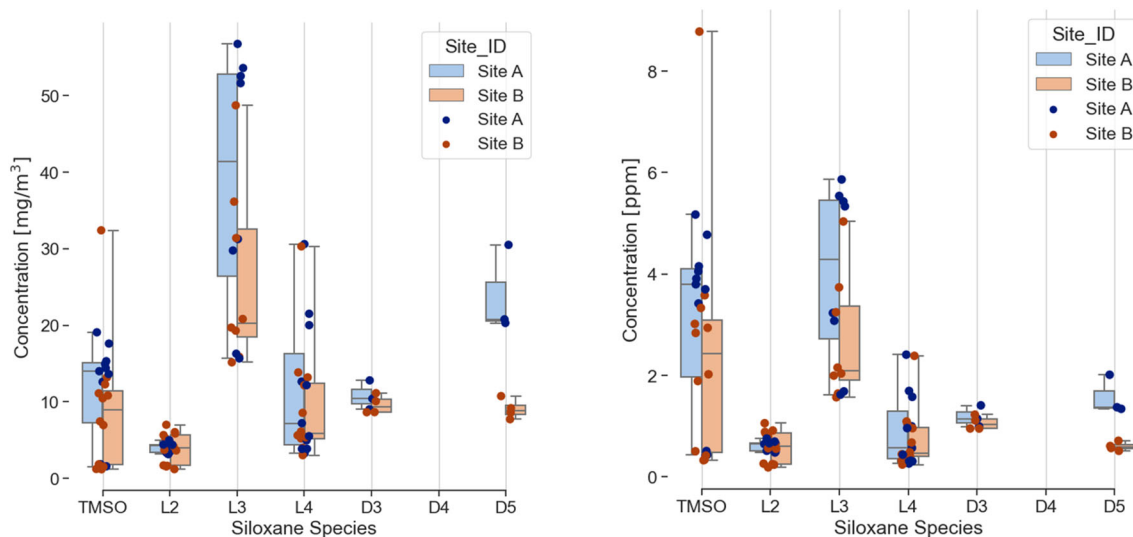
Figure 2.7 Concentrations of TMSO and siloxane species in landfill gas samples from two U.S. landfill sites in units of mg/m^3 (left) and ppm (right)

The concentrations of TMSO and siloxane species in the landfill gas sample is shown in **Figure 2.7**, in both units of mg/m^3 and ppmv. The results show that L3 and D5 has high mass

concentrations, while TMSO, L3, D3 and D5 have higher mole concentrations. This trend will be further compared with the data from other researches.

2.3.3 Longitudinal Data on Silicon Compounds

The data collected from the literature and the Midwest landfill sites were analyzed to determine trends with respect to location, time, types of silicon compounds observed and other aspects important for characterizing current and future effects on landfill and waste water gas. The geographic distribution of data was limited to the northern hemisphere. **Figure 2.8** shows the locations of the landfill and WWTP sites in the northern hemisphere and includes indication of the total average concentration of siloxane [mg/m^3] compounds found in landfill and WWTP reports. In the instances where the detailed location of the site was not reported, the latitudinal and longitudinal position of the center of the country where the data were acquired or where the first author's affiliation located was used. The color and size of the bubbles represent the total average concentrations, and the site types are presented in warm colors for landfill sites and cold colors for WWTPs as shown in the color bars. From the map, it can be seen that the majority of the data were reported in Europe. This is consistent with the fact that Europe has the largest number of biogas production sites while other regions of the world are in the process of developing more biogas facilities [48]. Data reported in the U.S. were primarily from sites on the west coast and Florida, which is similar with the distribution of U.S. landfill gas energy projects [35]. While the frequency of data reporting is far less than the total number of landfill and WWTP sites in the world, the results indicate the presence of silicon compounds is a global concern for biogas, and not confined to one region in the world. The regions in the US and central Europe report the highest concentrations, which may be due to the large number of chemical manufacturing facilities in those area.
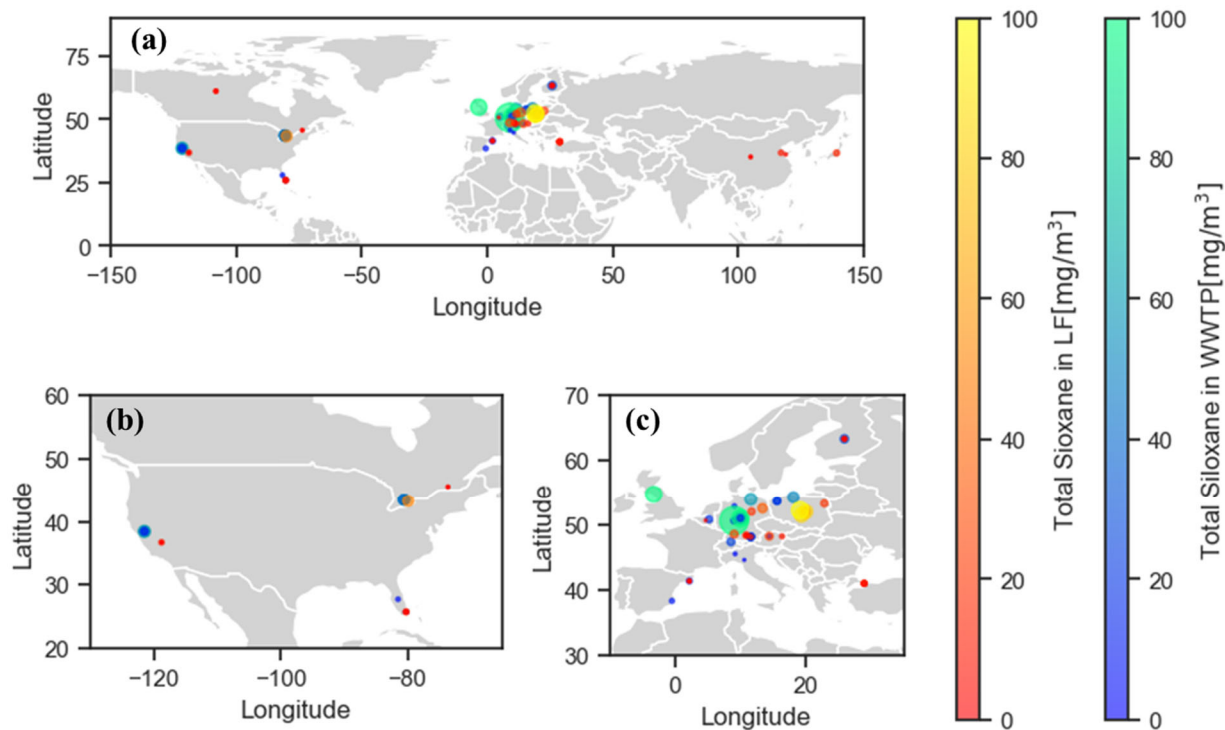
Figure 2.8 Locations and concentrations of total siloxane species reported in landfill and WWTP studies and reports from 1999 – 2021. (a) Northern Hemisphere; (b) U.S.; (c) Europe.

Figure 2.9 shows the distribution of the total siloxane concentrations in landfill gas and sludge gas in Europe, North America and Asia. For all figures reporting statistics, the shaded boxes indicate the values between lower and upper quartiles. The limits of the whiskers are the maximum and minimum values observed, and the arithmetic mean is shown as the bar within the gray box. The levels varied largely even within same continent and the data generally span two orders of magnitude. This is consistent with Midwest operator feedback that the level of silicon compounds varied significantly with the type and quantity of waste entering the landfill, which varied significantly regionally based on their experience. The results in **Figure 2.9** show, the total siloxane levels in Europe had the largest range, from 1 to over 100 mg/m^3. There was no significant difference between the siloxane concentrations from landfill gas and sludge gas in Europe. However, in North America, sludge gas from WWTP generally had higher concentration of

38

siloxanes compared with landfills. In Asia, no siloxane concentrations in sludge gas were available, and the data on landfill gas were also limited.
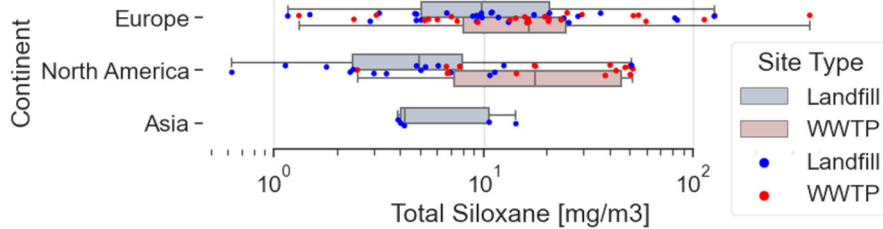
Figure 2.9 Comparison of total siloxane concentrations in gas samples from landfill and WWTP in the Europe, North America and Asia.

The siloxane concentration data are disaggregated by county in **Figure 2.10**. Similar to the concentration distribution by continent, **Figure 2.10** shows that sludge gas still exhibited higher concentrations compared with landfills when compared by country. This trend may be explained by the use of silicone chemicals in personal care products, which enter waste water during the production process or from household usage [22][27].
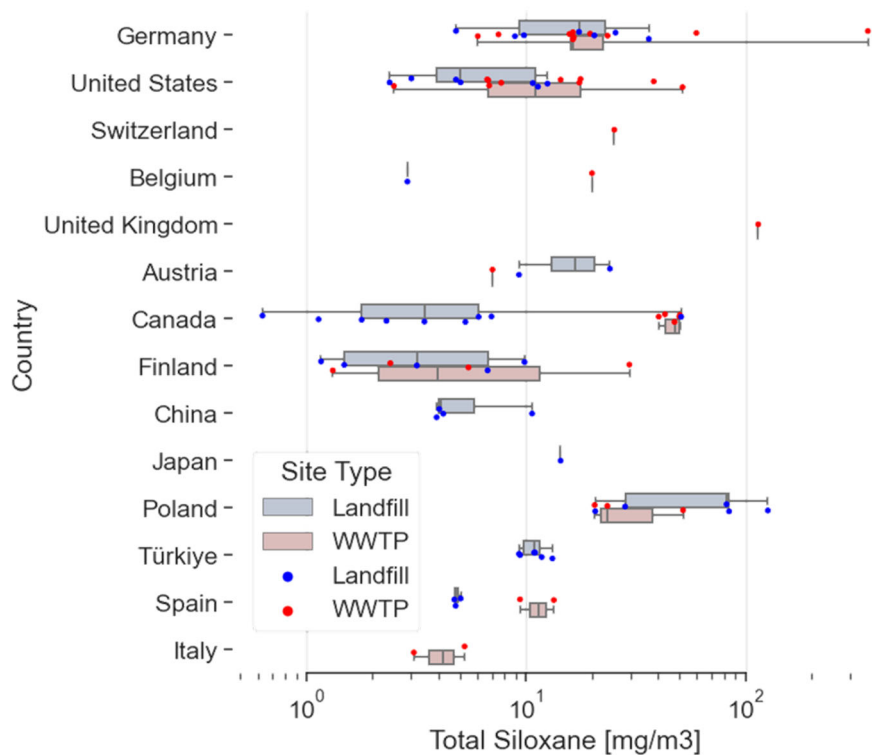
Figure 2.10 Comparison of total siloxane levels by country in gas samples from landfill and WWTPs.

Because the actual date of the analysis was not consistently provided, the total siloxane and silicon concentrations are presented as a function of time based on the publication years of the source articles in **Figure 2.11**. For data sources that included the sampling date, the sampling year could be zero to four years earlier than the publication date. As seen in the figure, the majority of data were below 50 mg/m^3, and the average value of total siloxane concentration for all data is 25 mg/m^3. There are few points with high concentrations in the past decade, but there are no clear trends in terms of net increasing or decreasing levels in landfill gas or WWTP gas. However, this is attributed to the lack of longitudinal studies at specific sources; essentially because of the insufficient monitoring of silicon compounds in biogas. However, it is worth noting that even 20 mg/m^3 siloxanes in biogas has a significant negative impact on the operation of biogas energy projects. In addition, as noted earlier, some studies quantified the total concentration of silicon compounds and some studies resolved the concentrations of specific compounds (e.g., see **Figure 2.2**). If key silicon-containing species were omitted, the total siloxane levels may be underestimated in these studies and reports.
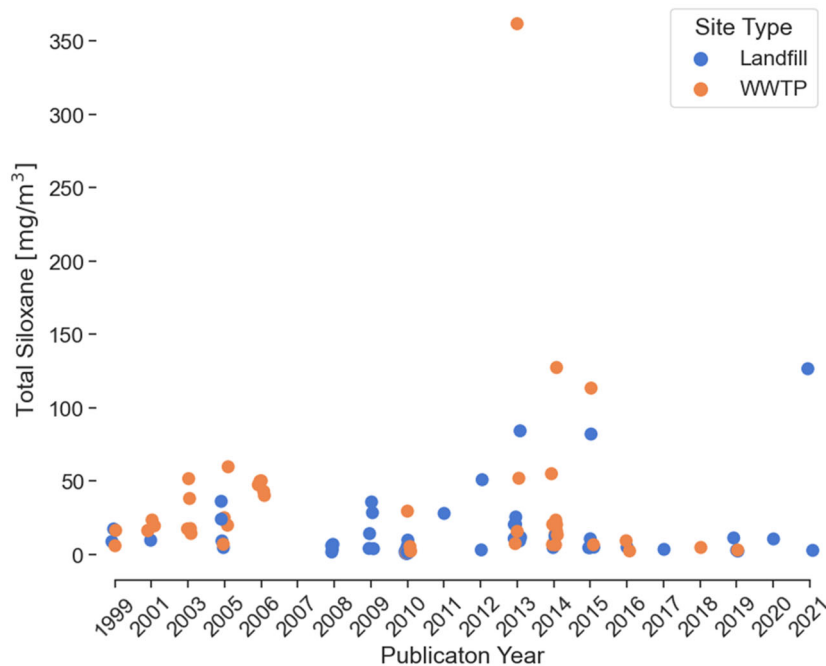
Figure 2.11 Reported total siloxane concentrations based on the publication year of the report.

The species-specific data were also analyzed to understand if any trends were apparent when species were considered individually or in relation to other silicon compounds or the total quantity of silicon compounds.

The distribution of specific siloxane species concentrations is shown in **Figure 2.12**. The ranges of concentrations were large; often spanning three decades. However, some trends are apparent. D5 is systematically the highest concentration in WWTP biogas and TMSO is systematically the highest concentration in landfill gas. It is also interesting to see that some siloxane species have generally high concentrations that are not correlated with their vapor pressures. For example, for sludge gas from WWTP, the larger cyclic siloxanes D4 and D5 have the highest concentrations, while their vapor pressures are lower than TMSO, L2, L3 and D3, as shown in **Table 2.1**. In landfill gas, TMSO, L2, D4 and D5 have higher concentration compared with other siloxanes. The shifts in species concentrations between landfill gas and WWTP gas is likely due to the different sources of the silicon compounds in the solid waste sent to landfills and

41

waste water sent to WWTPs. In addition, differences in the anaerobic reactions in the facilities can lead to different intermediate and product species. Tansel et. al. [49] observed similar trends in their gas samples that D4 and D5 comprised 62% and 28% of total siloxanes by mass in sludge gas from WWTP but TMSO and D4 comprised 58% and 17% of total siloxanes by mass in landfill gas. They proposed that the formation of TMSO in landfills is due to reactions between large cyclic siloxanes with H radicals or with methane. This trend towards producing TMSO is consistent with the higher concentrations of TMSO observed in landfills seen in **Figure 2.12**. The lower concentration of the longer chain length L5 indicates either these species are consumed more readily in landfills and WWTPs, or they are not formed by the source silicon compounds found in the waste materials. For landfills in particular, the data indicate the reaction processes tend to systematically favor the shorter chain length for the linear siloxanes, again providing some insight on the intermediate anaerobic reaction processes.
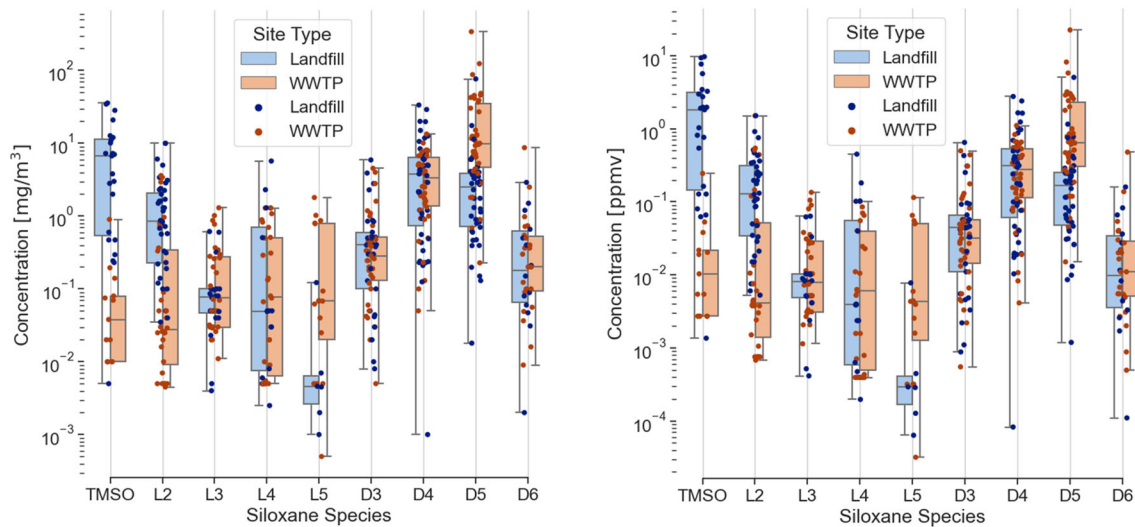
Figure 2.12 Concentration distributions of each siloxane species. The concentration unit is mg/m^3 for the left plot and ppmv for the right plot.

To understand the contribution to the total silicon concentration in the gases, **Figure 2.12** left panel shows the mass fraction distribution of species and **right panel** shows the mole fraction

distribution. Accounting for only TMSO and D4 and D5, captures approximately 83.75% of the total silicon compounds mass in the landfill data and 90.94% of the total silicon compounds mass in the WWTP data. Including L2 leads to capture of 90.46% (mass basis) of the silicon compounds in landfill. However, the sampling results from this study in **Figure 2.7** do not follow this trend, and the reason why L3 has higher concentration needs to be further studied.

Statistical analysis was also applied to understand correlations between species. The correlation maps are shown in **Figure 2.13** for landfill gas and **Figure 2.14** for sludge gas from WWTP. The correlation maps used the units of ppm to remove the impact by molecular weight of the different species. To reduce bias by outliers, median absolute deviation (MAD) was used to identify and remove outliers for each species using a modified Z-Score and a threshold of 3.5. Due to lack of L5 data, L5 is not included in the correlation analysis. From **Figure 2.13**, the TMSO concentrations in ppm are highly correlated with total siloxane concentrations in landfill gas, while D3, L2-L4 are weakly correlated with total concentrations. D4, D5 and D6 also have modest correlations with the total concentrations, but considering the larger molecular mass of D4-D6, their contributions to the total mass yield of silicon are prominent. In contrast, TMSO concentrations in sludge gas show limited correlation with the total siloxane concentrations, and D5 has the strongest correlation. From this observation, the total siloxane concentrations can be estimated with TMSO concentrations for landfill gas and with D5 for sludge gas in the future. This provides opportunities for continuously monitoring the total siloxane concentrations with onsite measurement for only few siloxane species.
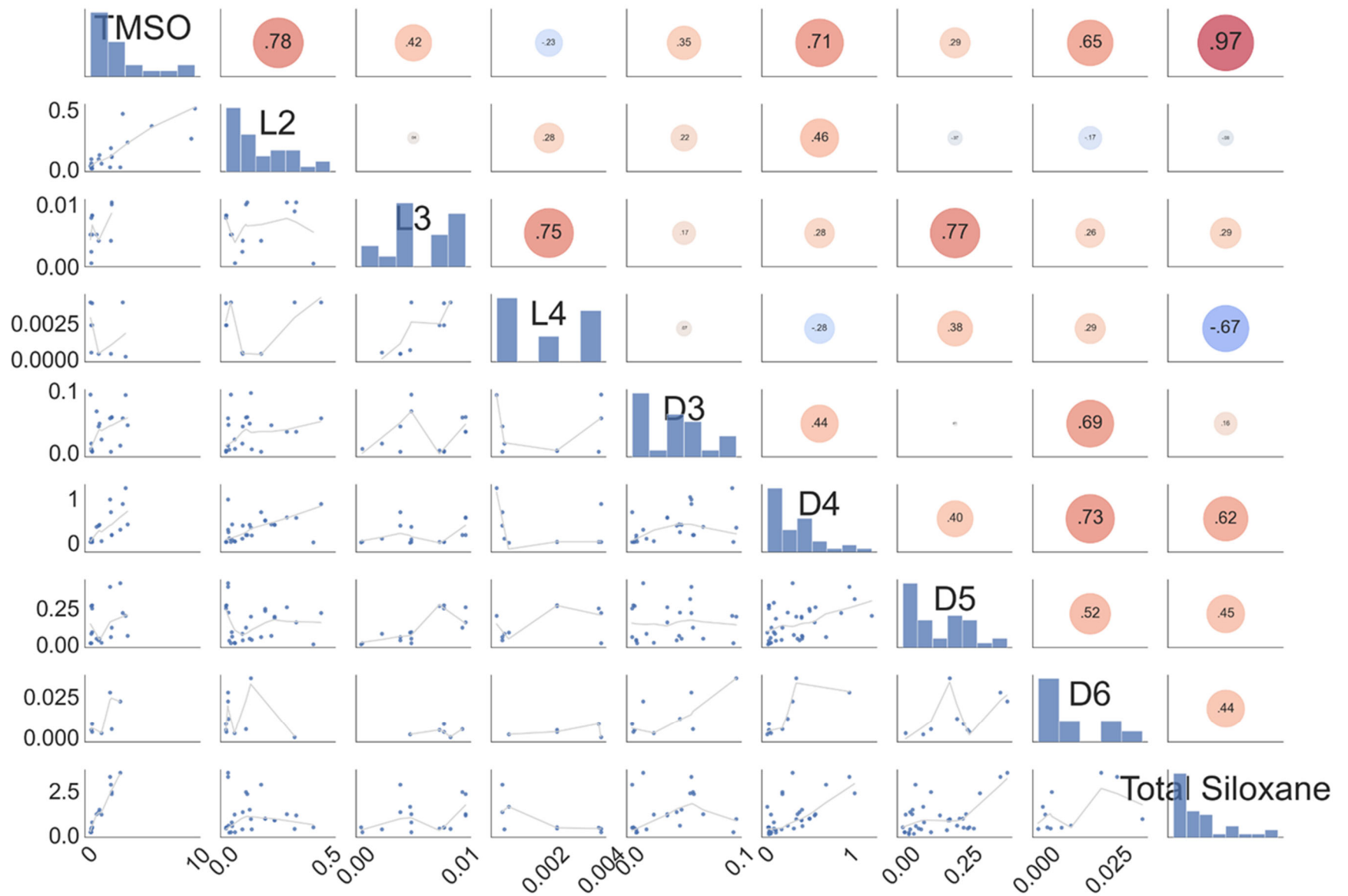
Figure 2.13 Correlations between each siloxane species and the total siloxane concentrations in landfill gas (units: ppmv)
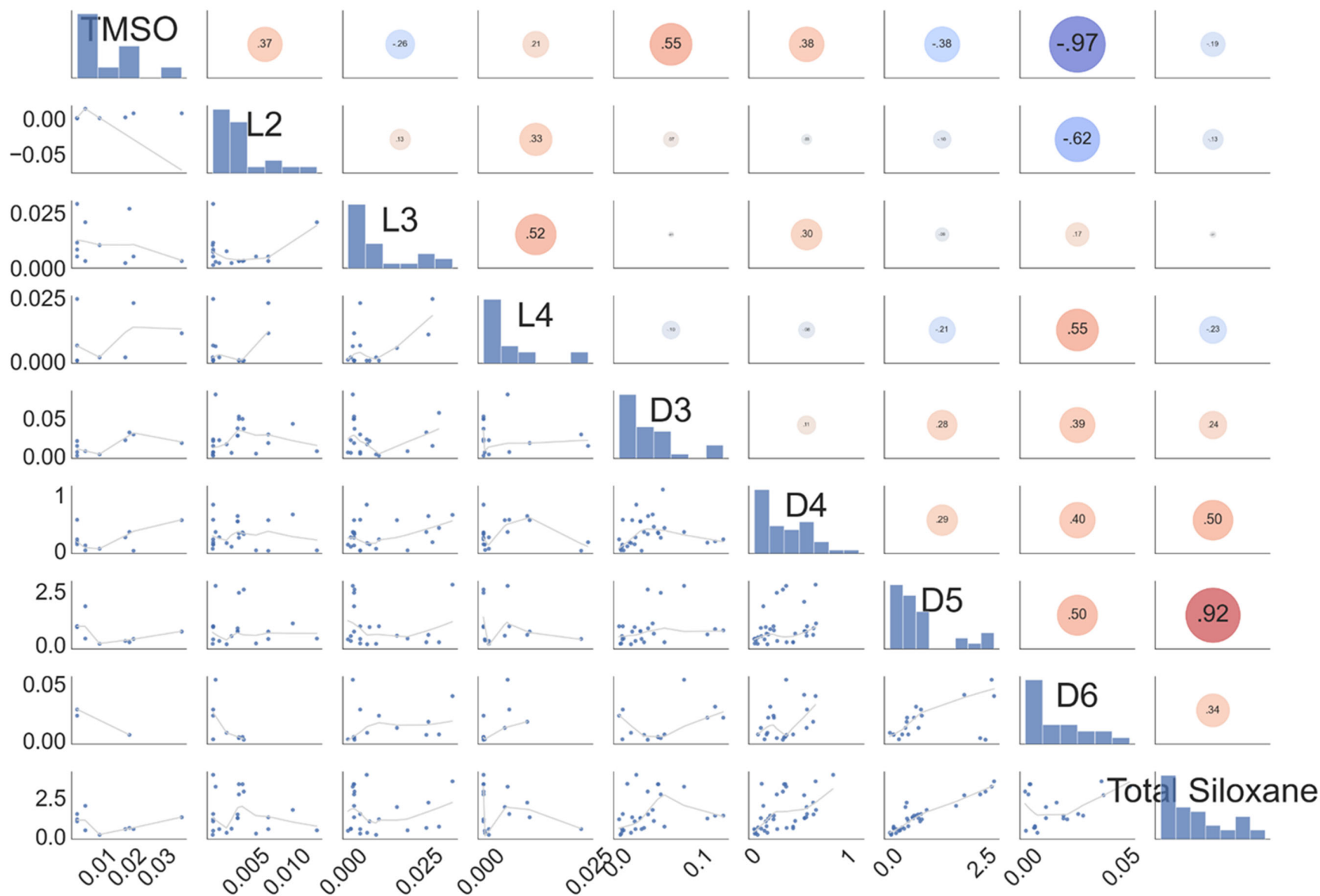
Figure 2.14 Correlations between each siloxane species and the total siloxane concentrations in sludge gas from WWTP (units: ppmv)

2.4 Conclusions

The present study was designed to investigate the presence, impact and potential of organic silicon compounds on landfill and sludge gas, though interviews with landfill site operators, periodically landfill gas sampling and statistical analysis of published siloxane data.

From the site visits at U.S. local landfill sites, the feedbacks from landfill-gas-to-energy operators were collected. Most of the operators have expressed their concerns about the formation of particles inside the engines and the increased maintenance frequency due to siloxanes. Gas sampling results show that the siloxane concentrations in the two landfill sites' gas are relatively high compared with the literature data, but the distribution of siloxane species didn't follow the general trend. No obvious increasing trend has been observed during the two-year sampling results, but more frequent sampling would be required in the future in order to provide insights on the relationship between siloxane levels and ambient temperature.

From the statistical analysis on published siloxane concentration data, the distribution of the sampling locations, the published year of the data, the concentrations of each siloxane species, the total siloxane concentrations, the correlations between specific species concentrations and total concentrations were studied. It can be seen that siloxanes in biogas has been a worldwide problem, though there are more studies in Europe compared with the other region of the world. In addition, there are a few high total siloxane concentrations reported in recent years (2013-2015 and 2021), but increasing monitoring of siloxanes in the future is required to confirm if there is an increasing trend of siloxanes concentrations. From the separate species concentrations, it has been observed that D4 and D5 have the highest concentrations in both landfill and sludge gas, while TMSO and L2 have high concentrations in landfill gas but not in sludge gas. Finally, the correlation analysis reveals that the landfill gas total siloxane concentrations is mostly correlated with TMSO, while

in sludge gas D5 is the most correlated species. This provides opportunities for waste-to-energy industry to monitoring the siloxane concentrations in their gas continuously through measurement of fewer species, which reduces the complexity and cost compared with measuring the total siloxane concentrations.

This study has provided a deeper insight in to the presence of siloxanes in biogas. However, the analysis was limited by the relatively small numbers of available siloxane data sources and the lack of essential information such as sampling date, sampling locations, whether the gas samples have been preprocessed, etc. It is suggested that siloxane concentrations at waste-to-energy sites should be more frequently monitored. A public online siloxane database including data contributed by both academic and industrial studies would be of great help in studying the worldwide trend of siloxanes. The database described in this chapter could be used to establish an initial online siloxane data sharing platform. More importantly, the outcomes of this study provide a quantitative foundation for technology development to recover siloxanes from biogas sites and to develop methods for siloxane abatement and mitigation to improve energy recovery from waste water treatment facilities and landfills.

2.5 Citations

[1]   B.C. Murray, C.S. Galik, T. Vegh, Biogas in the United States: estimating future production and learning from international experiences, Mitigation and Adaptation Strategies for Global Change. 22 (2017) 485–501.
[2]   N. Scarlat, J.-F. Dallemand, F. Fahl, Biogas: Developments and perspectives in Europe, Renewable Energy. 129 (2018) 457–472.
[3]   X. Jiang, S.G. Sommer, K.V. Christensen, A review of the biogas industry in China, Energy Policy. 39 (2011) 6073–6081.
[4]   P.G. Kougias, I. Angelidaki, Biogas and its opportunities—A review, Frontiers of Environmental Science & Engineering. 12 (2018) 1–12.

[5]   L. Appels, J. Baeyens, J. Degrève, R. Dewil, Principles and potential of the anaerobic digestion of waste-activated sludge, Progress in Energy and Combustion Science. 34 (2008) 755–781.

[6]   C. Mao, Y. Feng, X. Wang, G. Ren, Review on research achievements of biogas from anaerobic digestion, Renewable and Sustainable Energy Reviews. 45 (2015) 540–555.

[7]   IEA (2020), Outlook for biogas and biomethane: Prospects for organic growth, IEA, Paris https://www.iea.org/reports/outlook-for-biogas-and-biomethane-prospects-for-organic-growth, License: CC BY 4.0

[8]   C. Yaman, Investigation of greenhouse gas emissions and energy recovery potential from municipal solid waste management practices, Environmental Development. 33 (2020) 100484.

[9]   H. Omar, S. Rohani, Treatment of landfill waste, leachate and landfill gas: A review, Frontiers of Chemical Science and Engineering. 9 (2015) 15–32.

[10]   Y. Shen, J.L. Linville, M. Urgun-Demirtas, M.M. Mintz, S.W. Snyder, An overview of biogas production and utilization at full-scale wastewater treatment plants (WWTPs) in the United States: challenges and opportunities towards energy-neutral WWTPs, Renewable and Sustainable Energy Reviews. 50 (2015) 346–362.

[11]   D. Fytili, A. Zabaniotou, Utilization of sewage sludge in EU application of old and new methods—A review, Renewable and Sustainable Energy Reviews. 12 (2008) 116–140.

[12]   A. Raheem, V.S. Sikarwar, J. He, W. Dastyar, D.D. Dionysiou, W. Wang, M. Zhao, Opportunities and challenges in sustainable treatment and resource reuse of sewage sludge: A review, Chemical Engineering Journal. 337 (2018) 616–641.

[13]   P. Gupta, C. Kurien, M. Mittal, Biogas (a promising bioenergy source): A critical review on the potential of biogas as a sustainable energy source for gaseous fuelled spark ignition engines, International Journal of Hydrogen Energy. 48 (2023) 7747–7769.

[14]   A. Golmakani, S.A. Nabavi, B. Wadi, V. Manovic, Advances, challenges, and perspectives of biogas cleaning, upgrading, and utilisation, Fuel. 317 (2022) 123085.

[15]   S. Rasi, J. Läntelä, J. Rintala, Trace compounds affecting biogas energy utilisation–A review, Energy Conversion and Management. 52 (2011) 3369–3375.

[16]   W.T. Grubb, R.C. Osthoff, Physical properties of organosilicon compounds. II. Trimethylsilanol and triethylsilanol, Journal of the American Chemical Society. 75 (1953) 2230–2232.

[17]   D. Scott, J. Messerly, S. Todd, G. Guthrie, I. Hossenlopp, R. Moore, A. Osborn, W. Berg, J. McCullough, HEXAMETHYLDISILOXANE: CHEMICAL THERMODYNAMIC PROPERTIES AND INTERNAL ROTATION ABOUT THE SILOXANE LINKAGE1, The Journal of Physical Chemistry. 65 (1961) 1320–1326.

[18]   Haz-Map, Information on Hazardous Chemicals and Occupational Diseases https://haz-map.com/Agents/18767

[19]   Haz-Map, Information on Hazardous Chemicals and Occupational Diseases https://haz-map.com/Agents/17959

[20]   Y.D. Lei, F. Wania, D. Mathers, Temperature-dependent vapor pressure of selected cyclic and linear polydimethylsiloxane oligomers, Journal of Chemical & Engineering Data. 55 (2010) 5868–5873.

[21]   R.C. Osthoff, W. Grubb, C.A. Burkhard, Physical properties of organosilicon compounds. I. Hexamethylcyclotrisiloxane and octamethylcyclotetrasiloxane, Journal of the American Chemical Society. 75 (1953) 2227–2229.

[22]   N. de Arespacochaga, C. Valderrama, J. Raich-Montiu, M. Crest, S. Mehta, J.L. Cortina, Understanding the effects of the origin, occurrence, monitoring, control, fate and removal of siloxanes on the energetic valorization of sewage biogas—A review, Renewable and Sustainable Energy Reviews. 52 (2015) 366–381.

[23]   I. Bragança, F. Sánchez-Soberón, G.F. Pantuzza, A. Alves, N. Ratola, Impurities in biogas: Analytical strategies, occurrence, effects and removal technologies, Biomass and Bioenergy. 143 (2020) 105878.

[24]   G. Piechota, Biogas/Biomethane Quality and Requirements for Combined Heat and Power (CHP) Units/Gas Grids with a Special Focus on Siloxanes-a Short Review, SCE. (2021) 1–10.

[25]   L. Rivera-Montenegro, E.I. Valenzuela, A. González-Sánchez, R. Muñoz, G. Quijano, Volatile Methyl Siloxanes as Key Biogas Pollutants: Occurrence, Impacts and Treatment Technologies, Bioenerg. Res. (2022).

[26]   B. Tansel, S. Surita, Historical and projected trends of siloxane use in consumer products, associated impacts on municipal solid waste and landfill gas utilization, International Journal of Environmental Science and Technology. 14 (2017) 795–802.

[27]   S.C. Surita, B. Tansel, Emergence and fate of cyclic volatile polydimethylsiloxanes (D4, D5) in municipal waste streams: release mechanisms, partitioning and persistence in air, water, soil and sediments, Science of the Total Environment. 468 (2014) 46–52.

[28]   R. Dewil, L. Appels, J. Baeyens, Energy use of biogas hampered by the presence of siloxanes, Energy Conversion and Management. 47 (2006) 1711–1722.

[29]   N. Nair, X. Zhang, J. Gutierrez, J. Chen, F. Egolfopoulos, T. Tsotsis, Impact of Siloxane Impurities on the Performance of an Engine Operating on Renewable Natural Gas, Ind. Eng. Chem. Res. 51 (2012) 15786–15795.

[30]   A. Jalali, M.M.Y. Motamedhashemi, F. Egolfopoulos, T. Tsotsis, Fate of Siloxane Impurities During the Combustion of Renewable Natural Gas, Combustion Science and Technology. 185 (2013) 953–974.

[31]   N. Nair, A. Vas, T. Zhu, W. Sun, J. Gutierrez, J. Chen, F. Egolfopoulos, T.T. Tsotsis, Effect of Siloxanes Contained in Natural Gas on the Operation of a Residential Furnace, Ind. Eng. Chem. Res. 52 (2013) 6253–6261.

[32]   J. Álvarez-Flórez, E. Egusquiza, Analysis of damage caused by siloxanes in stationary reciprocating internal combustion engines operating with landfill gas, Engineering Failure Analysis. 50 (2015) 29–38.

[33]   I. Konkol, J. Cebula, J. Bohdziewicz, K. Piotrowski, P. Sakiewicz, M. Piechaczek-Wereszczyńska, A. Cenian, Mineral Deposit Formation in Gas Engines During Combustion of Biogas from Landfills and Municipal WWTP, Ecological Chemistry and Engineering S. 27 (2020) 347–356.

[34]   Ö. Östürk, O. Sevimoğlu, Identification of major and minor elements by multiple analysis responsible for deposit formation on engine utilizing landfill gas, Fuel. 277 (2020) 118125.

[35]   EPA's US Landfill Gas Energy Project Data Files [July 2023] https://www.epa.gov/lmop/landfill-gas-energy-project-data

[36]   E.A. McBean, Siloxanes in biogases from landfills and wastewater digesters, Can. J. Civ. Eng. 35 (2008) 431–436.

[37]   E. Wheless, Siloxanes in Landfill and Digester Gas Update, Proceedings of the 27th SWANA Landfill Gas Symposium. San Antonio, TX: Silver Springs (2004) 10.

[38]   S. Lampe, Assessment of fuel gas cleanup systems for waste gas fueled power generation, EPRI, Palo Alto, CA. 1012763 (2006).

[39]   M. Ajhar, M. Travesset, S. Yüce, T. Melin, Siloxane removal from landfill and digester gas – A technology overview, Bioresource Technology. 101 (2010) 2913–2923.

[40]   C.M.A.C. Alves, F.O.M.S. Abreu, R.S. Araújo, M.L.M. Oliveira, Recent advances in siloxanes removal from biogas and their efficiency: a short review, Chem. Pap. (2022).

[41]   J.N. Kuhn, A.C. Elwell, N.H. Elsayed, B. Joseph, Requirements, techniques, and costs for contaminant removal from landfill gas, Waste Management. 63 (2017) 246–256.

[42]   G. Soreanu, P. Seto, Approaches concerning siloxane removal from biogas * A review, CANADIAN BIOSYSTEMS ENGINEERING. 53 (2011) 18.

[43]   H.G.P. Lewis, T.B. Casserly, K.K. Gleason, Hot-filament chemical vapor deposition of organosilicon thin films from hexamethylcyclotrisiloxane and octamethylcyclotetrasiloxane, Journal of the Electrochemical Society. 148 (2001) F212.

[44]   R.A. Schwind, M.S. Wooldridge, Effects of organic silicon compounds on syngas auto-ignition behavior, Combustion and Flame. 212 (2020) 234–241.

[45]   A.B. Mansfield, M.S. Wooldridge, The effect of impurities on syngas combustion, Combustion and Flame. 162 (2015) 2286–2295.

[46]   W. McKinney, others, Data structures for statistical computing in python, in: Proceedings of the 9th Python in Science Conference, Austin, TX, 2010: pp. 51–56.

[47]   D. Possenriede, J. Sadler, M. Salmon, opencage: Geocode with the OpenCage API, 2023.

[48]   M. Farghali, A.I. Osman, K. Umetsu, D.W. Rooney, Integration of biogas systems into a carbon zero and hydrogen economy: a review, Environmental Chemistry Letters. 20 (2022) 2853–2927.

[49]   B. Tansel, S.C. Surita, Differences in volatile methyl siloxane (VMS) profiles in biogas from landfills and anaerobic digesters and energetics of VMS transformations, Waste Management. 34 (2014) 2271–2277.

[50]   M. Schweigkofler, R. Niessner, Determination of Siloxanes and VOC in Landfill Gas and Sewage Gas by Canister Sampling and GC-MS/AES Analysis, Environ. Sci. Technol. 33 (1999) 3680–3685.

[51]   M. Schweigkofler, R. Niessner, Removal of siloxanes in biogases, Journal of Hazardous Materials. 83 (2001) 183–196.

[52]   H.C. Hayes, S. Saeed, G.J. Graening, A SUMMARY OF AVAILABLE ANALYTICAL METHODS FOR THE DETERMINATION OF SILOXANES IN BIOGAS, (2003) 7.

[53]   P. Lens, P. Westermann, M. Haberbauer, A. Moreno, Biofuels for fuel cells, IWA publishing, 2005.

[54]   H. Monteith, K. Yajima, D. Andrews, P. Steel, Assessing Feasibility of Direct Drive Technology for Energy Recovery from Digester Biogas, Proc Water Environ Fed. 2006 (2006) 3517–3540.

[55]   O. Kazuyuki, T. Masaki, M. Tadao, K. Hiroshi, T. Nobuo, K. Akira, Behavior of siloxanes in a municipal sewage-treatment plant, J. Jpn. Sewage Works Ass. 44 (2007) 125.

[56]   Y. Takuwa, T. Matsumoto, K. Oshita, M. Takaoka, S. Morisawa, N. Takeda, Characterization of trace constituents in landfill gas and a comparison of sites in Asia, J Mater Cycles Waste Manag. 11 (2009) 305–311.

[57]   W. Urban, H. Lohmann, J.I.S. Gómez, Catalytically upgraded landfill gas as a cost-effective alternative for fuel cells, Journal of Power Sources. 193 (2009) 359–366.

[58] K. Badjagbo, M. Héroux, M. Alaee, S. Moore, S. Sauvé, Quantitative Analysis of Volatile Methylsiloxanes in Waste-to-Energy Landfill Biogases Using Direct APCI-MS/MS, Environ. Sci. Technol. 44 (2010) 600–605.

[59] S. Rasi, J. Lehtinen, J. Rintala, Determination of organic silicon compounds in biogas from wastewater treatments plants, landfills, and co-digestion plants, Renewable Energy. 35 (2010) 2666–2673.

[60] M. Arnold, T. Kajolinna, Development of on-line measurement techniques for siloxanes and other trace compounds in biogas, Waste Management. 30 (2010) 1011–1017.

[61] G. Piechota, M. Hagmann, R. Buczkowski, Removal and determination of trimethylsilanol from the landfill gas, Bioresource Technology. 103 (2012) 16–20.

[62] C. Clark, R.G. Zytner, E. McBean, Analyzing volatile organic siloxanes in landfill biogas, Can. J. Civ. Eng. 39 (2012) 667–673.

[63] J. Läntelä, S. Rasi, J. Lehtinen, J. Rintala, Landfill gas upgrading with pilot-scale water scrubber: Performance assessment with absorption water recycling, Applied Energy. 92 (2012) 307–314.

[64] O. Sevimoğlu, B. Tansel, Effect of persistent trace compounds in landfill gas on engine performance during energy recovery: A case study, Waste Management. 33 (2013) 74–80.

[65] G. Piechota, B. Igliński, R. Buczkowski, Development of measurement techniques for determination main and hazardous components in biogas utilised for energy purposes, Energy Conversion and Management. 68 (2013) 219–226.

[66] J. Raich-Montiu, C. Ribas-Font, N. de Arespacochaga, E. Roig-Torres, F. Broto-Puig, M. Crest, L. Bouchy, J.L. Cortina, Analytical methodology for sampling and analysing eight siloxanes and trimethylsilanol in biogas from different wastewater treatment plants in Europe, Analytica Chimica Acta. 812 (2014) 83–91.

[67] S.C. Surita, B. Tansel, A multiphase analysis of partitioning and hazard index characteristics of siloxanes in biosolids, Ecotoxicology and Environmental Safety. 102 (2014) 79–83.

[68] B. Tansel, S.C. Surita, Oxidation of siloxanes during biogas combustion and nanotoxicity of Si-based particles released to the atmosphere, Environmental Toxicology and Pharmacology. 37 (2014) 166–173.

[69] N. de Arespacochaga, C. Valderrama, C. Mesa, L. Bouchy, J.L. Cortina, Biogas deep clean-up based on adsorption technologies for Solid Oxide Fuel Cell applications, Chemical Engineering Journal. 255 (2014) 593–603.

[70] G. Piechota, R. Buczkowski, Development of chromatographic methods by using direct-sampling procedure for the quantification of cyclic and linear volatile methylsiloxanes in biogas as perspective for application in online systems., International Journal of Environmental Analytical Chemistry. 94 (2014) 837–851.

[71] G. Piechota, B. Igliński, R. Buczkowski, An experimental approach for the development of direct-absorption sampling method for determination of trimethylsilanol and volatile methylsiloxanes by the GC-MS technique in landfill gas, International Journal of Environmental Analytical Chemistry. (2015) 1–11.

[72] C.A. Hepburn, P. Vale, A.S. Brown, N.J. Simms, E.J. McAdam, Development of on-line FTIR spectroscopy for siloxane detection in biogas to enhance carbon contactor management, Talanta. 141 (2015) 128–136.

[73] E. Gallego, F.J. Roca, J.F. Perales, X. Guardino, E. Gadea, Development of a method for determination of VOCs (including methylsiloxanes) in biogas by TD-GC/MS analysis

using Supel™ Inert Film bags and multisorbent bed tubes, International Journal of Environmental Analytical Chemistry. 95 (2015) 291–311.

[74]   S.C. Surita, B. Tansel, Preliminary investigation to characterize deposits forming during combustion of biogas from anaerobic digesters and landfills, Renewable Energy. 80 (2015) 674–681.

[75]   B. Tansel, S.C. Surita, Selectivity and limitations of carbon sorption tubes for capturing siloxanes in biogas during field sampling, Waste Management. 52 (2016) 122–129.

[76]   A. Trapote, M. García, D. Prats, The elimination of siloxanes from the biogas of a wastewater treatment plant by means of an adsorption process, Water Science and Technology. 74 (2016) 2927–2934.

[77]   L. Xu, S. Xu, L. Zhi, X. He, C. Zhang, Y. Cai, Methylsiloxanes Release from One Landfill through Yearly Cycle and Their Removal Mechanisms (Especially Hydroxylation) In Leachates, Environ. Sci. Technol. 51 (2017) 12337–12346.

[78]   V. Paolini, F. Petracchini, M. Carnevale, F. Gallucci, M. Perilli, G. Esposito, M. Segreto, L.G. Occulti, D. Scaglione, A. Ianniello, M. Frattoni, Characterisation and cleaning of biogas from sewage sludge for biomethane production, Journal of Environmental Management. 217 (2018) 288–296.

[79]   Y. Li, C.P. Alaimo, M. Kim, N.Y. Kado, J. Peppers, J. Xue, C. Wan, P.G. Green, R. Zhang, B.M. Jenkins, C.F.A. Vogel, S. Wuertz, T.M. Young, M.J. Kleeman, Composition and Toxicity of Biogas Produced from Different Feedstocks in California, Environ. Sci. Technol. 53 (2019) 11569–11579.

[80]   M. Ghidotti, D. Fabbri, C. Torri, Determination of linear and cyclic volatile methyl siloxanes in biogas and biomethane by solid-phase microextraction and gas chromatography-mass spectrometry, Talanta. 195 (2019) 258–264.

[81]   N. Wang, L. Tan, L. Xie, Y. Wang, T. Ellis, Investigation of volatile methyl siloxanes in biogas and the ambient environment in a landfill, Journal of Environmental Sciences. 91 (2020) 54–61.

[82]   E. Dooms, K. Haereens, P. Segers, Laboratory and field study on the analyses of siloxanes in biogas by TD-GC-MS, 9th IWA Odour& VOC, in: Air Emission Conference, Bilbao, Spain, Olores. Org, 2021.

[83]   G. Piechota, Removal of siloxanes from biogas upgraded to biomethane by Cryogenic Temperature Condensation System, Journal of Cleaner Production. 308 (2021) 127404.

Chapter 3 X-ray Fluorescence (XRF) for Temperature Measurement

3.1 Introduction

The previous chapter has demonstrated that the siloxane chemicals are becoming a critical issue in biogas-to-energy processes. Since the majority of biogas-to-energy projects utilize combustion-based method, it is important and valuable to study the combustion phenomenon and chemistry of silicon-based compounds. This project used a flat flame burner to characterize siloxane and silanol flames. However, due to the large number of particles formed inside the flame, traditional methods do not work well for *in-situ* measurements. To obtain the information within a flame with condensed phase particles, a novel combustion diagnostic method Kr Kα X-ray Fluorescence Spectroscopy (XRF) is used. Before applying this method to complex siloxane and silanol flames, this chapter shows the methods and results from an initial study characterizing the flow and temperature profiles of methane flat flames using XRF measurement.

Flat flame burners are valuable tools for fundamental combustion studies and have been used extensively for studies of particle formation [1]-[5], combustion chemistry [6], and diagnostic tool development and calibration [7], to name a few major research applications. A major advantage of 1D burners is that they can have well-defined governing equations and initial and boundary conditions, which makes it possible to emulate more complex combustion processes accurately. Among the different types of flat flame burners, a multi-element diffusion burner (MEDB, by Research Technologies, also called a Hencken burner) can provide highly uniform, stable and nearly adiabatic combustion conditions. Furthermore, separating the fuel and oxidizer

flows eliminates the risk of flashback, while the rapid mixing of fuel and oxidizer above the surface of the burner can still be described by premixed equilibrium models. The inclusion of a central fuel tube (separate from the bulk fuel flow) also enables secondary fuel studies, including the study of particle forming precursors [1][3]-[5]. By stretching the central flame, different reaction zones can be studied via measurements at different heights.

While many studies have used MEDBs as platforms for combustion research, few have evaluated the flow and temperature fields near the surface of the MEDB or other flat flame burners. In the earlier work by De Goey et al. [8], operating conditions to create adiabatic flames using flat flame burners were presented. Due to the lack of advanced non-intrusive measurement techniques, the study used the uniformity of burner plate temperature to confirm adiabatic flame conditions. Later work by Hancock et al. [9] applied coherent anti-Stokes Raman scattering (CARS) spectroscopy to measure the axial temperature profile of a larger (38 mm square) MEDB burner with H_2 as the fuel. Measurements at 3.81 cm axial height above the burner (HAB) showed good agreement with equilibrium calculations for different equivalence ratios, and demonstrated that MEDBs are excellent tools for diagnostic development and calibration. Konnov et al. [10] used particle-image velocimetry (PIV) measurements to study the effects of pressure on spatial uniformity of the flame structures of a flat flame burner. The velocity field from 0.54 mm to 3.39 mm HAB was measured, showing that the burner was able to form a uniform 1-D flame front; however, fluctuations and non-uniformities in the flow speeds (in magnitude and direction) were observed. The study by Konnov et al. [10] also noted that it was impossible to measure the flow field below 0.5 mm HAB with this method due to strong reflection of the laser light sheet from the burner surface. The study by Belmont et al. [11] used OH planar laser-induced fluorescence (OH PLIF) to quantify the disruption of the flame when a sampling probe was inserted into the flame

54

at heights from 9 to 23 mm above the burner surface. The measurements showed flame front displacements from 0.5 to 2.7 mm due to physical sampling. In more recent studies by Wang et al. [12] and Gu et al. [13], the impact of heat losses on temperature uniformity were investigated. Both studies found it was common for flame temperature to be lower than the predicted adiabatic temperature due to heat transfer effects.

These past studies demonstrate quantitative information with high spatial resolution, including temperature, velocity, and species concentration data, is valuable for flat flame burner research applications. The previous studies also show the value of non-intrusive methods that do not disrupt the flow and that can interrogate regions close to the surface of the burner, particularly below 0.5 mm HAB.

The objective of this study was to characterize the combustion system created by an MEDB using high-fidelity, non-intrusive measurements, in particular to provide new data on the mixing region near the surface of the burner. The technical approach used Kr Kα x-ray fluorescence (XRF) spectroscopy as an in-situ, non-invasive diagnostic method to quantify the combustion system, including fuel and air mixing very near the surface of the burner (e.g., within 2 mm of the burner surface) and temperature profiles of the burner flame. XRF has traditionally been used for non-destructive elemental analysis of solid and liquid samples in material and biological areas [14]. However, in recent years, researchers have extended XRF to gas phase measurements [15]-[18] due to the attractive features of the method, including high energy penetration, insensitivity to temperature spectral broadening and high spatial fidelity.

Another benefit of this technique is that x-rays effectively only interact with the Kr tracer in the flow. Consequently, if there are particles generated during combustion, they have no impact on the signal [17]. Although the work in this chapter did not produce particles in the flame, this is

a necessary feature for future gas-phase studies of systems with condensed phase reactants and products. Highly resolved XRF scans from multiple planar locations and at different heights above the burner surface were used in the current work to characterize the MEDB flow at reacting and non-reacting conditions. The results are compared with model predictions for a 1D system.

3.2 Methods

3.2.1 Multi-element Diffusion Burner

A schematic of the experimental setup utilized in this study is shown in **Figure 3.1**. The details of the MEDB [1][19] and the XRF [15][16] set-up have been described previously. Therefore, only brief descriptions of each are provided here. The MEDB consists of an array of small stainless-steel tubes aligned in a square honeycomb matrix with an overall dimension of 2.5 cm × 2.5 cm. The primary fuel is delivered through the fuel tubes (0.508 mm inner diameter), while the oxidizer flows through the remaining channels of the honeycomb matrix (where each honeycomb channel has a circumdiameter of 0.801 mm). The primary fuel and oxidizer are mixed rapidly above the burner surface and create a highly uniform and steady nominally flame sheet. A central tube can be used to deliver secondary fuels, e.g., particle precursors, where the use of the central fuel tube is optional based on the research objective. In the current work, methane (CH_4) was used as the primary fuel and dry-grade air was used as the oxidizer. The central tube was either not used or a flow of nitrogen premixed with 3% Kr by volume was used to study the influence of the central fuel tube on the primary flow. A shroud co-flow of N_2 (6.4 mm wide) was used for all experiments in order to minimize the impact of ambient air. Additionally, a chimney was used to isolate the burner from room air, which was made by 0.13 mm thick Kapton film wrapped around the outside of the burner (forming a cylindrical shape aligned with the axis of the gas flow). The flow rates used in the current work are listed in **Table 3.1**, and the gases used for each test

configuration are listed in **Table 3.2**. For the reacting conditions, the methane and air flow rates correspond to a global equivalence ratio of 0.8.

Table 3.1 Flow rates used in the MEDB XRF studies

	Gas	Flow rate [sccm]
Primary fuel	CH_4	166
	Kr	5.68
Oxidizer	air	1984
	Kr	67.8
Central tube	3% Kr/N_2 mixture	200
Shroud	N_2	3000

Table 3.2 Experimental conditions studied

Scan	Scan Range	Fuel	Oxidizer	Central Flow
Flames w/central flow (x-y)	x: -25 to 25 mm y: 0.1 to 20 mm z: 0 mm	$CH_4 + Kr$	air + Kr	$N_2 + Kr$
Flames w/o central flow (x-y)	x: -25 to 25 mm y: 0.1 to 20 mm z: 0 mm	$CH_4 + Kr$	air + Kr	-
Central jet scan (x-y)	x: -25 to 25 mm y: 0.1 to 0.5 mm z: 0 mm	CH_4	air	$N_2 + Kr$
Fuel jet scan (x-z)	x: -11 to -5 mm y: 0.1 and 0.5 mm z: 13 to 16mm	$CH_4 + Kr$	air	—
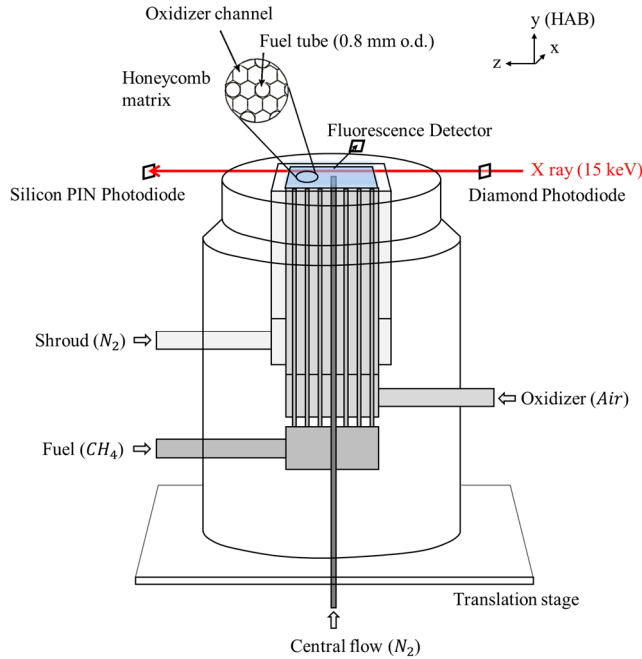
Figure 3.1 Schematic of the structure of the multi-element diffusion burner (MEDB) and the x-ray fluorescence experimental setup used in the current work

3.2.2 Kr K-alpha X-ray Fluorescence Spectroscopy

The study used the 7-BM beamline of the Advanced Photon Source (APS) at Argonne National Laboratory to produce a nearly collimated x-ray beam (15 keV mean photon energy, 0.7% spectral bandpass, 9×10^{10} photons/s incident flux). The beam was focused to a 4×6 μm spot (full width at half maximum intensity). The incident and transmitted power of the x-ray beam were measured using diamond (55 μm thickness) and silicon (300 μm thickness) photodiodes, respectively. Krypton was used as the fluorescence species and was added to the burner gas flows using calibrated mass flow controllers (MKS 1179A, uncertainty: 0.5% of reading plus 0.2% full scale range). During x-ray experiments, Kr is ionized by absorbing an incident x-ray photon and ejecting a K-shell electron. The ion then emits either an Auger electron or an x-ray fluorescence photon as it relaxes [20] on a time scale [21] far smaller than collision times in the flame.

Consequently, electronic quenching is not of concern for this implementation of XRF. The photon emitted at 12.65 keV (K-alpha transition) [22] was captured by an energy-dispersive x-ray detector (silicon drift diode) fitted with a polycapillary x-ray optic (100 mm focal length), set at an angle perpendicular to the x-ray beam but 30° above the horizontal plane to avoid vignetting at the burner surface when measuring positions near the burner surface. Because the x-ray at 12.65 keV is below the K-edge of Kr, and because the density of both the combustion gases and ambient air are quite low, trapping of the fluoresced photon between the point of generation and the detector is negligible. For this work, the center of the burner surface was defined as the (x, y, z) = (0, 0, 0) mm position, where x and z defined the plane parallel to the surface of the burner (z being the incident x-ray propagation direction) and y was the height above burner (HAB). The effective probe volume size, defined by the incident x-ray beam focal spot size and the focal region of the polycapillary was (Δx, Δy, Δz) = (6 µm, 4 µm, 325 µm).

As mentioned previously, the core-hole ions have a much shorter lifetime compared with the collision time in the flame. In addition, the thermal energies at flame temperatures are negligible compared with the shorter wavelength (i.e., hard) x-ray energies. Therefore, other parameters except the Kr number density $n_{Kr}(x,y)$ are not sensitive to temperature in this experiment, and the x-ray fluorescence signal is linearly proportional to the Kr number density in the interaction region between the flow and the incident x-ray beam. The intensity of the x-ray fluorescence is thus related to the Kr concentration and inversely related to the local temperature [16][17][20][23], as shown in Eq. 3.1 and Eq. 3.2

$$I(x,y) = \eta_d \cdot \frac{\Omega}{4\pi} \cdot (1 - f_{abs}) \cdot \omega \cdot \Delta t \cdot \Delta z \cdot \pi R_p^2 \cdot \sigma_{Kr} \cdot \phi \cdot n_{Kr}(x,y) \qquad 3.1$$

$$n_{Kr}(x,y) = \frac{\chi_{Kr}(x,y)\cdot p}{R\cdot T(x,y)} \quad (mol/m^3) \qquad\qquad 3.2$$

where $I(x,y)$ is the x-ray fluorescence signal, η_d is the detector efficiency, Ω is the solid angle viewed by the detector, f_{abs} is the fraction of emitted photons absorbed by media *en route* to the detector, ω is the fluorescence yield, Δt is the measurement collection time, Δz is the detector field of view along the beam propagation path, R_p is the radius of the incident beam, σ_{Kr} is the absorption cross section of krypton at the incident wavelength, ϕ is the incident photon flux, $n_{Kr}(x,y)$ is the local Kr number density, $\chi_{Kr}(x,y)$ is the local Kr mole fraction, p is the pressure (1 atm for these studies), T is the local temperature, and R is the universal gas constant. To map the Kr distribution in the flow fields, the burner was raster scanned in the x and y directions. To measure distributions on planes perpendicular to the overall flow direction, the burner was raster scanned in the x direction while the detector platform was raster scanned in the z direction. The silicon-drift diode integrated the XRF signal at each measurement location for 1 s.

For the cold-flow conditions (i.e., with no flame), Eq. 3.1 and Eq. 3.2 can be used to calibrate the Kr number density distribution assuming the temperature is homogeneous and equal to room temperature. The calculated Kr number density can then be further used to transform the fluorescence field to temperature. For each experiment, a reference scan of the cold flow was made without the methane flow, i.e., at non-reacting conditions. 2D and 1D profile results for a typical cold-flow experiment are shown in **Figure 3.2**. The corresponding lit-flame images as-recorded XRF intensity data are provided in the supplementary material in Appendix B:, for reference. Each reacting flow data set was corrected using the cold-flow reference scan to obtain a relative value of Kr number density. The results in **Figure 3.2** show excellent uniformity in Kr density (~1.27% variation) in the imaging plane (e.g., x = ±10 mm to y = 15 mm). In the current study, temperatures are only interpreted within this region of uniform Kr mole fraction, since measurement fidelity is

drastically reduced in regions with lowered Kr mole fraction. (For additional discussion on this topic, please see Banyon et al. [18]). For the cold flow conditions, the Kr was transported outward towards the shroud flow ($|x| > 15$ mm) and mixed with the shroud and room air above approximately y = 18 mm. The increase in Kr at the edges of the line plot (i.e., $|x| > 20$ mm) at HAB = 1 mm in **Figure 3.2** indicates a small amount of Kr was recirculated into the room air. This has negligible impact on the main flow measurements due to the protection by the N_2 shroud flow.
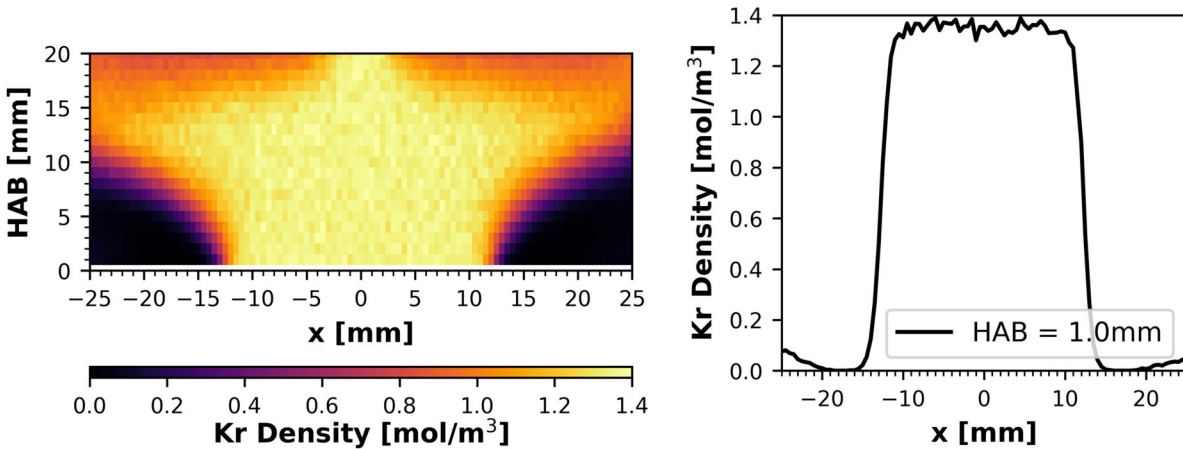
Figure 3.2 Typical results of a 2D Kr XRF scan (left) acquired at cold-flow/non-reacting conditions and used as a reference for reacting conditions. The right panel is a line plot at HAB = 1 mm of the 2D scan.

3.3 Results and Discussion

In addition to the cold flow measurements, XRF scans were made to characterize the flow and mixing associated with the main portion of the MEDB and the central fuel tube during combustion. **Figure 3.3** shows the Kr density results with and without the use of the central tube flow during combustion, where methane was only used in the main flow of the burner. The corresponding XRF intensity data are provided in the supplementary material in Appendix B:, for reference. The figure includes both 2-D results and line-plots of the measured Kr number density. For these experiments 3% Kr/N_2 flow was used for the central fuel tube with a flow rate of 200

standard cm^3/min (sccm). Due to the inverse relationship between the Kr number density and temperature (Eq. 3.2), higher Kr number density indicates higher Kr concentration and/or lower temperature. From the cold flow scan (**Figure 3.2**), the relative Kr density was nearly homogeneous in the main flow region. Accordingly, a conclusion can be made that in the main flame region, the low signal intensity was primarily due to heat release in the flame which decreased bulk gas density. As seen in **Figure 3.3**, there was a region of high Kr number density very close to the burner surface (y < 1 mm), indicating a low temperature region upstream of the flame front, which is potentially impacted by the fuel and oxidizer mixing process. Near the edges, the higher Kr density region may be due to heat loss to the shroud flow. The line plots also highlight an asymmetry in the Kr number density near the central fuel tube.

When the central fuel tube was not used, the temperature and mixing were quite uniform with limited variation within the x = ± 5 mm plane for most of the imaging region. When the central tube was used, the imaging indicates some mixing of the central tube gases with the combustion products of the main burner, but the central gas flow remained in a concentrated region, with only a gradual spread and dilution of the jet as it flowed downstream. The effects of the central tube flow on the main combustion gases appeared small in the region above y = ~ 3 mm and x > ±4 mm. However, near the exit of the central tube, there is evidence of gases leaking from the central tube into the vicinity of the main region inside the fuel plenum of the burner assembly. This hypothesis was investigated further with experiments where 200 sccm 3% Kr/N$_2$ flow was supplied through the central tube without the primary flow gases. The results are presented in **Figure 3.4** and show side jet flows are present in the main flow region. Three repeated scans were made, and no significant changes of side-jet intensities were observed. Thus, it is unlikely the side jets were caused by residual Kr flow in the main burner plenums. The results

indicate imperfect isolation of the central tube from the main region of the burner. The line plot in

Figure 3.4 indicates three tubes in each direction (+x and -x) adjacent to the central fuel tube

directions were affected.
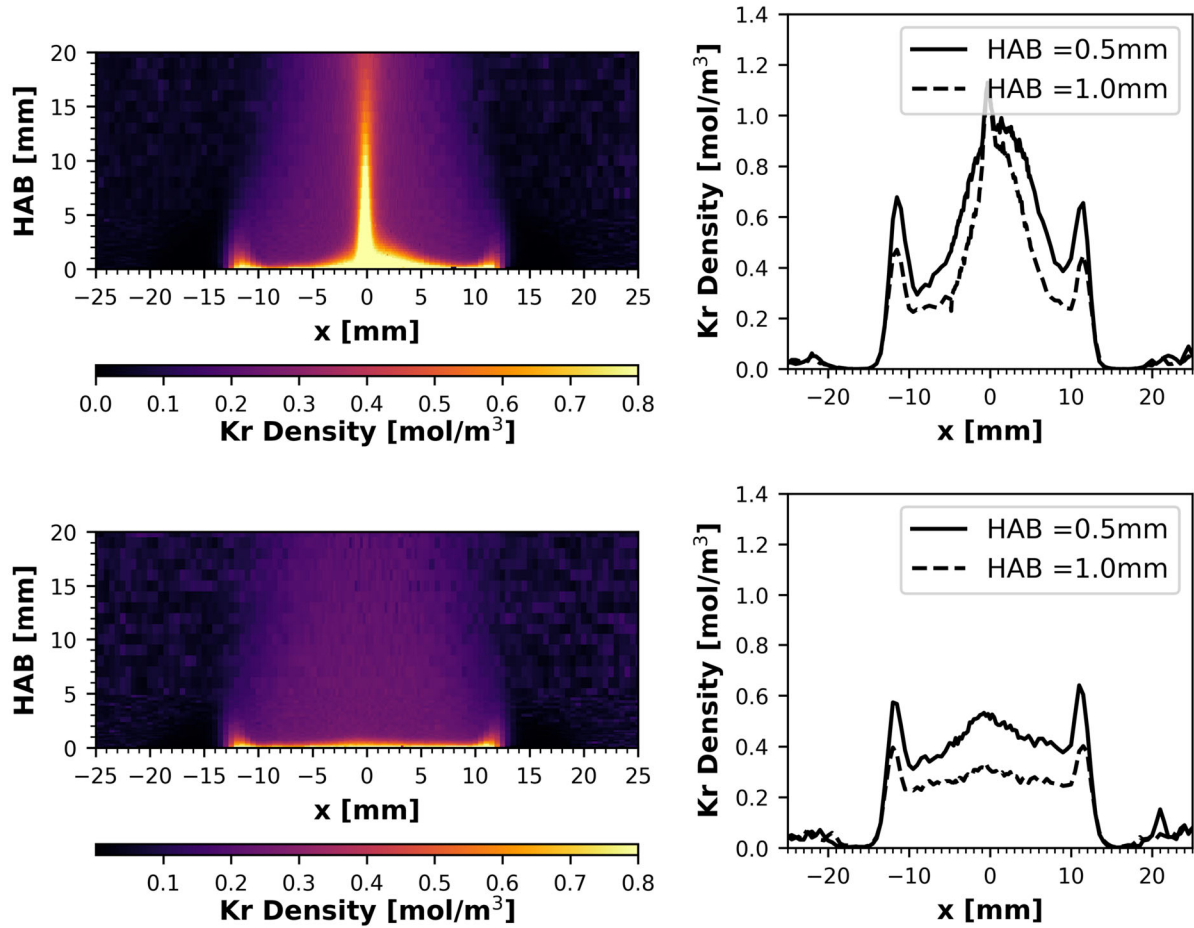
Figure 3.3 XRF results of 2D x-y scans (z = 0 mm; y = HAB) of the burner flames (left panels), with (top panels) and without (bottom panels) Kr flow in the central tube. The right panels are line plots of the corresponding data in the left panels at HAB = 0.5 mm and 1 mm.
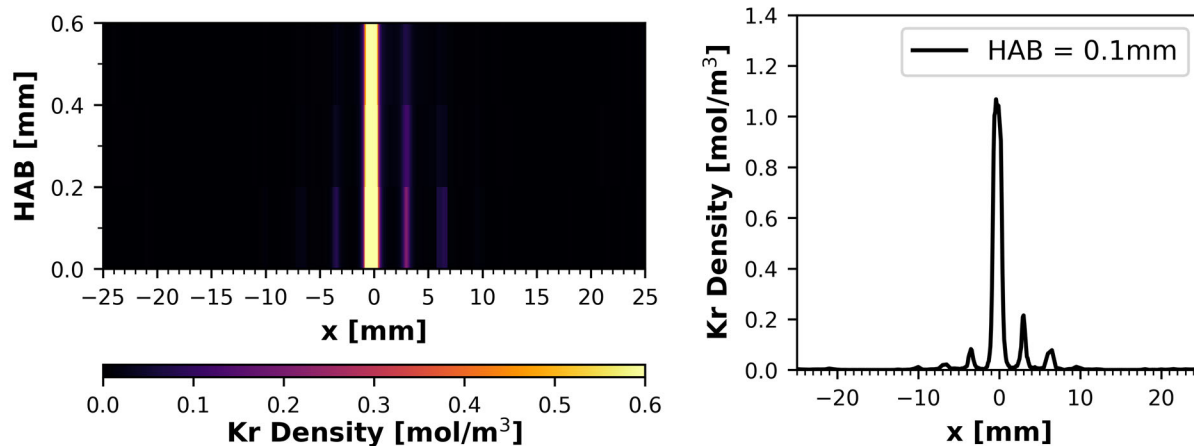
Figure 3.4 XRF results of a 2D x-y scan (left panel, z = 0 mm; y = HAB) of the central tube flow without Kr in the main burner flow gases close to the burner surface, i.e. small HAB. The pale lines show side jet flows on both sides of the central jet flow. The right panel is a line plot of the 2D scan at HAB = 0.1 mm

In addition to the 2D scans in the x-y plane, the fuel jets were scanned in the x-z plane at different heights above the burner to characterize the mixing behavior of fuel and oxidizer near to the burner surface. The air was supplied without Kr, therefore only fuel rich regions are visualized by x-ray fluorescence. Since the burner fuel jets are arranged in a systematic pattern in the honeycomb array, a small representative portion of the burner was scanned. As shown in **Figure 3.5**, at 0.5 mm HAB, the fuel and oxidizer were partially mixed, and the peak intensity at 0.5mm is significantly attenuated compared with the 0.1 mm HAB scan. The decrease in the maximum Kr number density is caused both by mixing and temperature changes, but in this HAB range of 0.1 mm to 0.5 mm, temperature changes would be minor and mixing effects should dominate. The results in **Figure 3.5** show the maximum Kr number density decreased by approximately 67% from HAB = 0.1 mm to HAB = 0.5 mm. Assuming minimal temperature change in this HAB region, the data indicate fuel mixing with the oxidizer flow is rapid and located very near the burner surface.
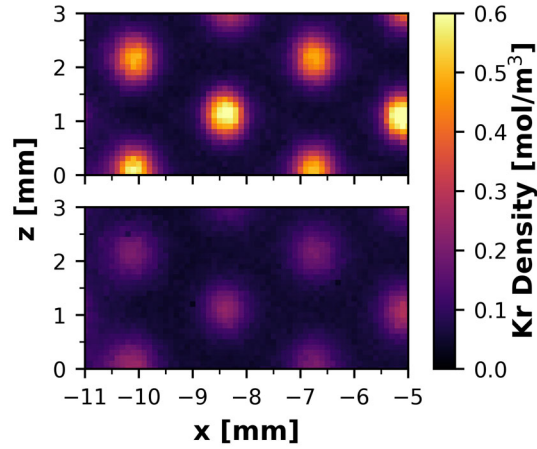
Figure 3.5 XRF results of 2D x-z scans of the main flow region at two heights above the burner surface. The top panel corresponds to HAB = 0.1 mm, and the bottom panel corresponds to HAB = 0.5 mm.

1D vertical Kr densities at x = 0 and x = 5 mm were extracted from the 2D x-y plane measurements with and without the central tube flow and converted to temperature using Eq. 3.1 and Eq. 3.2 and the cold flow scan reference data. The Kr mole fraction $\chi_{Kr}(x, y)$ in Eq. 3.2 was calculated from the flow rates recorded by the mass flow controller during the cold flow scans and the value of χ_{Kr} was assumed constant. This assumption is only valid in the homogeneous region above the burner (HAB < 10 mm). The results of the analysis were compared with temperature predictions using a CHEMKIN [24] premixed burner-stabilized methane flame model and the GRIMech 3.0 reaction mechanism [25]. The GRIMech reaction mechanism was selected for the modeling work because the reaction mechanism was designed, validated and verified primarily for methane and natural gas combustion at atmospheric pressure [25]. The input data for the simulations included the reactant mixture composition (methane and air at an equivalence ratio of 0.8), the reactant mixture temperature (298 K) and pressure (1 atm) and the inlet velocity 6.92 cm/s. The model represented a burner-stabilized flame without heat transfer to the environment, whereas some heat losses are expected in the experiments. The premixed model was chosen to compare with the experimental data in order to verify whether mixing near the burner surface is

sufficiently fast that the flame can be described as "premixed" downstream of the mixing region. Due to these distinctions, the model results are not expected to exactly agree with the experimental data in the mixing region near the surface of the burner (e.g., HAB < 1mm).

Figure 3.6 shows comparisons between the experimental results and the CHEMKIN model predictions of the calculated 1D temperature profiles at x = 0 and x = 5 mm with and without flow through the central tube. Figure 3.7 shows the corresponding 2D temperature distributions (in the regions where the Kr concentration remains homogeneous) with and without the central jet flow of 3% Kr/N_2 mixture. The left panel of Figure 3.6 presents the data along the centerline of the burner, and the results show when the central tube was used, the central jet flow was well isolated from the main flow, yielding a significant low-temperature region along the centerline of the burner. When the central tube was not used, the temperature profile along the centerline was slightly lower than the model predictions near the burner surface (HAB < 2 mm), which is due to the flow disruption caused by unused fuel tube. The off-center temperature data without the central jet flow (presented in the right panel of Figure 3.6) show excellent agreement (within the variability of the experimental data) with the model predictions for a premixed burner-stabilized flame along the entire temperature profile. However, as also seen in the right panel of Figure 3.6, when the central fuel tube was used, the temperature profile was lower than the model predictions, which is attributed to dilution by the observed leakage of gases from the central fuel tube within the body of the burner. At the high locations shown (e.g., HAB > 6 mm), the higher experimentally determined temperature was likely caused by enhanced Kr dilution by ambient air at the hot flow conditions, which leads to a lower Kr mole fraction compared with the cold flow scan data and therefore a higher calculated temperature. The 2D temperature data presented in Figure 3.7 further show that when the perturbation of the flow caused by not using the central fuel tube is avoided,

the temperature field is quite uniform and consistent with adiabatic burner performance, as seen in

the right panel of **Figure 3.7**. And, when the central fuel tube is used, a pyrolysis region is created

along the centerline of the burner as seen in the left panel of **Figure 3.7**.
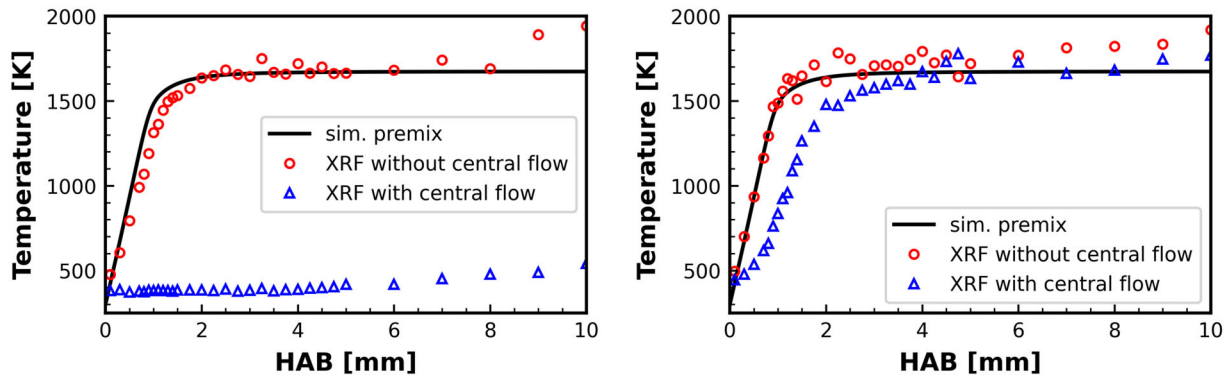
Figure 3.6 Temperature along HAB at x = 0 mm (left panel) and x = 5 mm (right panel), calculated from the experimental fluorescence data and the CHEMKIN modeling results.
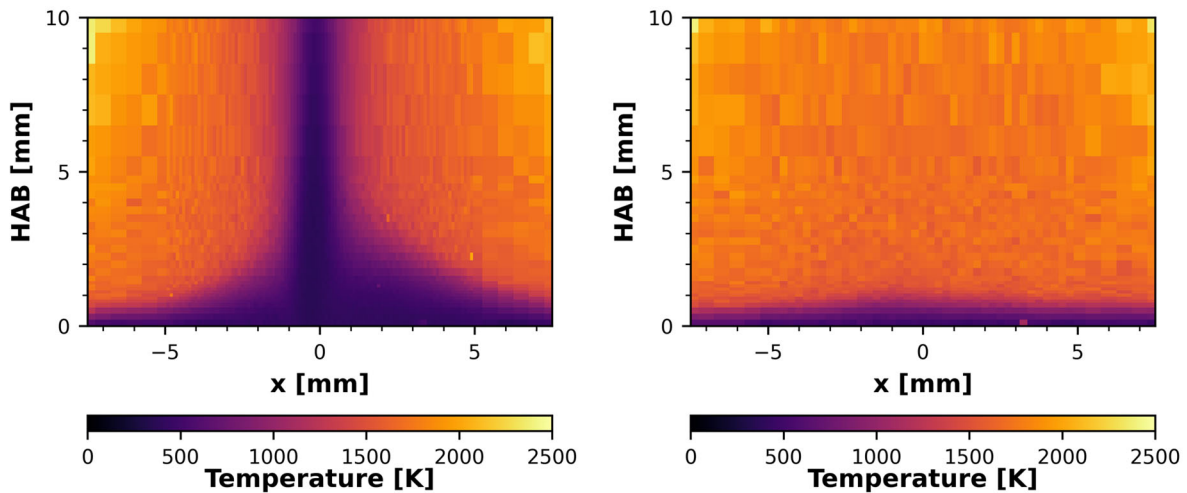
Figure 3.7 Flame temperature distribution in the region of constant Kr density with (left panel) and without (right panel) central jet flow (3% Kr/N$_2$ mixture), calculated from the experimental fluorescence data.

3.4 Conclusions

The present study provides new high-fidelity results on the mixing and thermal characteristics of a MEDB that is an important resource for fundamental combustion studies. The XRF data are the first of their kind for this type of burner and confirmed mixing occurs rapidly between the fuel and oxidizer very near the surface of the burner, with measurable mixing observed at heights less than 0.5 mm above the burner surface. The XRF data showed excellent uniformity in the "far field" of the burner, i.e., heights above 2 mm and for regions of flow offset from the central fuel tube by > 2 mm. The central fuel tube flow was found to affect adjacent fuel tube flows, indicating the flow to the central fuel tube was leaking to the main fuel region. However, the central flow indicated good symmetry and well-behaved laminar jet characteristics for the significant heights above the surface of the burner. Temperature determinations based on the Kr data yielded excellent agreement with 1D model predictions for a premixed burner-stabilized methane flame for regions unaffected by flow through the central tube (i.e., 5 mm away from the centerline of the burner). Overall, the results confirm the MEDB is an excellent tool for studies that require steady well-controlled combustion conditions, and the results identified regions of substantial uniformity required for many combustion studies. Importantly, the study also confirmed the feasibility and utility of XRF to study mixing, diffusion and heat loss characteristics of the baseline methane combustion system, with the benefits of outstanding spatial resolution and insensitivity to particles in the flow. The 2D imaging data obtained in the current work provide new detailed information about the MEDB flow fields and are a valuable foundation for fundamental combustion research.

3.5 Citations

[1]   M.S. Wooldridge, P.V. Torek, M.T. Donovan, D.L. Hall, T.A. Miller, T.R. Palmer, C.R. Schrock, An experimental investigation of gas-phase combustion synthesis of SiO_2 nanoparticles using a multi-element diffusion flame burner, Combust. Flame 131 (2002) 98–109.

[2]   D. Khatri, A. Gopan, Z. Yang, A. Adeosun, R.L. Axelbaum, Characterizing early stage sub-micron particle formation during pulverized coal combustion in a flat flame burner, Fuel 258 (2019) 115995.

[3]   S.D. Bakrania, T.A. Miller, C. Perez, M.S. Wooldridge, Combustion of multiphase reactants for the synthesis of nanocomposite materials, Combust. Flame 148 (2007) 76-87.

[4]   S.D. Bakrania, C. Perez, M.S. Wooldridge, Methane-assisted combustion synthesis of nanocomposite tin dioxide materials, Proc. Combust. Inst. 31 (2007) 1797-1804.

[5]   T.A. Miller, S.D. Bakrania, C. Perez, M.S. Wooldridge, A new method for direct preparation of tin-dioxide nanocomposite materials, J. Mater. Res. 20 (2005) 2977-2987.

[6]   F.N. Egolfopoulos, N. Hansen, Y. Ju, K. Kohse-Höinghaus, C.K. Law, F. Qi, Advances and challenges in laminar flame experiments and implications for combustion chemistry, Prog. Energy Combust. Sci. 43 (2014) 36–67.

[7]   N.R. Grady, R.W. Pitz, C.D. Carter, K.-Y. Hsu, Raman scattering measurements of mixing and finite-rate chemistry in a supersonic reacting flow over a piloted, ramped cavity, Combust. Flame 165 (2016) 310–320.

[8]   L.P.H. De Goey, A. Van Maaren, R.M. Quax, Stabilization of adiabatic premixed laminar flames on a flat flame burner, Combust. Sci. Technol. 92 (1993) 201-207.

[9]   R.D. Hancock, K.E. Bertagnolli, R.P. Lucht, Nitrogen and hydrogen CARS temperature measurements in a hydrogen/air flame using a near-adiabatic flat-flame burner, Combust. Flame 109 (1997) 323-331.

[10]   A.A. Konnov, R.Riemeijer, V.N. Kornilov, L.P.H. De Goey, 2D effects in laminar premixed flames stabilized on a flat flame burner, Exp. Therm. Fluid Sci. 47 (2013) 213-223.

[11]   E. Belmont, T. Ombrello, M. Brown, C. Carter, J. Ellzey, Experimental and numerical investigation of freely propagating flames stabilized on a Hencken Burner, Combust. Flame 162 (2015) 2679-2685.

[12]   P. Wang, X. Luo, Q. Li, Heat transfer study of the Hencken burner flame, Flow Turbul. Combust. 101 (2018) 795-819.

[13]   M. Gu, S. Wang, G. Wang, Q. Wang, X. Liu, F. Qi, C.S. Goldenstein, Improved laser absorption spectroscopy measurements of flame temperature via a collisional line-mixing model for CO_2 spectra near 4.17 μm, Appl. Phys. B 128 (2022) 1-12.

[14]   B. Beckhoff, ed., Handbook of practical X-ray fluorescence analysis, Springer, Berlin ; New York, 2006.

[15]   R.S. Tranter, A.L. Kastengren, J.P. Porterfield, J.B. Randazzo, J.P.A. Lockhart, J.H. Baraban, G.B. Ellison, Measuring flow profiles in heated miniature reactors with x-ray fluorescence spectroscopy, Proc. Combust. Inst. 36 (2017) 4603–4610.

[16]   N. Hansen, R.S. Tranter, K. Moshammer, J.B. Randazzo, J.P. Lockhart, P.G. Fugazzi, T. Tao, A.L. Kastengren, 2D-imaging of sampling-probe perturbations in laminar premixed flames using Kr x-ray fluorescence, Combust. Flame 181 (2017) 214-224.

[17] M.J. Montgomery, H. Kwon, A.L. Kastengren, L.D. Pfefferle, T. Sikes, R.S. Tranter, Y. Xuan, C.S. McEnally, In situ temperature measurements in sooting methane/air flames using synchrotron x-ray fluorescence of seeded krypton atoms, Sci. Adv. 8.17 (2022) eabm7947.

[18] C. Banyon, M.J. Montgomery, H. Kwon, A.L. Kastengren, L.D. Pfefferle, T. Sikes, Y. Xuan, C.S. McEnally, R.S. Tranter, Temperature measurements of heavily-sooting ethylene/air flames using synchrotron x-ray fluorescence of krypton, Combust. Flame (in press). DOI: 10.1016/j.combustflame.2022.112494

[19] D.L. Hall, A.A. Wang, K.T. Joy, T.A. Miller, M.S. Wooldridge, Combustion synthesis and characterization of nanocrystalline tin and tin oxide (SnO_x, x= 0-2) particles, J. Am. Ceram. Soc. 87 (2005) 2033–2041.

[20] J.A. Bearden, X-ray wavelengths, Rev. Mod. Phys. 39 (1967) 78–124.

[21] J.L. Campbell, T. Papp, Widths of the atomic K–N7 levels, At. Data Nucl. Data Tables 77(1) (2001) 1-56.

[22] R.D. Deslattes, E.G. Kessler, P. Indelicato, L. De Billy, E. Lindroth, J. Anton, X-ray transition energies: new approach to a comprehensive evaluation, Rev. Mod. Phys. 75 (2003) 35-99.

[23] A.C. Eckbreth, *Laser diagnostics for combustion temperature and species*, CRC press, 1996.

[24] ANSYS CHEMKIN 17.0 (15151), ANSYS Reaction Design: San Diego, 2016.

[25] G.P. Smith, D.M. Golden, M. Frenklach, N.W. Moriarty, B. Eiteneer, M. Goldenberg, C.T. Bowman, R.K. Hanson, S. Song, W.C. Gardiner, Jr., V.V. Lissianski, Z. Qin, http://combustion.berkeley.edu/gri-mech/

Chapter 4 Flames Characterization for Organic Silicon Compounds

4.1 Introduction

With an understanding of the presence of organic silicon species in biogas and the fact that the majority waste-to-energy projects utilizing combustion techniques, it is essential to learn about the combustion phenomenon associated with siloxane and silanol flames. Furthermore, trace amounts of siloxanes and silanols have significant impacts on ignition properties of fuels [1][2]. Therefore, studying siloxane reactions in methane flames can help with understanding particle formation mechanism and developing potential methods to mitigate their negative impacts on waste-to-energy facilities.

In addition, besides their roles as impurities in landfill gas and sludge gas utilization, they could potentially be recovered from biogas and utilized as a resource. Siloxanes and silanols are common precursors for flame-based silica nanoparticle synthesis [3], and there is an increasing need for producing bulk nanoparticle materials effectively and economically. An example would be the production of fumed silica by flame pyrolysis of volatile silicon compounds, which has a global market size over a billion dollars and has an increasing demand in various industries such as construction, electronics, transportation, personal care and etc. [4][5]

Flame-based particle synthesis is dominated by many complicated phenomena including mixing, gas-phase chemical kinetics, particle formation (nucleation, condensation and

aggregation) and heterogeneous interactions [6]-[9]. Among key operating conditions, it has been observed previously in many studies that flame temperature plays an important role in controlling the morphology and composition of the particles formed [9]-[12]. Consequently, accurately measuring and controlling the flame temperature are important to predict and obtain the target particle products. In addition, having a detailed temperature map of the flame field can help researchers develop a fundamental understanding of the chemical mechanisms describing oxidation of the precursor and to verify and improve existing chemical kinetics models, which will further help with developing and optimizing processes to make advanced particle materials at scale [8][11].

Temperature measurements in particle laden flames are challenging. For example, physical sensors, like thermocouples, are confounded by particle deposition on the probe, as shown in **Figure 4.1**.
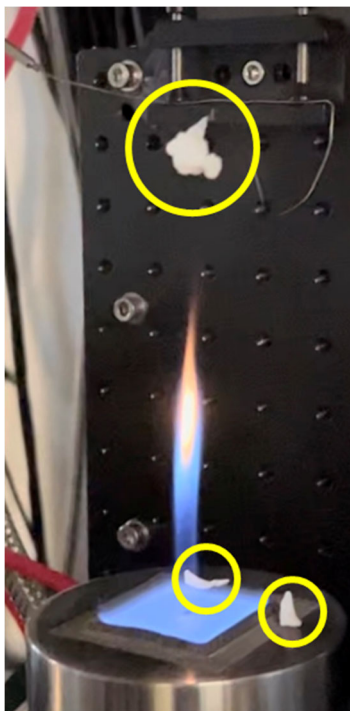
Figure 4.1 Picture of bulk silica particles deposited on a thermocouple above a siloxane flame and fell off on the burner (marked by yellow circles)

Spectroscopic diagnostics, like spectral emission and laser absorption, provide some opportunities for in-situ and non-intrusive measurements of flame temperature and species concentrations [13]-[16]. However, they are limited by scattering from the particles and the high optical density at the typical probe wavelengths [17].

In **Chapter 3**, XRF has been demonstrated for gas phase measurements in a particle-free flame with high spatial fidelity. In the studies by Montgomery et al. [18] and Banyon et al. [19], XRF was used to measure the temperature profiles of highly sooty flames, and the results demonstrated that the soot particles had negligible impact on the XRF signal. In the current work, XRF measurements were explored as a means to measure temperature in laminar synthesis flames with high silica particle densities using hexamethyldisiloxane (HMDSO, $C_6H_{18}OSi_2$) and trimethylsilanol (TMSO, $C_3H_{10}OSi$) as the silica particle precursors, mainly focusing on the precursor reaction region near the burner surface (height above burner HAB < 20 mm). This work also verified the XRF technique's capability with high fidelity gas temperature measurement with condensed phase. The results from the XRF measurement in this study form the basis for more detailed analysis of siloxane chemistry related to silica particle synthesis and waste-to-energy process.

There is quite rich literature on the production of particle materials from siloxanes, but only a limited number of fundamental studies. Of particular relevance to this work is the flame study by Chagger et al. [20] and pyrolytic studies by Chernyshev et al. [21] and Almond et al. [22][23]. Chagger et al. [20] used methane counter-flow diffusion flames doped with HMDSO and emission spectroscopy to study the reaction path from HMDSO to silica, pointing out that there were great uncertainties caused by the unclear HMDSO decomposition mechanism. Fairly recently, Feroughi et al. [24] and Chrystie et al. [25][26] have used optical techniques to determine gas-phase

temperature profiles and measure SiO intermediates in flames. A kinetic model for SiO and SiO₂

formation was used for simulation and compared with experimental data. Finally, Schwind et al.

[2][27] showed dramatic acceleration of the methane ignition chemistry with the addition of trace

quantities (e.g., 100 ppm) of HMDSO or TMSO. The authors hypothesized the reactions pathways

affected by the silicon reactants based on the ignition data. While the structures of HMDSO and

TMSO, shown in **Figure 4.2**, might indicate increased reactivity as a direct source of radicals,

Schwind et al. concluded the interaction of the silicon compounds with the methane ignition

chemistry was likely through H_2/O_2 reactions, e.g., HO_2 and H_2O_2 source and sink reactions

[2][27].

Trimethylsilanol
($C_3H_{10}OSi$)

Hexamethyldisiloxane
($C_6H_{18}OSi_2$)
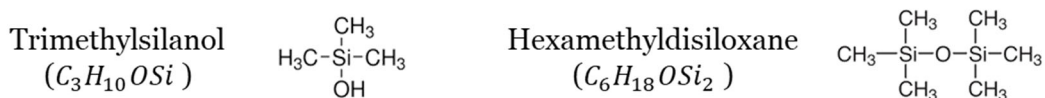
Figure 4.2 Chemical structure of trimethylsilanol (TMSO) and hexamethyldisiloxane (HMDSO).

4.2 Methods

4.2.1 Experimental Setup for XRF Measurement of TMSO and HMDSO flames

A schematic of the experimental setup is shown in **Figure 4.3** and an image of a typical

HMDSO doped flame is shown in **Figure 4.4**. The multi-element diffusion burner (MEDB) used

in the current work has a square honeycomb matrix with dimensions of 36 mm × 36 mm and

overall dimensions of 50 mm × 50 mm when including the surrounding shroud flow region. The

MEDB is similar, but larger than the burner used in Meng et al. [29] and Wooldridge et al.[30].

For the XRF study, methane (ultra-high purity grade, >99.9%, Airgas) was delivered to the fuel

tubes and air (compressed air from wall manifold) was delivered to the surrounding channels. Kr

(≥ 99.995%, Airgas) was the fluorescence medium and doped at 3.2% by volume in the various gas flow. At the center of the burner there is an additional tube through which a third gas stream can be injected into the main flame. In this study, the central jet was used to introduce TMSO (≥ 97.5%, Sigma-Aldrich) or HMDSO (≥ 98%, Sigma-Aldrich) carried by a nitrogen-krypton (nitrogen boiled off from liquid nitrogen supply) mixture made in a mixing tank prior to the experiments. A bubbler was used to introduce the silicon precursor to the central gas flow. Details on the bubbler can be found in Dalmiya et al. [31]. Briefly, the bubbler consisted of a vessel filled with liquid HMDSO or liquid TMSO, and the carrier gas was introduced to the liquid precursor using a glass frit to disperse the gas in the liquid. The carrier gas was considered saturated in HMDSO and TMSO, and the concentrations were calculated based on the vapor pressures at 25 ºC (pvap, HMDSO = 55 mbar [32], TMSO = 29 mbar [33]). For HMDSO this results in a mixture of approximately 5.43% by volume and for TMSO a mixture of approximately 2.86% by volume. A nitrogen shroud flow was used in all experiments to reduce entrainment of room air.

When the burner is ignited, the primary fuel and oxidizer mix rapidly and form a flat flame sheet near the burner surface as seen in **Figure 4.4**. When the central tube includes the particle precursor reactant, a second highly-luminous flame is created that extends vertically above the surface of the burner, as is also seen in **Figure 4.4**.
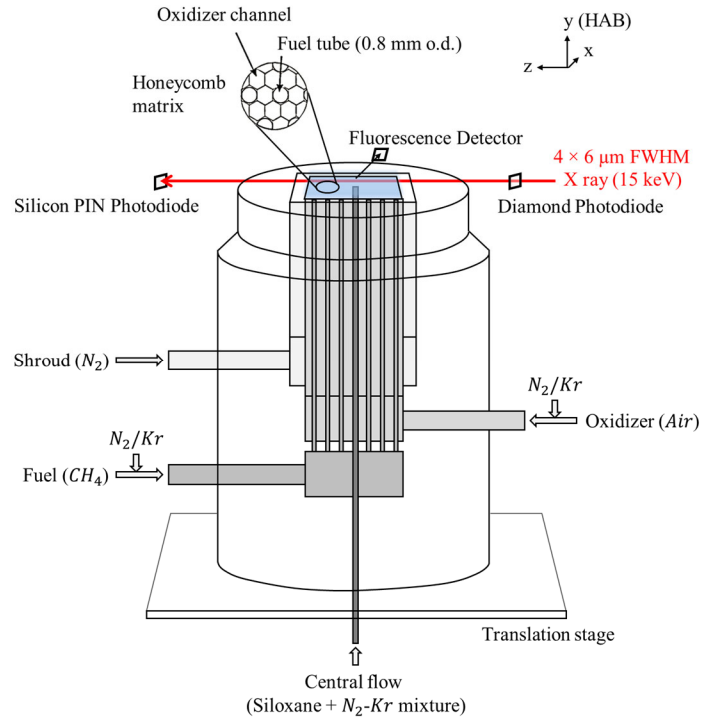
Figure 4.3 Schematic of the structure of the multi-element diffusion burner (MEDB) and the x-ray fluorescence experimental setup used in the current work. [29]

Figure 4.4 Photo of methane flat flame ($\Phi = 1.0$) with HMDSO flame at the center of the burner.

Different flow configurations were used to isolate different effects in the flame systems. Three fuel-to-air equivalence ratios were used, namely fuel-lean, stoichiometric and fuel-rich conditions for the primary methane flame. **Table 4.1** provides the flow rates for each equivalence ratio. **Table 4.2** provides details of the flow configurations in terms of the gases used and identifies the scanned regions above the surface of the burner. The cartesian coordinate system is oriented as shown in **Figure 4.3** with the origin (x=0, y=0, z=0) at the center of the central jet. During the central jet scans, Kr is only doped in the central jet flow and an additional 3.2% N_2 is doped into the other gas flows.

Table 4.1 Flow rates used for fuel lean, stoichiometric and fuel rich conditions (unit: sccm)

Flows	Fuel Lean $\Phi = 0.83$	Stoichiometric $\Phi = 1.0$	Fuel Rich $\Phi = 1.22$
N2 Shroud	10,000	6,000 / 10,000	10,000
Air	3,900	3200	3200
Air Kr (or N_2)	130	106	106
Fuel	340	340	410
Fuel Kr (or N_2)	11.5	11.5	13.8
Central Jet Kr-N_2 Mixture	50	50 / 200	50

Table 4.2 Experimental conditions studied

Description	Fuel	Oxidizer	Central Flow
Cold flow	$N_2 + Kr$	air + Kr	$N_2 + Kr$
Methane-air flame	$CH_4 + Kr$	air + Kr	$N_2 + Kr$
Methane-air flame with HMDSO in central jet	$CH_4 + Kr$	air + Kr	$N_2 + Kr + HMDSO$
Methane-air flame with TMSO in central jet	$CH_4 + Kr$	air + Kr	$N_2 + Kr + TMSO$
Central jet scan for HMDSO flame	$CH_4 + N_2$	air + N_2	$N_2 + Kr + HMDSO$
Central jet scan for TMSO flame	$CH_4 + N_2$	air + N_2	$N_2 + Kr + TMSO$

This study used a 15 keV x-ray beam to ionize Kr atoms, which then relax primarily by producing a Kα photon at 12.65 keV by fluorescence. The details of the x-ray beam properties, the XRF experimental setup, and the fluorescence mechanisms have been described previously in

Meng et al. [29]. At the beginning of the experiments, the x-ray beam was focused to 4 × 6 μm cross-section at the center of the burner. A polycapillary x-ray optic focused emitted photons from the probe volume onto an energy dispersive detector (silicon drift diode, 2 mm thick), yielding a probe volume of 4×6×320 μm. Spatially resolved data were obtained by translating the burner while keeping the x-ray beam and fluorescence detector probe volume fixed in space.

The local gas temperature can be determined from the XRF signal as follows. The fluorescence signal is linearly proportional to the Kr number density, as described previously [18][28][34]. With a cold flow reference signal, the Kr number density can be calculated from the fluorescence signal, and the local temperature can be further derived from the Kr number density from idea gas law as shown in Eq. 4.1

$$T(x, y) = \frac{\chi_{Kr}(x,y) \cdot p}{R \cdot n_{Kr}(x,y)} \quad (K)$$
4.1

where $\chi_{Kr}(x, y)$ is the local Kr mole fraction, $n_{Kr}(x, y)$ is the Kr number density, p is the pressure (1 atm for these studies), $T(x, y)$ is the local temperature, and R is the universal gas constant. In the temperature calculation process, Kr dilution by the combustion products is assumed to be negligible. This assumption is reasonable in this study because there is no dilution from methane oxidation since the total mole number of reactants is the same as the total mole number of products in the overall combustion of methane in air. For HMDSO and TMSO oxidation, the products will dilute Kr, but because of the small amount of those reactants in the flame, the impact of dilution on the flame temperature calculation is less than 0.7% for HMDSO and less than 0.3% for TMSO.

The temperature uncertainties were calculated using Eq. 4.2, which was derived by Banyon et al. [19]

$$dT^2 = T_{ref}^2 \left(\frac{\chi_{Kr}}{\chi_{Kr,ref}}\right)^2 \left(\frac{I_{ref}}{I}\right)^2 \left[\left(\frac{dT_{ref}}{T_{ref}}\right)^2 + \left(\frac{d\chi_{Kr}}{\chi_{Kr}}\right)^2 + \left(\frac{d\chi_{Kr,ref}}{\chi_{Kr,ref}}\right)^2 + \left(\frac{dI_{ref}}{I_{ref}}\right)^2 + \left(\frac{dI}{I}\right)^2\right]$$
4.2

where I is the fluorescence signal, the differentials correspond to the full-width uncertainty for each parameter, and the subscript ref represent the cold flow reference scan. It is assumed that the cold flow temperature $T_{ref} = 298K$ and $dT_{ref} = 2K$, and other parameters are obtained from the experiment data. From the uncertainty analysis, the main source of uncertainties came from the detector noise which is reflected in $\frac{dI}{I}$. The temperature uncertainties are shown as the colored shadow in **Figure 4.7, Figure 4.8** and **Figure 4.9** in the results and discussion session.

4.2.2 MEDB Gas Sampling

To study the bulk intermediates formed inside the central siloxane flames, a gas sampling procedure were established. Gas samples were collected by a 1mL air tight syringe (Hamilton Model 1001 SL Syringe) fixed above the burner with a 4-inch needle (Hamilton Large Hub RN Needle, point style 3). The gas in the flame was extracted from selected height above burner (HAB) manually and slowly, about 0.2 mL/s. The gas was then secured in the syringe through a sample lock built on the syringe, and the 4-inch needle was replaced by a 2-inch needle (Hamilton Large Hub RN Needle, point style 5) for GC injection. Particles from the flame were built up inside the 4-inch needle, therefore the needle needed to be cleaned through a thin wire each time before taking the next sample. A GC-FID (SHIMADZU GC-17A) was used to measuring the amount siloxanes in the gas samples.

This study used MEDB with methane main flame and HMDSO central flame. The burner set up is described previously in **4.2.1.** The stoichiometric condition for methane flame was tested, with sampling positions at burner center and at 5 mm, 10 mm, 15 mm HAB.

4.3 Results and Discussion

4.3.1 XRF results

Figure 4.5 shows the Kr density map of a stoichiometric methane flame with and without HMDSO or TMSO in the central jet. Line plots of the Kr number density at multiple heights above the burner (HAB) are included in **Figure 4.5**. The temperature profiles calculated from the Kr number density data are shown in **Figure 4.6**. The apparently high temperature regions at the top edges of the 2D plots in **Figure 4.6** are artifacts caused by the dilution of Kr by the shroud flow. As seen in the figures, when there was no silicon-containing dopant, the central jet had a higher Kr density and lower temperature, indicating a cold jet flow region isolated from the surrounding flame. When the central jet was doped with HMDSO or TMSO, the centerline Kr number density and hence the temperature at higher HAB (HAB > 9.2 mm) became the same as the surrounding flow due to the reaction and mixing of the silicon-containing compounds. The temperature profiles indicate the reaction of the silicon compounds is initiated at low temperatures. However, from the work by Schwind et al. [2], the unimolecular decomposition of TMSO and HMDSO is unlikely to happen under low temperature range (<1000K) due to the high energy barrier for those reactions.
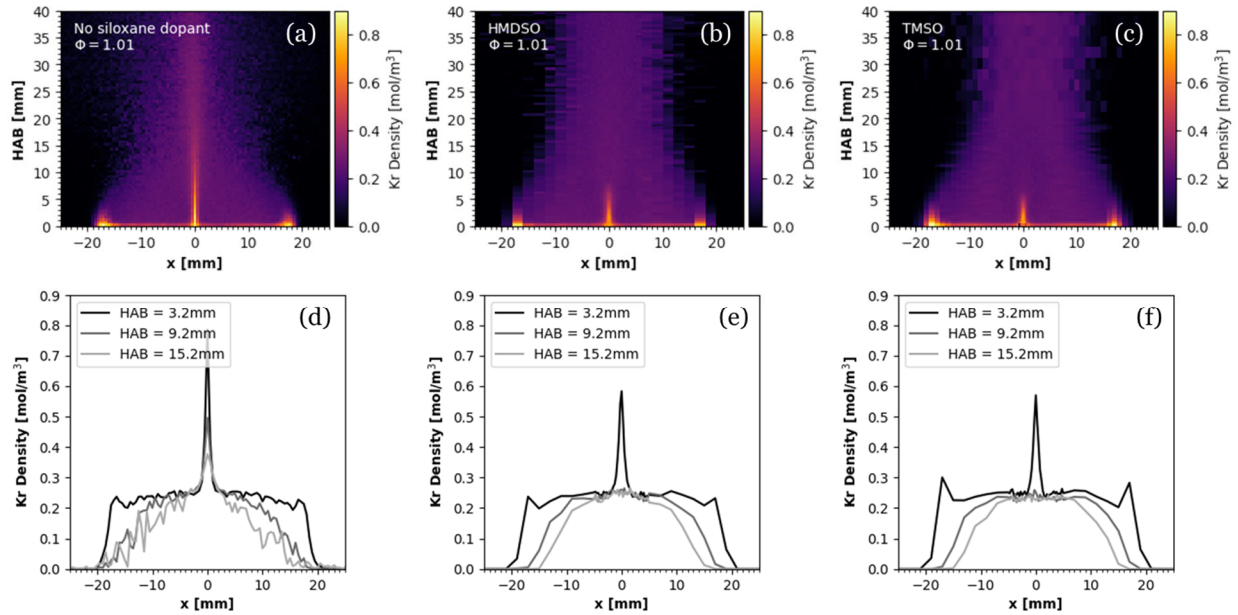
Figure 4.5 XRF results of 2D x-y scans (z = 0 mm; y = HAB) without a silicon-containing reactant in the central jet flow (left panels), with HMDSO in the central jet flow (middle panels) and with TMSO in the central jet flow (right panels). The bottom panels are line plots of the corresponding data in the top panels at three heights above the burner.
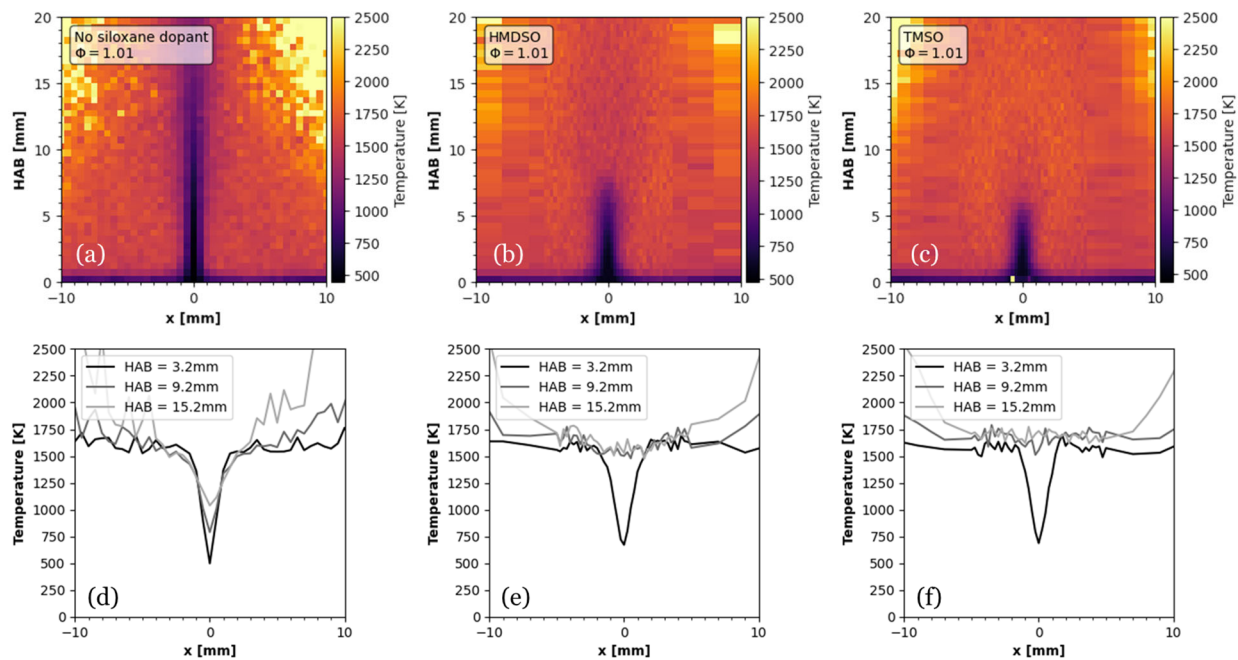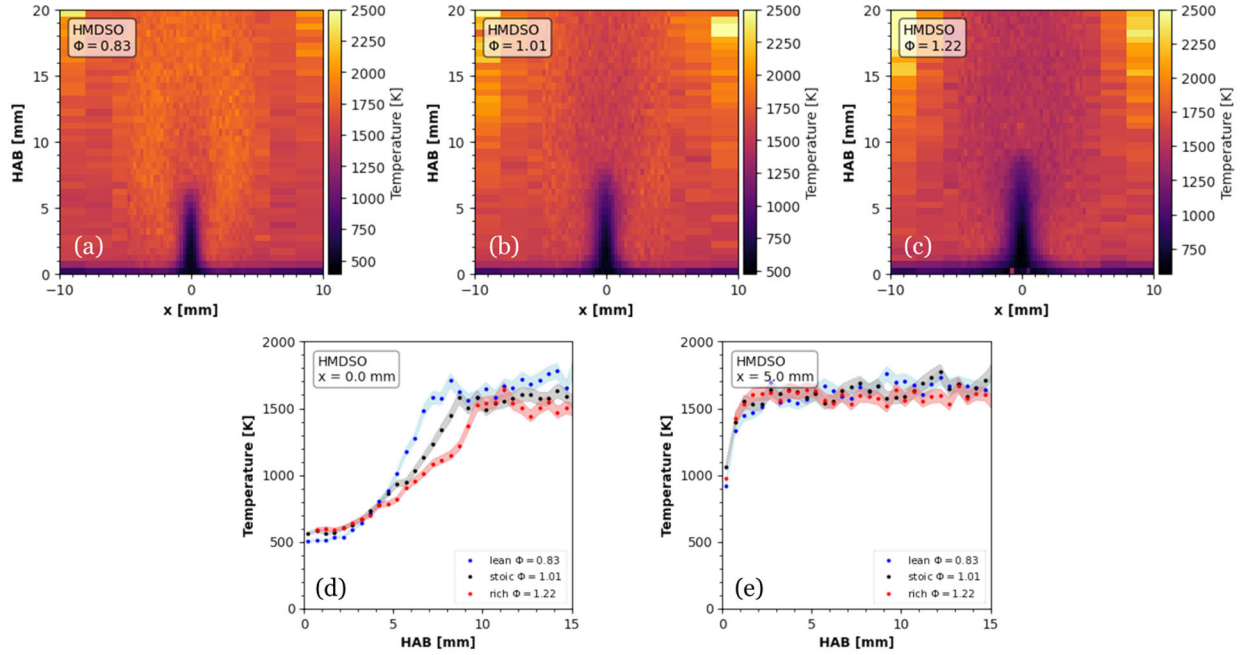

Figure 4.6 Temperature results of 2D x-y scans (z = 0 mm; y = HAB) without a silicon-containing reactant in the central jet flow (left panels), with HMDSO in the central jet flow (middle panels) and with TMSO in the central jet flow (right panels). The bottom panels are line plots of the corresponding data in the top panels at three heights above the burner.

In order to explore the effects of the main flame region on the particle-forming diffusion flame of the central jet, scans with fuel-lean ($\Phi = 0.83$), stoichiometric ($\Phi = 1.0$), and fuel-rich ($\Phi = 1.22$) methane flames were made. The central jet flow rate was kept the same at 50 sccm for all these experiments. The temperature results of the scans are shown in **Figure 4.7** for HMDSO and **Figure 4.8** for TMSO. The equivalence ratio of the methane flat flames has significant impact on the HMDSO and TMSO flames, which is reflected as the difference in the temperature map. The 2D data show that with lower methane flame equivalence ratio, the central flames produced an elliptical region ($|x| < 4$mm, HAB < 20mm) with temperature slightly higher (~ 50 K) than the methane flames. But in fuel rich conditions, this region disappeared and was replaced by a lower temperature area. The differences may be due to changes in reaction chemistry; or the temperature of the methane flames could be different at the three conditions, causing different heat transfer rates to the central flow. To investigate this possibility, temperature line plots were made along the centerline ($x = 0.0$ mm) and in the region of the methane flame where the temperatures were nearly uniform ($x = 5.0$ mm, $dT = +/- 60$ K). From the results for the temperature profiles in the region of the main flame where the methane combustion is unaffected by the central fuel jet (i.e., the offset temperature line plots in the bottom figures of **Figure 4.7** and **Figure 4.8**), it can be seen the methane flame temperature did not change significantly between the three equivalence ratio conditions. However, the temperature along the centerline increased at lower HAB at lean conditions compared with stoichiometric conditions, and increased at higher HAB at rich conditions compared with stoichiometric conditions. This trend was consistent for both HMDSO and TMSO. Therefore, the difference in the centerline temperature is attributed to changes in reaction chemistry and not to changes in heat transfer.

Figure 4.7 Temperature results of 2D x-y scans (z = 0 mm; y = HAB) with HMDSO in the central jet flow. The methane flames were operated at (a) lean, (b) stoichiometric and (c) rich conditions. The bottom panels (d) and (e) show temperature line plots above the burner surface for the different equivalence ratios at the centerline (x = 0.0 mm) and at an offset location (x = 5.0 mm).
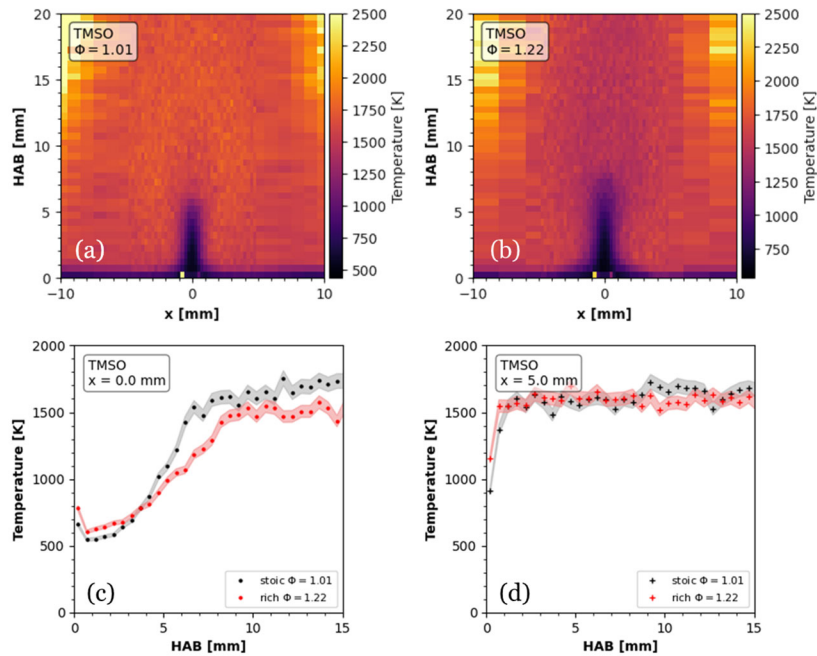

Figure 4.8 Temperature results of 2D x-y scans (z = 0 mm; y = HAB) with TMSO in the central jet flow. The main methane flames were operated at (a) stoichiometric and (b) rich conditions. The bottom panels show temperature line plots above the burner surface for the different equivalence ratios at (c) the centerline and at (d) an offset location.

A comparison between centerline temperature profiles of stoichiometric and rich flames doped with HMDSO and TMSO is shown in **Figure 4.9**. It is interesting to see that even though TMSO has a lower concentration (2.86% by volume) in the central flow than HMDSO (5.43% by volume), the TMSO temperature increases at locations closer to the surface of the burner. Using the constant pressure monatomic ideal gas heat capacity for Kr (20.79 J/mol·K) and polyatomic heat capacity for HMDSO and TMSO (33.26 J/mol·K), the saturated mixture's heat capacity was calculated (21.47 J/mol·K for HMDSO-Kr mixture and 21.15 J/mol·K for TMSO-Kr mixture). Assuming that the same amount of heat has transferred from the main flame to the central gas jet without considering the reactions of HMDSO and TMSO, this difference of heat capacities will only result in about 1.5% in increased temperature. This further indicates the temperature increasing along the centerline is due to reaction kinetics, although the detailed mechanism is still unclear.
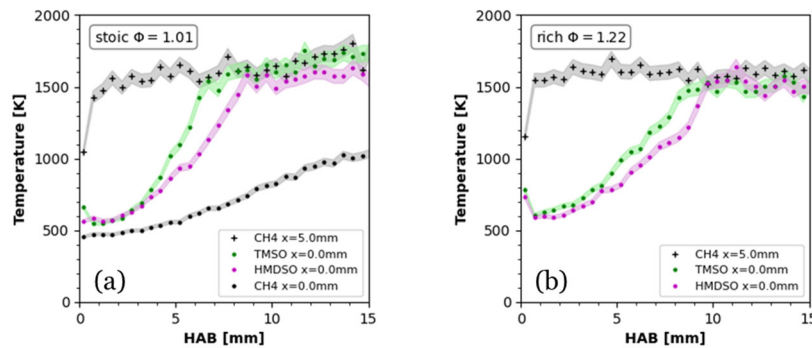
Figure 4.9 Comparison of temperature results above the surface of the burner at (a) stoichiometric conditions (Φ = 1.01) and (b) rich conditions (Φ = 1.22) for non-reacting flow along the centerline (CH₄ x = 0.0 mm), the methane flame region offset from the centerline (CH₄ x = 5.0 mm), for centerline flow with TMSO (TMSO x = 0.0 mm) and for centerline flow with HMDSO (HMDSO x = 0.0 mm).

Another factor that could possibly affect the centerline temperature profile is the mixing of the center flow with the surrounding hot flow in the main combustion region of the burner. To study effects of mixing, scans were made with only Kr added to the central flow while the Kr in

the main flow was replaced by the equivalent amount of N$_2$. Assuming that the flame profiles are the same as the previous scans with Kr doped in both the central and main flows, the Kr concentration can be derived from the previous temperature results and the new XRF central flow scan data using Eq. 4.1. The results of the Kr concentrations are shown in **Figure 4.10** for both HMDSO and TMSO for stoichiometric and fuel rich conditions. The 2D plots are visually quite similar, and the comparison of the 1D centerline data shows the temperatures agree within the scatter of the data.
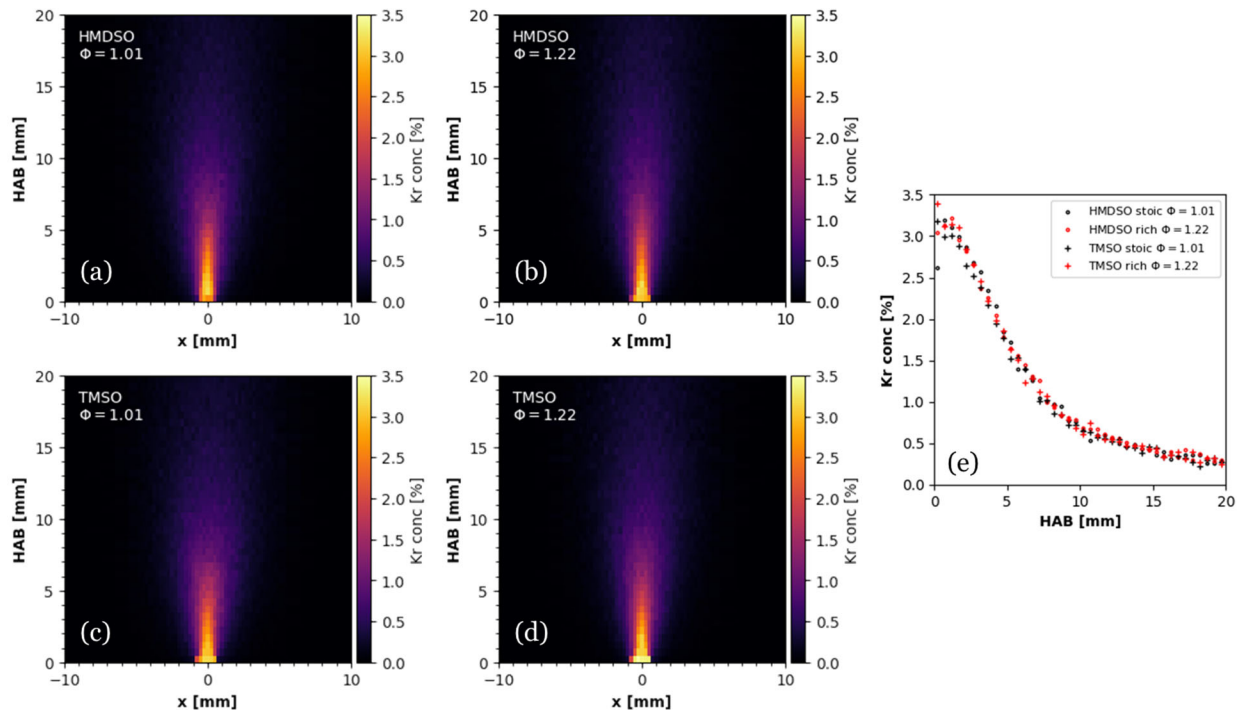
Figure 4.10 2D Kr concentration profiles of central flow scans with HMDSO (upper panels) and TMSO (bottom panels). The main methane flames were at stoichiometric (left panels) and rich (central panels) conditions. The right panel shows the line plots of the Kr concentrations along the centerline associated with the four conditions shown in the 2D scans.

Overall, the results show the HMDSO and TMSO affect the centerline temperature by different amounts depending on the type of reactant added and the equivalence ratio of the main flame. The data indicate that when HMDSO or TMSO is present in the central flow, the increase in temperature observed relative to the baseline case with no silicon-containing compound present

is not due to heat transfer or mixing effects, but rather attributable to reaction of the HMDSO or TMSO. It is interesting to note that reaction is initiated in the low-temperature and low-O_2 region of the burner. The cold flow scans of this region as shown in **Figure 4.9** indicate that the temperatures below ~ HAB= 20m are too low for unimolecular decomposition of HMDSO and TMSO to initiate reactions in the central jet. A possible explanation is the transport of radicals such as OH, H, and O from the methane flame to the cold central flow and these radicals initiate reactions with HMDSO and TMSO. This hypothesis could be validated in the future using diagnostic methods to measure the spatial distribution of these radicals in the flame systems.

4.3.2 Gas sampling results

Table 4.3 Gas sampling results for MEDB HMDSO flames

HAB (mm)	Cold flow TMSO (ppm)	Ignited flow TMSO (ppm)	Cold flow HMDSO (ppm)	Ignited flow HMDSO (ppm)
5	7	220	Saturated	Saturated
10	8	384	Saturated	3071
15	3	5	4076	256

Results of the MEDB gas sampling are shown in **Table 4.3**. For cold flow (non-ignited) tests, the TMSO concentrations remains low (<10ppm), and HMDSO GC peak remains saturated until reaches 15 mm HAB. The TMSO measured in the cold flow came from impurities of the HMDSO chemicals. In the ignited tests, TMSO concentrations in the gas samples collected at 5 mm and 10 mm HAB are largely increased, and HMDSO concentrations drop faster with increased HAB. This indicates that TMSO is an intermediate species formed during HMDSO reactios. Due to the complex structure of the MEDB flame, whether TMSO is a HMDSO pyrolysis product or intermediate of HMDSO oxidation is not immediately evident. Additional studies, beyond the scope of the work presented here, can clarify the potential reaction source of the TMSO observed.

4.4 Conclusions

A key objective of this study was to assess the feasibility of using XRF for gas phase temperature measurements in particle synthesis flames. The results confirm that the high particle density in the flame had negligible impact on the XRF temperature measurement method. The high-fidelity temperature results provide an opportunity to study the flow and temperature profiles in flame systems that have been historically difficult to interrogate with intrusive and non-intrusive diagnostics. The temperature data are particularly valuable for studies of the physical and chemical mechanisms important to particle synthesis.

A second aim of this work was to characterize the temperature profiles of a MEDB burner with a secondary central flame to provide a foundation for studies of siloxane and silanol reaction chemistry. The results showed measurable and distinct impacts of HMDSO and TMSO on the centerline temperature. While HMDSO and TMSO yielded similar temperatures near the surface of the burner (HAB < 4 mm), the TMSO produced higher temperatures compared with HMDSO at HAB > 4 mm). The centerline temperature was also affected by the equivalence ratio of the main flame. The small changes in main flame temperature at different conditions indicated that heat transfer was not a major factor contributing to the changes in centerline temperature.

In addition to the temperature measurements, by doping the central flow with Kr, mixing between the central flow and the main flow was visualized and quantified. The results showed that mixing was similar between the different HMDSO and TMSO flames. When considered together, the findings of this study suggest the changes in centerline temperature are due to the reaction chemistry of HMDSO and TMSO, and that reaction with these compounds starts in a low temperature region, possibly initiated by free radicals from the methane main flame penetrating into the central flow. Direct gas sampling result provided further information that TMSO is

produced in HMDSO flames. Although further experimental investigations are needed to determine the important reaction pathways occurring in the synthesis flame, the insights gained from this study provide new insights and demonstrate a powerful new tool for particle synthesis studies of important siloxane and silanol reactants.

4.5 Citations

[1]   A.B. Mansfield, M.S. Wooldridge, The effect of impurities on syngas combustion, Combustion and Flame. 162 (2015) 2286–2295.

[2]   R.A. Schwind, Understanding the Combustion Chemistry of Siloxanes: Reaction Kinetics and Fuel Interactions, PhD Thesis (2019).

[3]   S.L. Burkett, S.D. Sims, S. Mann, Synthesis of hybrid inorganic–organic mesoporous silica by co-condensation of siloxane and organosiloxane precursors, Chem. Commun. (1996) 1367–1368.

[4]   Fumed Silica Market by Type (Hydrophilic and Hydrophobic), Application (Silicone Elastomers, Paints, Coatings & Inks, Adhesives & Sealants, UPR & Composites), End-Use Industry, and Region - Global Forecast to 2026, MARKETS AND MARKETS, 2021.

[5]   H. Barthel, L. Rösch, J. Weis, Fumed silica-production, properties, and applications, Organosilicon Chemistry Set: From Molecules to Materials. (2005) 761–778.

[6]   M.S. Wooldridge, S.A. Danczyk, J. Wu, Demonstration of gas-phase combustion synthesis of nanosized particles using a hybrid burner, Nanostructured Materials. 11 (1999) 955–964.

[7]   W.Y. Teoh, R. Amal, L. Mädler, Flame spray pyrolysis: An enabling technology for nanoparticles design and fabrication, Nanoscale. 2 (2010) 1324.

[8]   C. Schulz, T. Dreier, M. Fikri, H. Wiggers, Gas-phase synthesis of functional nanomaterials: Challenges to kinetics, diagnostics, and process development, Proceedings of the Combustion Institute. 37 (2019) 83–108.

[9]   D. Dasgupta, P. Pal, R. Torelli, S. Som, N. Paulson, J. Libera, M. Stan, Computational fluid dynamics modeling and analysis of silica nanoparticle synthesis in a flame spray pyrolysis reactor, Combustion and Flame. 236 (2022) 111789.

[10]   S.E. Pratsinis, W. Zhu, S. Vemury, The role of gas mixing in flame synthesis of titania powders, Powder Technology. 86 (1996) 87–93.

[11]   M.T. Swihart, Vapor-phase synthesis of nanoparticles, Current Opinion in Colloid & Interface Science. 8 (2003) 127–133.

[12]   I. Rahinov, J. Sellmann, M.R. Lalanne, M. Nanjaiah, T. Dreier, S. Cheskis, I. Wlokas, Insights into the mechanism of combustion synthesis of iron oxide nanoparticles gained by laser diagnostics, mass spectrometry, and numerical simulations: a mini-review, Energy & Fuels. 35 (2020) 137–160.

[13]   M.T. Donovan, D.L. Hall, P.V. Torek, C.R. Schrock, M.S. Wooldridge, Demonstration of temperature and OH mole fraction diagnostic in SiH4/H2/O2/Ar flames using narrow-line

UV OH absorption spectroscopy, Proceedings of the Combustion Institute. 29 (2002) 2635–2643.

[14] P.V. Torek, D.L. Hall, T.A. Miller, M.S. Wooldridge, H2O absorption spectroscopy for determination of temperature and H2O mole fraction in high-temperature particle synthesis systems, Appl. Opt. 41 (2002) 2274-2284.

[15] M.S. Wooldridge, S.A. Danczyk, J. Wu, Quantitative evaluation of vibrational excitation of SiO A1Π–X1Σ+ flame emission from a silane/hydrogen/oxygen/argon diffusion flame, Journal of Quantitative Spectroscopy and Radiative Transfer. 64 (2000) 573–584.

[16] T.A. Sipkens, J. Menser, T. Dreier, C. Schulz, G.J. Smallwood, K.J. Daun, Laser-induced incandescence for non-soot nanoparticles: recent trends and current challenges, Applied Physics B. 128 (2022) 72.

[17] T. Dreier, C. Schulz, Laser-based diagnostics in the gas-phase synthesis of inorganic nanoparticles, Powder Technology. 287 (2016) 226–238.

[18] M.J. Montgomery, H. Kwon, A.L. Kastengren, L.D. Pfefferle, T. Sikes, R.S. Tranter, Y. Xuan, C.S. McEnally, In situ temperature measurements in sooting methane/air flames using synchrotron x-ray fluorescence of seeded krypton atoms, Science Advances. 8 (2022) eabm7947.

[19] C. Banyon, M.J. Montgomery, H. Kwon, A.L. Kastengren, L.D. Pfefferle, T. Sikes, Y. Xuan, C.S. McEnally, R.S. Tranter, Temperature measurements in heavily-sooting ethylene/air flames using synchrotron x-ray fluorescence of krypton, Combustion and Flame. (2022) 112494.

[20] H.K. Chagger, D. Hainsworth, P.M. Patterson, M. Pourkashanian, A. Williams, The formation of SiO2 from hexamethyldisiloxane combustion in counterflow methane-air flames, Symposium (International) on Combustion. 26 (1996) 1859–1865.

[21] E.A. Chernyshev, T.L. Krasnova, A.P. Sergeev, E.S. Abramova, Siloxanes as sources of silanones, Russ Chem Bull. 46 (1997) 1586–1589.

[22] M.J. Almond, R. Becerra, S.J. Bowes, J.P. Cannady, J.S. Ogden, R. Walsh, A mechanistic study of cyclic siloxane pyrolyses at low pressures, Phys. Chem. Chem. Phys. 10 (2008) 6856.

[23] M.J. Almond, R. Becerra, S.J. Bowes, J.P. Cannady, J.S. Ogden, N.A. Young, R. Walsh, A mechanistic study of the low pressure pyrolysis of linear siloxanes, Phys. Chem. Chem. Phys. 11 (2009) 9259.

[24] O.M. Feroughi, L. Deng, S. Kluge, T. Dreier, H. Wiggers, I. Wlokas, C. Schulz, Experimental and numerical study of a HMDSO-seeded premixed laminar low-pressure flame for SiO2 nanoparticle synthesis, Proceedings of the Combustion Institute. 36 (2017) 1045–1053.

[25] R.S.M. Chrystie, O.M. Feroughi, T. Dreier, C. Schulz, SiO multi-line laser-induced fluorescence for quantitative temperature imaging in flame-synthesis of nanoparticles, Appl. Phys. B. 123 (2017) 104.

[26] R.S.M. Chrystie, H. Janbazi, T. Dreier, H. Wiggers, I. Wlokas, C. Schulz, Comparative study of flame-based SiO2 nanoparticle synthesis from TMS and HMDSO: SiO-LIF concentration measurement and detailed simulation, Proceedings of the Combustion Institute. 37 (2019) 1221–1229.

[27] R.A. Schwind, M.S. Wooldridge, Effects of organic silicon compounds on syngas auto-ignition behavior, Combustion and Flame. 212 (2020) 234–241.

[28] N. Hansen, R.S. Tranter, K. Moshammer, J.B. Randazzo, J.P.A. Lockhart, P.G. Fugazzi, T. Tao, A.L. Kastengren, 2D-imaging of sampling-probe perturbations in laminar premixed flames using Kr X-ray fluorescence, Combustion and Flame. 181 (2017) 214–224.

[29] Q. Meng, C. Banyon, A.L. Kastengren, M.S. Wooldridge, R.S. Tranter, Experimental measurement of the rapid mixing of fuel and air in a multi-element diffusion (Hencken) burner, Combustion and Flame. 251 (2023) 112686.

[30] M.S. Wooldridge, P.V. Torek, M.T. Donovan, D.L. Hall, T.A. Miller, T.R. Palmer, C.R. Schrock, An experimental investigation of gas-phase combustion synthesis of SiO2 nanoparticles using a multi-element diffusion flame burner, Combustion and Flame. 131 (2002) 98–109.

[31] A. Dalmiya, J.M. Mehta, R.S. Tranter, P.T. Lynch, High pressure, high flow rate batch mixing apparatus for high throughput experiments, Review of Scientific Instruments. 92 (2021).

[32] ECHA (European Chemicals Agency), Information on registered substances, (2015).

[33] W.T. Grubb, R.C. Osthoff, Physical properties of organosilicon compounds. II. Trimethylsilanol and triethylsilanol, Journal of the American Chemical Society. 75 (1953) 2230–2232.

[34] J.A. Bearden, X-ray wavelengths, Rev. Mod. Phys. 39 (1967) 78–124.

Chapter 5 HMDSO Impact on Methane Flame Speeds

5.1 Introduction

In **Chapter 4**, HMDSO and TMSO were observed to start reactions at relatively low temperatures. A hypothesis has been suggested that this phenomenon is caused by radicals penetrating into the central jet flow from the methane main flame. In prior work by Schwind [1] using the University of Michigan rapid compression facility, it was proposed that the initial reactions of HMDSO are dominated by H-abstraction from a methyl group by free radicals such as H, OH, HO_2, and CH_3. In addition, in the low-temperature oxidation kinetics study by Wang et al. [2] on dimethyl ether (DME), a potential hydrocarbon surrogate for HMDSO, a model has been developed that at temperatures under 593 K, 93% of DME is consumed through H-abstraction by OH radicals and 6% of DME was consumed through H-abstraction by H radicals. Although the full HMDSO mechanism cannot be developed from DME reactions due to differences in the bonding and structures, the study by Wang et al. may be a good reference to conjecture HMDSO initial reactions at low temperatures because of the commonality of the methyl groups where H-abstraction may initiate in both chemicals.

Although these studies provide some guesses on the reaction mechanism of HMDSO, the H-abstraction hypothesis has not been verified. A recent HMDSO oxidation mechanism developed by Huang et al. [3] using reactive force field (ReaxFF) has proposed other initial reaction paths which mainly include methyl group abstraction (29.8%) and O_2 addition (10.8%), and H-abstraction pathways only contribute to 5.4% of the total number of initial chemical events. The

discrepancy between HMDSO reactions proposed by different studies and between experimental and simulation results underscores the needs for validating and improving the reaction mechanism.

In order to investigate HMDSO reactions in additional flame systems with less complex flame geometries than the MEDB systems described in **Chapter 3** and **Chapter 4**, laminar flame speed experiments were conducted using a spherical laminar flame speed apparatus. Comparing with the MEDB flames in **Chapter 3** and **Chapter 4**, spherical propagating flames have reduced complexity and well established models [4]-[7]. As with the burner studies, methane flames were used for reference experiments and trace addition of HMDSO was added to assess the perturbation of the methane system by the HMDSO chemistry. Sensitivity analysis of methane flame speeds helps to identify the key reactions that have largest impact on the flame speed and the potential impact of HMDSO on these reactions (e.g., via radical production) can be considered. Importantly, HMDSO flame speeds have never been measured previously. Thus, this work is meant to lay the foundation for subsequent studies that will reduce experimental uncertainties and expand the data analysis to more nuanced interpretation. It is acknowledged that the uncertainties in the data presented here may be higher due to the need to develop new experimental protocols to such a novel experimental campaign.

Methods for laminar speed measurement include stationary flame measurements with burners (Bunsen burner, counter flow burner, flat flame burners, etc.) and outwardly propagating spherical flames with constant volume or constant pressure measurements [7]. This study uses the constant pressure method (CPM). Comparing with the burner-based methods, CPM provides the flexibility of changing the initial pressure, the better flame stability, and nearly adiabatic condition, but may have higher facility requirements as it typically requires an optical accessible combustion chamber and a high-speed camera. The accuracy of CPM is affected by the mixture preparation

process, the spark ignition energy, the camera's resolution and frame speed, the flame front identification algorithm, and the flame stretch extrapolation model [8].

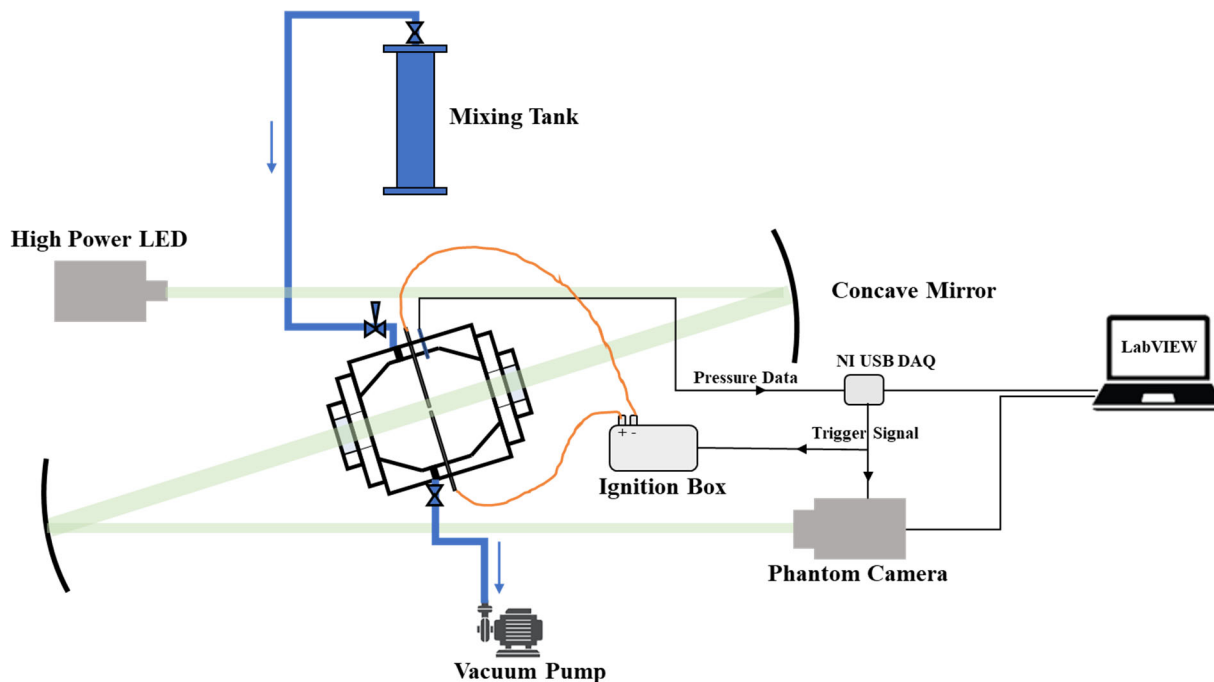## 5.2 Method

5.2.1 Flame Speed Measurement Setup

This work used a quasi-spherical combustion chamber as described in [8] and [9]. The schematic of the chamber is shown in **Figure 5.1**. The quartz windows' diameter is 92 mm, the window-to-window distance is 265 mm, and the cross-sectional diameter at the center is 260 mm. The chamber has 10.6 L volume and can operate up to 40 atm. Two spark electrodes were installed opposingly at the top and bottom center of the burner, which was connected to a custom-made electronics unit. The electrodes were used to generate a spark which ignited the mixture inside the chamber. The spark energy was determined by a capacitor in the electronics unit, which could be changed based on needs. In this experiment, the spark energy was fixed to 30 mJ. This spark energy was selected to ensure that the methane mixtures can be ignited and to ensure the impact of the spark on flame speeds was limited to the initial propagating region. A pressure transducer (kulite ETM-375-250A, pressure range 250 psi) was installed in the chamber and determined the period after ignition when pressure of unburned gas had minimal change ($< 1\%$).
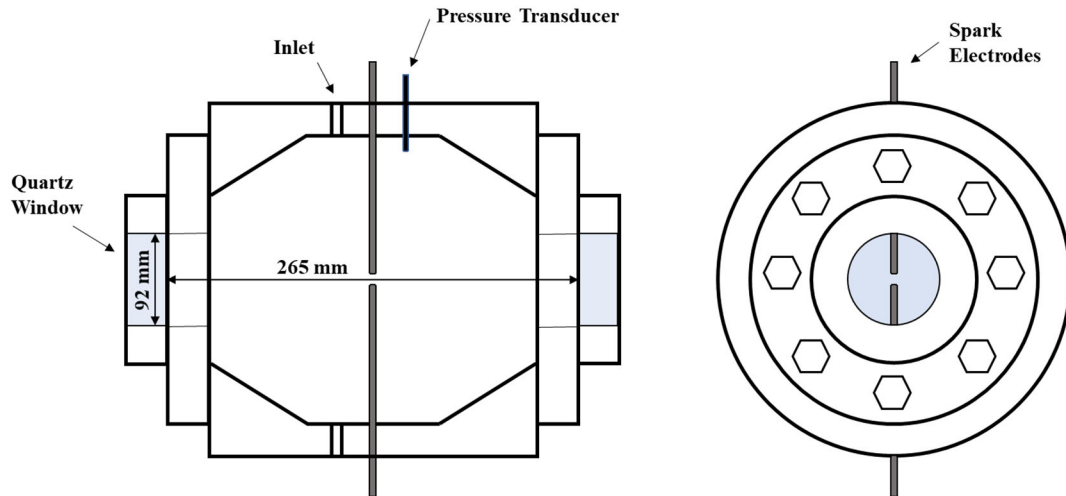
Figure 5.1 Schematic of the quasi-spherical combustion chamber

The experimental set up is shown in **Figure 2**. A high-speed camera (PHANTOM MIRO R310) was used to capture the expanding spherical flame front through a Z-type schlieren system with light source at 532 nm. The camera was operating at 15000 frame-per-second (fps) and 512 * 384 resolution. Prior to the experiments, a transparent grid with fixed-distance references was used to calibrate the camera. In this study, the calibration factor was 3.47 pixel/mm.

Figure 5.2 Schematic of the flame speed measurement experimental setup. Gas flow path is shown by blue lines; light path is shown by green lines

Prior to each test, a mixture was prepared in a stainless-steel tank using partial pressure method. The pressures of each components were measured using three pressure gauges for different ranges (VARIAN CDG GAUGE 0-100 torr, VARIAN CDG GAUGE 0-1000 torr, OMEGA PX309-050A5V 0-2586 torr / 0-50 psi). The mixture preparing started with evacuating the mixing tank using a vacuum pump (VARIAN DS102) until ≤ 0.2 torr. If HMDSO was included in the test, it was evaporated from a small stainless-steel canister connected to the mixing tank. Methane, air, and N_2 were then filled in the tank in that sequence. The pressure at each step was recorded to calculate the concentration of each species. A list of mixtures that has been tested in this experiment is shown in **Table 5.1**. The mixture was then stirred in the mixing tank for a minimum of 1 hour if not contained HMDSO and a minimum of 3 hours if contained HMDSO. Each mixture was used for filling in the combustion chamber twice.

A LabVIEW program is used to control the generation of trigger signal and receive data from a data acquisition system (National Instrument USB-6001). Once the signal was sent, the ignition box was triggered and then generated a voltage pulse which formed the spark at the center of the combustion chamber. The camera was triggered simultaneously and recorded 302 frames prior to the trigger and 2106 frames after the trigger. After ignition, the chamber was evacuated using the vacuum pump for approximately 30 mins, then the next test was started.

Table 5.1 Mixture information for flame speed measurement experiments

No.	Condition	Equivalence Ratio	HMDSO (ppm)	Fuel	Oxidizer	N_2/O_2 ratio
1	lean	0.824	0	Methane	O_2+N_2	3.787
2	lean	0.835	0	Methane	O_2+N_2	3.758
3	stoichiometric	0.998	0	Methane	O_2+N_2	3.770
4	stoichiometric	1.005	0	Methane	O_2+N_2	3.708
5	rich	1.219	0	Methane	O_2+N_2	3.759
6	rich	1.222	0	Methane	O_2+N_2	3.760
7	stoichiometric	0.999	261	Methane	O_2+N_2	3.747
8	stoichiometric	1.022	1013	Methane	O_2+N_2	3.762

5.2.2 Data Processing

The high-speed camera videos are processed through a MATLAB program developed by R. Ramesh et. al. [8]. The trigger signal is used to correlate the time between CCD camera video and the pressure data recorded by the LABVIEW program. Once the trigger position of the video has been determined, the previous 100 frames are averaged and used as the background. If the frames prior to the trigger signal were not recorded, the average of first two frames in which the flame expansion has not started will be use as background. For the frames containing the propagating flame fronts, the background will be extracted from the frames to identify the near-spherical flames by fitting a circle to the flame front using least squares minimization approach by Taubin et. al. [10]. The recorded circle radius data in the range of 10 mm to 30 mm is selected. It

is assuming that in this range, the flame stretch is minimal, and the pressure variation of the unburned gas is small enough that this flame can be treated as a freely propagating flame.

The radius data in the selected range is fitted with time by linear regression, and the coefficient (dR/dt) is used as the stretched burned flame speed S_b. The stretched unburned flame speed S_u is calculated using a mass conservation by Eq. 5.1, where ρ_b is the burned gas density and ρ_u is the unburned gas density.

$$S_u = \frac{\rho_b}{\rho_u} S_b = \frac{\rho_b}{\rho_u} \frac{dR}{dt} \qquad\qquad 5.1$$

To obtain the unstretched flame, a linear stretch model was applied [11]. The equation of the linear stretch model is

$$S_b = \frac{dR}{dt} = S_b^0 - L_b K \qquad\qquad 5.2$$

with

$$K = \frac{2S_b}{R} \qquad\qquad 5.3$$

where S_b^0 is the unstretched burned flame speed, L_b is the burned Markstein length, and K is the stretch rate. By applying a linear fitting of $S_b - K$ curve, the unstretched flame speed S_b^0 is obtained.

The primary sources of uncertainty in the current work were the repeatability of the experiments and the analytical procedure used to extract the flame speed from the imaging data. The uncertainty is estimated as less than ±30% (based on the scatter in the data) and will likely improve with the next generation of experimental procedures that can be developed using the results of this initial exploratory study.

5.3 Results and Discussion

Table 5.2 Flame speed measurement results

| No.	Phi	Cantera flame speed (cm/s)	Stretched flame speed 1 (cm/s)	Stretched flame speed 2 (cm/s)	Unstretched flame speed 1 (cm/s)	Unstretched flame speed 2 (cm/s)
1	1.005	36.82	31.94	32.33	35.20	35.40
2	0.998	37.26	31.87	33.99	35.02	37.12
3	0.835	29.09	25.75	25.84	27.55	27.10
4	0.824	29.48	24.24	26.14	25.89	27.17
5	1.219	31.43	30.44	32.89	34.34	36.46
6	1.222	31.17	33.83	34.27	37.44	36.38
7	0.999	37.52	30.95	31.88	33.32	34.55
8	1.022	37.65	30.39	31.97	33.55	34.61
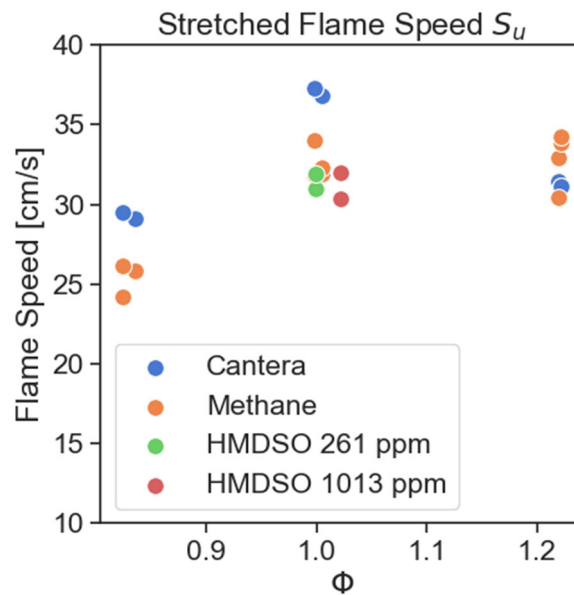
Figure 5.3 Stretched flame speeds results

The Cantera simulated flame speeds, measured stretched flame speeds, and unstretched flame speed obtained from linear stretch extrapolation model are listed in **Table 5.2** and plotted in **Figure 5.3** and **Figure 5.4**. As shown in **Figure 5.3**, there are discrepancies between the Cantera simulation results for freely propagating methane flame speeds and the experimental measurement results. These discrepancies indicate that the assumption that the flame stretch has minimal impact

is incorrect [12]. Therefore, a further unstretched flame speed need to be calculated. In addition, surprisingly, the HMDSO added to the methane flame has no or very small impact on the flame speed. Intuitively, HMDSO is a highly energetic species and will increase the total amount of energy released in the flame. In addition, the radicals in flame can be utilized by HMDSO to initiate its reactions, following by a production of intermediates from HMDSO reactions. Although the mechanism of HMDSO reaction is still not clear, it is expected that it has impacts on flame speeds due to radical consumption and formation.
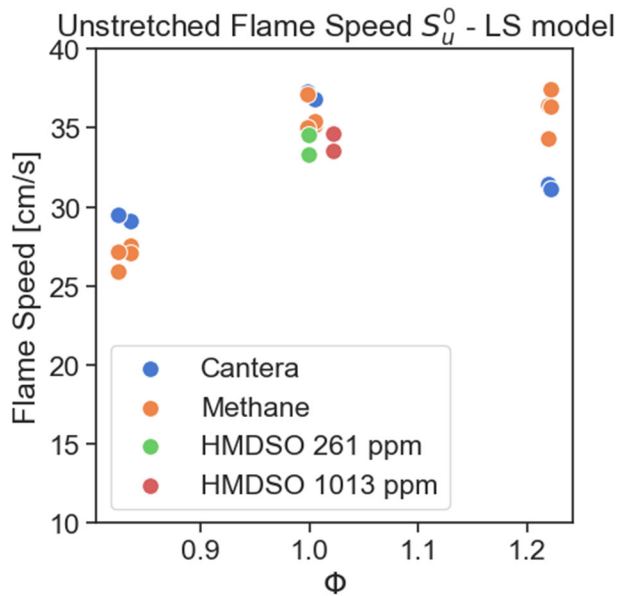
Figure 5.4 Unstretched flame speeds (cm/s) from linear stretch (LS) extrapolation model [9]

Unstretched flame speeds shown in **Figure 5.4** show an improved consistency between experimental data and Cantera simulation results for lean and stoichiometric conditions. The unstretched flame speeds for rich conditions exceed the simulated results largely. This could be due to a stronger stretch effect in the flames, which results in a non-linear relationship between S_b and K. Different stretch extrapolation models may reduce the discrepancy between experimental and simulated results under rich conditions, and is a recommendation for future work.
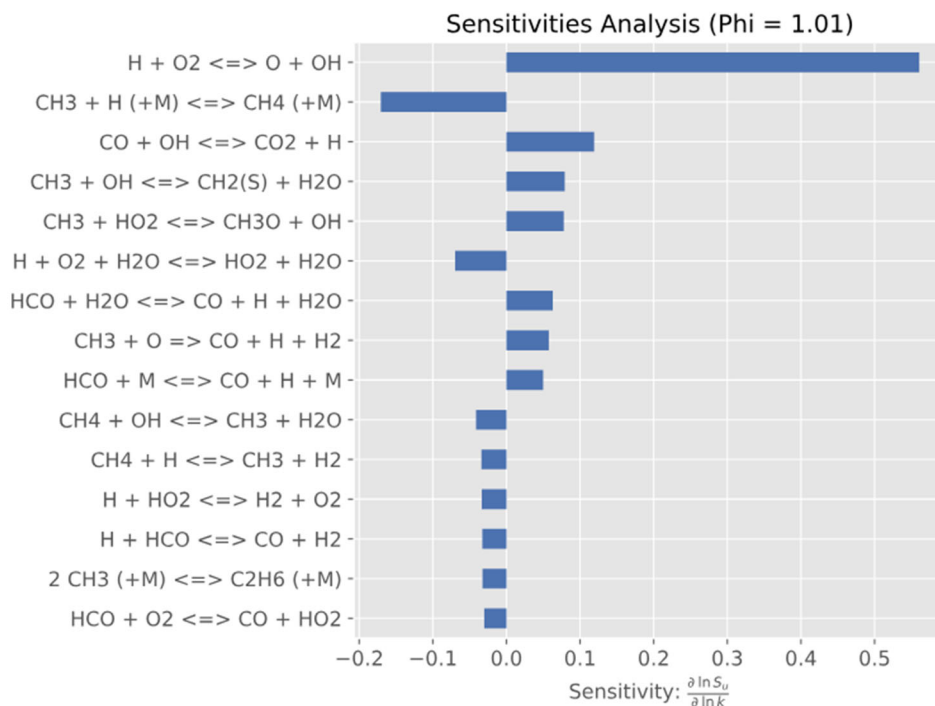
Figure 5.5 Sensitivity analysis results for methane flame speed (stoichiometric, $\Phi = 1.01$)

A sensitivity analysis for stoichiometric methane flame was made to identify the key reactions that have largest impact on the flame speed. Sensitivity analysis for other conditions were included in the supplementary materials in Appendix C:. The results show that reactions $H + O_2 \leftrightarrow O + OH$ and $CH_3 + H (+M) \leftrightarrow CH_4 (+M)$ has largest impact on the flame speeds. For the $H + O_2 \leftrightarrow O + OH$ reaction, through adjustments of the A factor, the impact on the simulated flame speed are shown in **Table 5.3**. By altering the A-factor in the kinetic rates equation by 20%, the resulting flame speeds vary about 10-12%. If the initial reactions of HMDSO includes H-abstraction by H radicals, or production of CH_3 radicals by Si-C bond breaking, it may consume the H radicals from the methane flame and increase the concentrations of CH_3 radicals, which will reduce the methane flame speeds. However, following HMDSO reactions are likely to generate more free radicals in the flame with a releasing of energy, which may further promote methane combustion. These two effects may cancel out at the experimental conditions studied.

Alternatively, the reaction chemistry for HMDSO may be so fast, it only affects the early times of the flame speed or it is possible that transport effects offset the HMDSO chemistry effects.

Table 5.3 Impact of A-factor adjustment on simulated methane flame speeds

Phi	A-factor from GriMech 3.0	Adjusted A-factor	Explain the adjustment	Flame speed without adjustment [cm/s]	Flame speed with adjustment [cm/s]	Flame speed changes [%]
1.01	2.65 e16	2.12 e16	20% smaller	37.48	32.87	-12.30%
1.01	2.65 e16	3.18 e16	20% larger	37.48	41.46	+10.62%

5.4 Conclusions

This work measured methane flame speeds with and without HMDSO in the methane-air mixture through constant pressure method in a quasi-spherical combustion chamber using a schlieren method. The results of this study show that around 1000 ppm HMDSO in the mixture potentially reduces stoichiometric methane flame speeds slightly, but the difference is within the variation of the data. From the sensitivity analysis, flame speed of methane is largely impacted by the reaction $H + O_2 \leftrightarrow O + OH$, which may be affected by the reactions of HMDSO. However, the HMDSO chemistry may be so fast, that the effects on the flame speed are not observable (i.e., due to the convolution with the spark initiation) or transport effects may dominate the HMDSO chemistry. It is unclear at this time why the flame speeds are unaffected. Additional experiments, beyond the scope of this work, may elucidate the reasons.

5.5 Citations

[1]   R. Schwind, Understanding the Combustion Chemistry of Siloxanes: Reaction Kinetics and Fuel Interactions, PhD Thesis, 2019.
[2]   Z. Wang, X. Zhang, L. Xing, L. Zhang, F. Herrmann, K. Moshammer, F. Qi, K. Kohse-Höinghaus, Experimental and kinetic modeling study of the low- and intermediate-temperature oxidation of dimethyl ether, Combustion and Flame. 162 (2015) 1113–1125.

[3] Y. Huang, H. Chen, A detailed reaction mechanism for hexamethyldisiloxane combustion via experiments and ReaxFF molecular dynamics simulations, Int J of Chemical Kinetics. (2023) kin.21698.

[4] D. Bradley, P.H. Gaskell, X.-J. Gu, Burning velocities, Markstein lengths, and flame quenching for spherical methane-air flames: a computational study, Combustion and Flame. 104 (1996) 176–198.

[5] F.N. Egolfopoulos, N. Hansen, Y. Ju, K. Kohse-Höinghaus, C.K. Law, F. Qi, Advances and challenges in laminar flame experiments and implications for combustion chemistry, Progress in Energy and Combustion Science. 43 (2014) 36–67.

[6] Z. Chen, On the accuracy of laminar flame speeds measured from outwardly propagating spherical flames: Methane/air at normal temperature and pressure, Combustion and Flame. 162 (2015) 2442–2453.

[7] M. Faghih, Z. Chen, The constant-volume propagating spherical flame method for laminar flame speed measurement, Science Bulletin. 61 (2016) 1296–1310.

[8] R. Ramesh, A. Vinod, F. Bisetti, M. Gamba, Analysis of uncertainties in the measurement of Markstein number and laminar flame speed of H2/O2/He mixtures at unity Lewis number in spherically expanding laminar flames, in: 2023.

[9] E.G. Groff, The cellular nature of confined spherical propane-air flames, Combustion and Flame. 48 (1982) 51–62.

[10] G. Taubin, Estimation of planar curves, surfaces, and nonplanar space curves defined by implicit equations with applications to edge and range image segmentation, IEEE Transactions on Pattern Analysis & Machine Intelligence. 13 (1991) 1115–1138.

[11] C.K. Wu, C.K. Law, On the determination of laminar flame speeds from stretched flames, in: Symposium (International) on Combustion, Elsevier, 1985: pp. 1941–1949.

[12] Z. Chen, M.P. Burke, Y. Ju, Effects of compression and stretch on the determination of laminar flame speeds using propagating spherical flames, Combustion Theory and Modelling. 13 (2009) 343–364.

Chapter 6 Conclusions and Recommendations for Future Work

6.1 Conclusions

The objective of this work was to advance the understanding of siloxanes in biogas including both their presence in waste gas and the understanding of the reaction pathways combustion chemistry. This goal was achieved through a combination of longitudinal studies involving waste management stakeholders and fundamental laboratory experiments focusing on trimethylsilanol (TMSO) and hexamethyldisiloxane (HMDSO).

Previous investigations on siloxanes in biogas were often confined to specific landfills and waste-water treatment sites, providing key insights on specific facilities. Such studies were leveraged to identify overall trends that characterize siloxane composition and amounts more broadly. As described in **Chapter 2**, the current work used multiple strategies, including stakeholder interviews, gas sampling from local landfill sites, and database establishment and analysis. These investigations were all original and new contributions, and have confirmed that the occurrence of siloxanes in biogas is not limited to certain regions, but is a worldwide concern. From the data analysis, it was observed that high concentrations of TMSO are associated with landfill gas and high concentrations of D4 and D5 are associated with sludge gas. Moreover, correlation analysis revealed that TMSO, D4 and D5 are reliable predictors of total siloxane concentrations. The relative silicon species concentrations showed consistent trends and the data can be used to understand the chemistry forming these silicon compounds in landfill and sludge gas. The results from this work also provide a basis for estimating the silicon concentrations when

speciation data are limited or vice versa. Such information can be used to develop on-site siloxane monitoring systems which can help address maintenance and operating concerns caused by high siloxane concentrations in biogas. In addition, the outcomes of this study provide a quantitative foundation for technology development to recover siloxanes from biogas sites (and determining if such recovery is technically and economically feasible) and to develop methods for siloxane abatement and mitigation that can improve energy recovery from waste water treatment facilities and landfills.

The analysis in **Chapter 2** was limited by the relatively small numbers of available siloxane data sources and the lack of some valuable information such as sampling date, sampling location, whether the gas samples were preprocessed, etc. It is suggested that siloxane concentrations at waste-to-energy sites should be more frequently monitored to improve the accuracy of the correlations, provide greater understanding if temporal variations are a concern, and other attributes that can reduce costs and improve outcomes of biogas applications. A publicly-accessible, global, online siloxane database including contributions from diverse sources can help address some of these limitations. The database described in this chapter could be used to establish such an online siloxane data sharing platform.

Chapter 3 - Chapter 5 presented the results of studies of the fundamental combustion chemistry of two canonical silicon species – TMSO and HMDSO. These compounds are both relevant due to their prevalence in biogas and due to the canonical structure of these silicon organic species. Previous studies of TMSO and HMDSO have shown discrepancies between experimental observations, theory and model predictions. The current work addresses needs for new insights into the oxidation and pyrolysis reactions controlling siloxane consumption in flames. In **Chapter 3** and **Chapter 4**, x-ray fluorescence (XRF) spectroscopy was successfully applied to high-fidelity

mixing and temperature measurements in MEDB flames. The experimental work not only validated the capability of measuring flow and temperature fields for gases with high concentrations of condensed phase species using XRF spectroscopy, but also provided valuable insights on the initiation of TMSO and HMDSO reactions. Pyrolysis and oxidation reactions were identified as both important in the flames studied, separated by different spatial locations, and XRF enabled high spatial fidelity measurement in both regions. The results showed the reactions of TMSO and HMDSO were initiated in a low temperature region, which was conjectured as due to H and OH radicals from methane flames transported to the flow of the siloxanes. Recent complementary work indicates the hypothesis of H-atom transport is correct [1]. Direct gas sampling results provided further information that TMSO is produced in HMDSO flames. The observation of TMSO is contrary to a recent reaction mechanism for HMDSO proposed by Chen et al. [2]. Thus, the current work provides important new data to guide needed development of new HMDSO reaction theory that correctly reproduces the new experimental observations.

To further investigate perturbation of methane reactions by HMDSO chemistry, in **Chapter 5** laminar flame speed experiments were conducted using a spherical laminar flame speed apparatus. This is the first work studying the impact of siloxanes on methane flame speeds. The results showed the addition of HMDSO had limited impact on methane flame speeds, indicating transport effects or faster combustion chemistry associated with HMDSO are impacting these measurements. The results provide an important foundation for future studies that reduce the uncertainties and improve the accuracy of siloxane flame speed measurements.

In summary, this work has improved the understanding of siloxanes including their worldwide presence and critical patterns of observation in biogas and the combustion chemistry of siloxanes. The findings provide a foundation to develop new strategies for siloxane resource

recovery, mitigation of siloxane impacts on energy equipment and insights into the fundamental chemistry that has value in science and engineering applications of siloxanes. For example, the data can be used to understand and compare silicon bonding with carbon bonding of species with analogous chemical structures. Chemical synthesis methods that use siloxanes as key reactants can also benefit from the reaction theory developed (both global and elementary) from the current work. The work may also improve outcomes for the waste-to-energy industry and other industries associated with siloxane combustion, including functionalized silica.

6.2 Recommendations for Future Work

While the current work provides new insights into the reaction chemistry important during combustion of siloxanes, further fundamental studies can refine and improve the hypotheses on which reaction pathways are active and important. Consistent reaction paths of siloxane compounds can be developed and validated through integration of diverse experimental methods and conditions. For example, the XRF results presented in this thesis indicate low temperature reactions are initiating consumption of siloxanes in the flames studied, potentially through H-abstraction reactions with H, OH and HO_2 radicals. This hypothesis has been initially verified by planar laser induced fluorescence (PLIF) [1]. Understanding the role of radicals in hydrocarbon and siloxane combustion chemistry is critical. PLIF and other diagnostics can be applied to resolve the radical distributions and quantitively analyze the consumption rate of radicals in the initial reaction region of TMSO and HMDSO. In addition to radical studies, identifying and quantifying siloxane intermediates is urgently needed to propose and validate siloxane oxidation pathways. Burner-based studies enable gas sampling and spectroscopy measurements to obtain spatially resolved intermediate data, as do rapid compression facility experiments using fast gas sampling. However, particles may be problematic in these experiment as gas sampling analytics like gas

chromatography are sensitive to solid phases. Removing particles from the gas samples without largely affecting the intermediate concentrations could be challenging and should be well considered and addressed in any sampling experiments.

Finally, the recent advances in computational capabilities provide new opportunities for quantitative reaction mechanism development. Examples include Stochastic Nanoparticle Simulators (SNAPS) [3], reactive force-field (ReaxFF) [4] and Automated mechanism generators such as KinBot [5] and Reaction Mechanism Generator (RMG) [6]. Such methods could facilitate the identification of potential reaction pathways and transition states. A combination of computational methods with various experimental data can dramatically improve the development of accurate mechanisms for siloxane combustion and the hierarchal chemistry of silicon compounds.

6.3 Citations

[1]   K. Kim, M. Hay, Q. Meng, M.S. Wooldridge, W.D. Kulatilaka, R.S. Tranter, Hexamethyldisiloxane pyrolysis: probing the importance of H-atom initiation by femtosecond two-photon LIF, Submitted to PROCI (2023).
[2]   Y. Chen, H. Chen, J. Wang, Y. Huang, Chemical kinetics of hexamethyldisiloxane pyrolysis: A ReaxFF molecular dynamics simulation study, International Journal of Chemical Kinetics. 54 (2022) 413–423.
[3]   J.Y. Lai, P. Elvati, A. Violi, Stochastic atomistic simulation of polycyclic aromatic hydrocarbon growth in combustion, Physical Chemistry Chemical Physics. 16 (2014) 7969–7979.
[4]   T.P. Senftle, S. Hong, M.M. Islam, S.B. Kylasa, Y. Zheng, Y.K. Shin, C. Junkermeier, R. Engel-Herbert, M.J. Janik, H.M. Aktulga, T. Verstraelen, A. Grama, A.C.T. van Duin, The ReaxFF reactive force-field: development, applications and future directions, Npj Comput Mater. 2 (2016) 15011.
[5]   R. Van de Vijver, J. Zádor, KinBot: Automated stationary point search on potential energy surfaces, Computer Physics Communications. 248 (2020) 106947.
[6]   M.S. Johnson, X. Dong, A. Grinberg Dana, Y. Chung, D. Farina, R.J. Gillis, M. Liu, N.W. Yee, K. Blondal, E. Mazeau, C.A. Grambow, A.M. Payne, K.A. Spiekermann, H.-W. Pang, C.F. Goldsmith, R.H. West, W.H. Green, RMG Database for Chemical Property Prediction, J. Chem. Inf. Model. 62 (2022) 4906–4915.
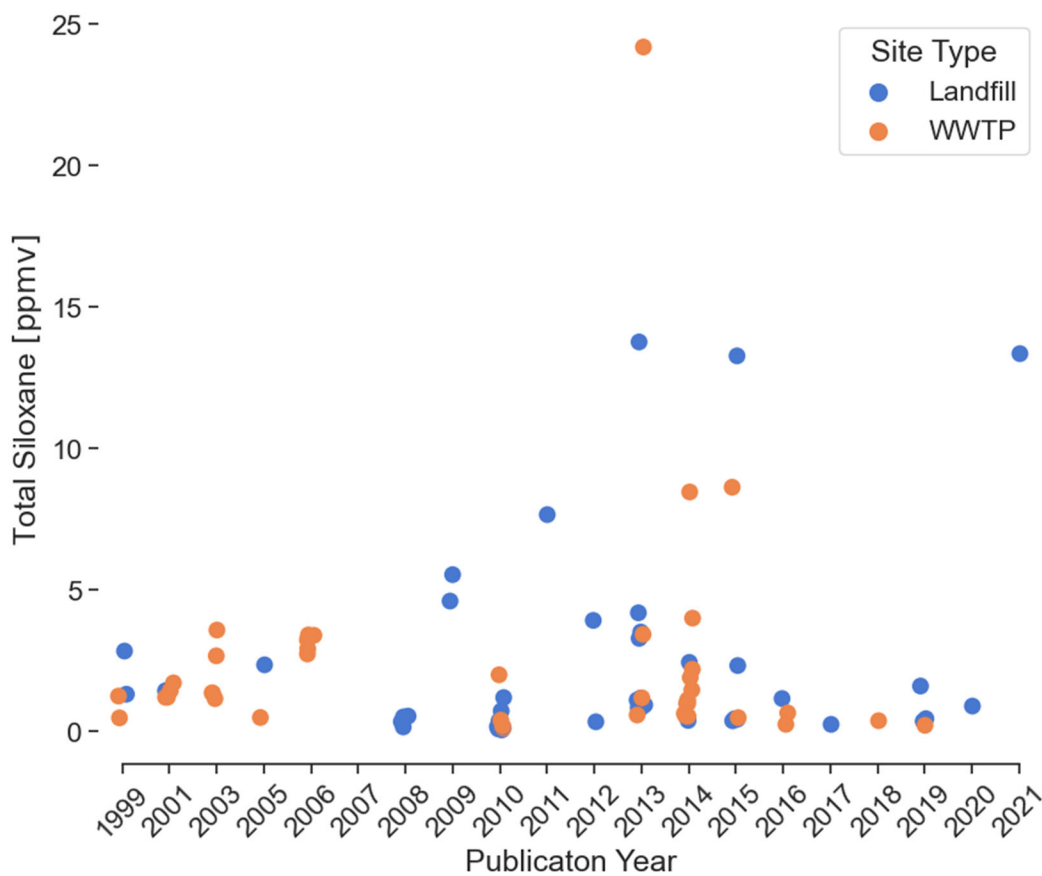
Appendices

Appendix A: Siloxane in Biogas Analysis Results in Other Units
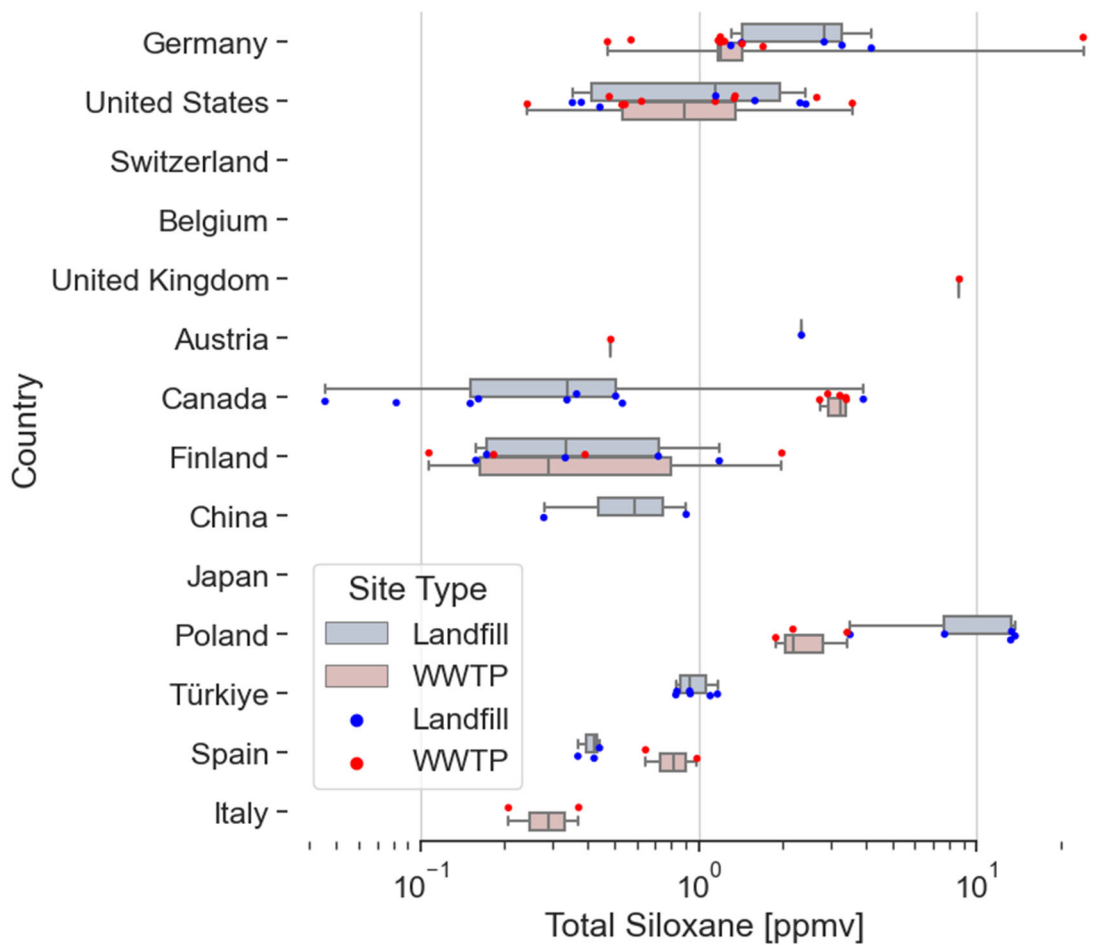
Appendix Figure A.1 Comparison of total siloxane levels by country in gas samples from landfill and WWTPs (units: ppmv).
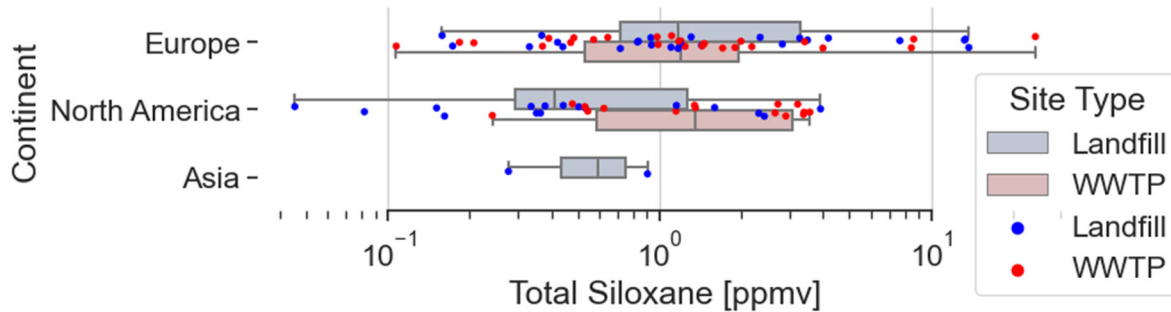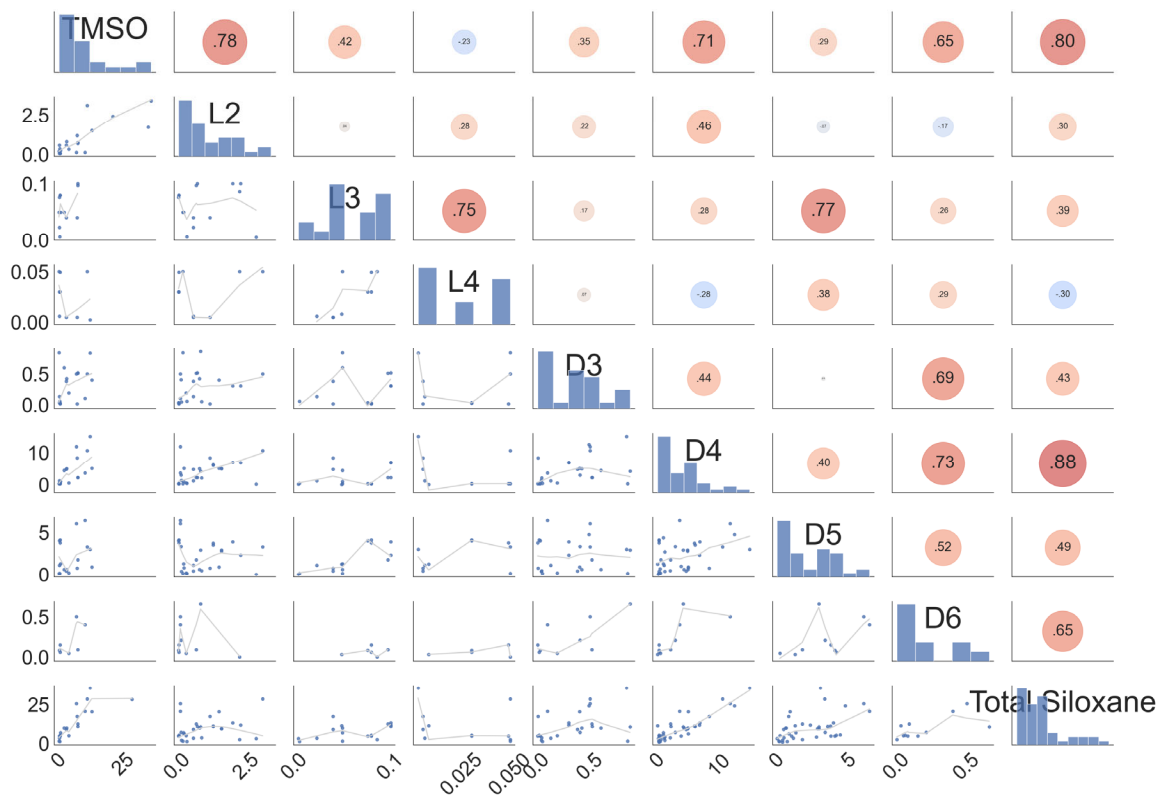
Appendix Figure A.2 Comparison of total siloxane levels by continent in gas samples from landfill and WWTPs (units: ppmv).
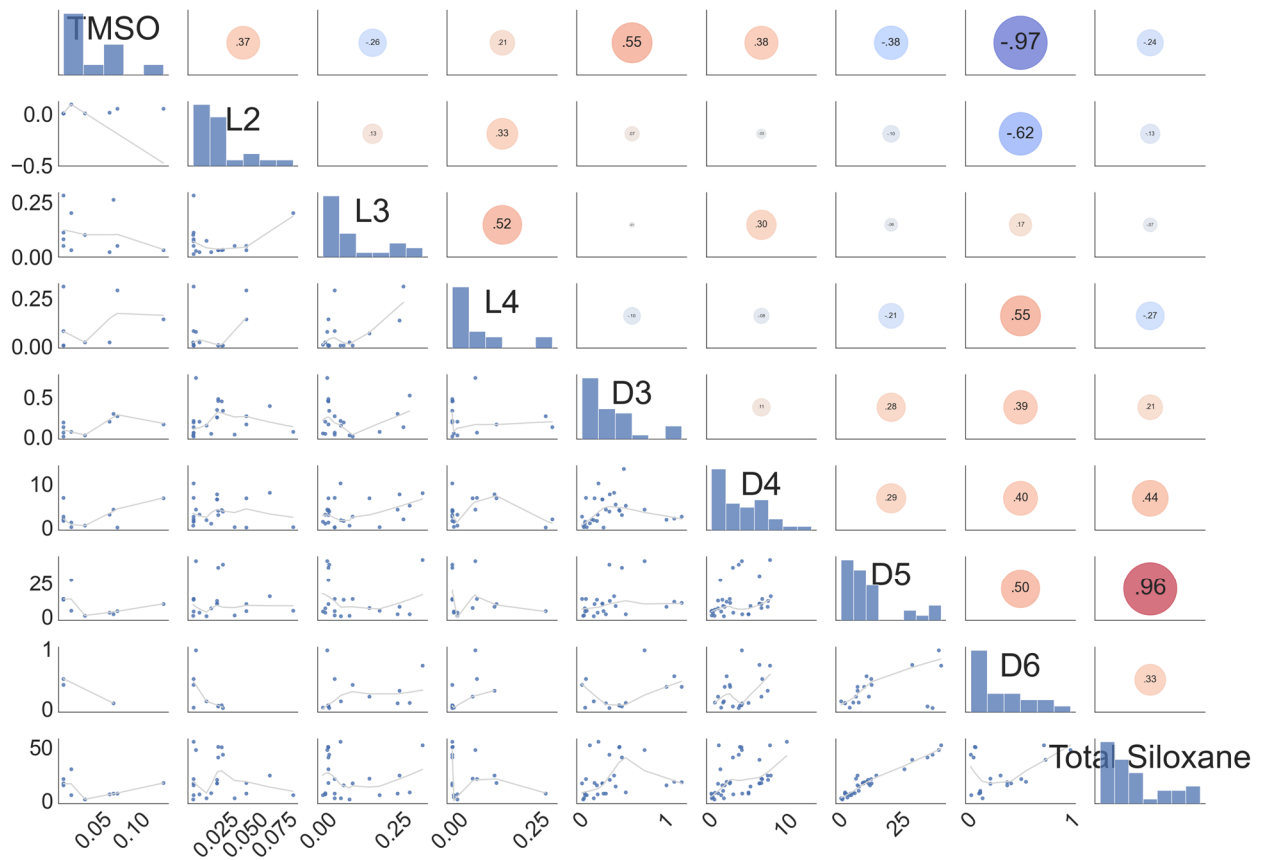

Appendix Figure A.3 Reported total siloxane concentrations based on the publication year of the report (units: ppmv).
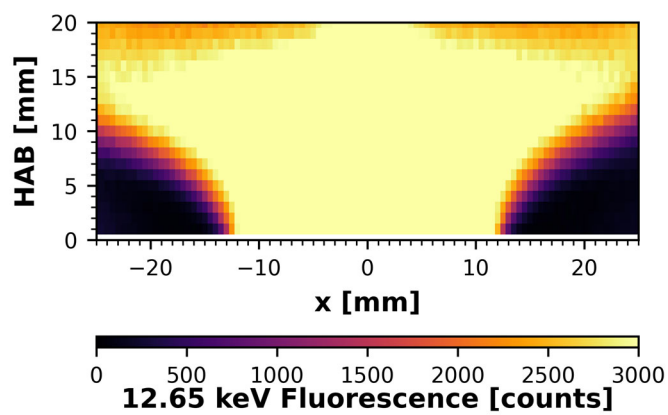
Appendix Figure A.4 Correlations between each siloxane species and the total siloxane concentration in landfill gas (units: mg/m^3).

Appendix Figure A.5 Correlations between each siloxane species and the total siloxane concentration in sludge gas (units: mg/m3).

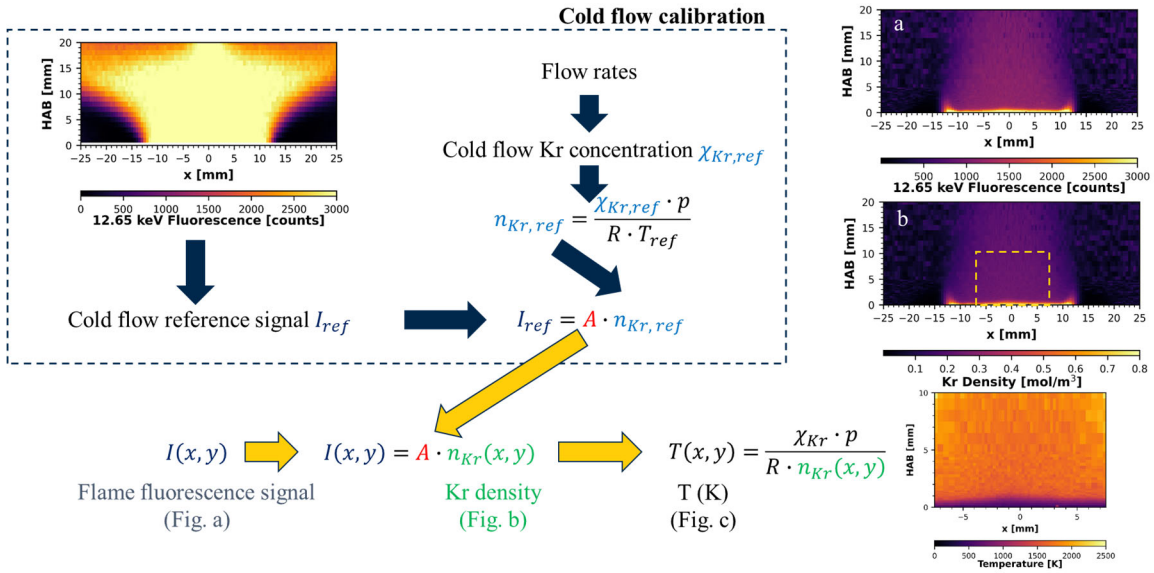# Appendix B: X-ray Fluorescence Measurement Supplementary Materials

Appendix Figure B.1 Cold flow (T = 298 K) intensity data highlighting the region containing Kr where measurements are possible.
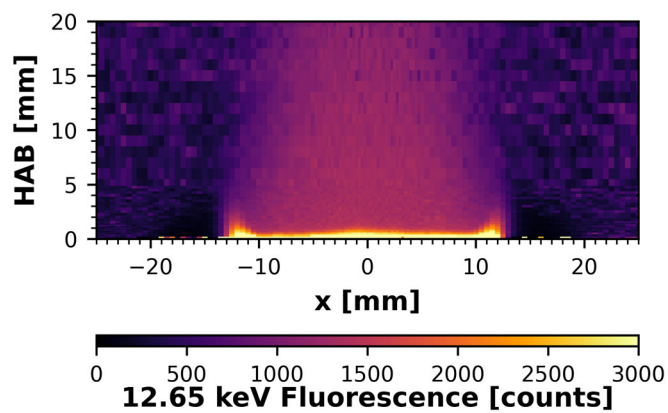
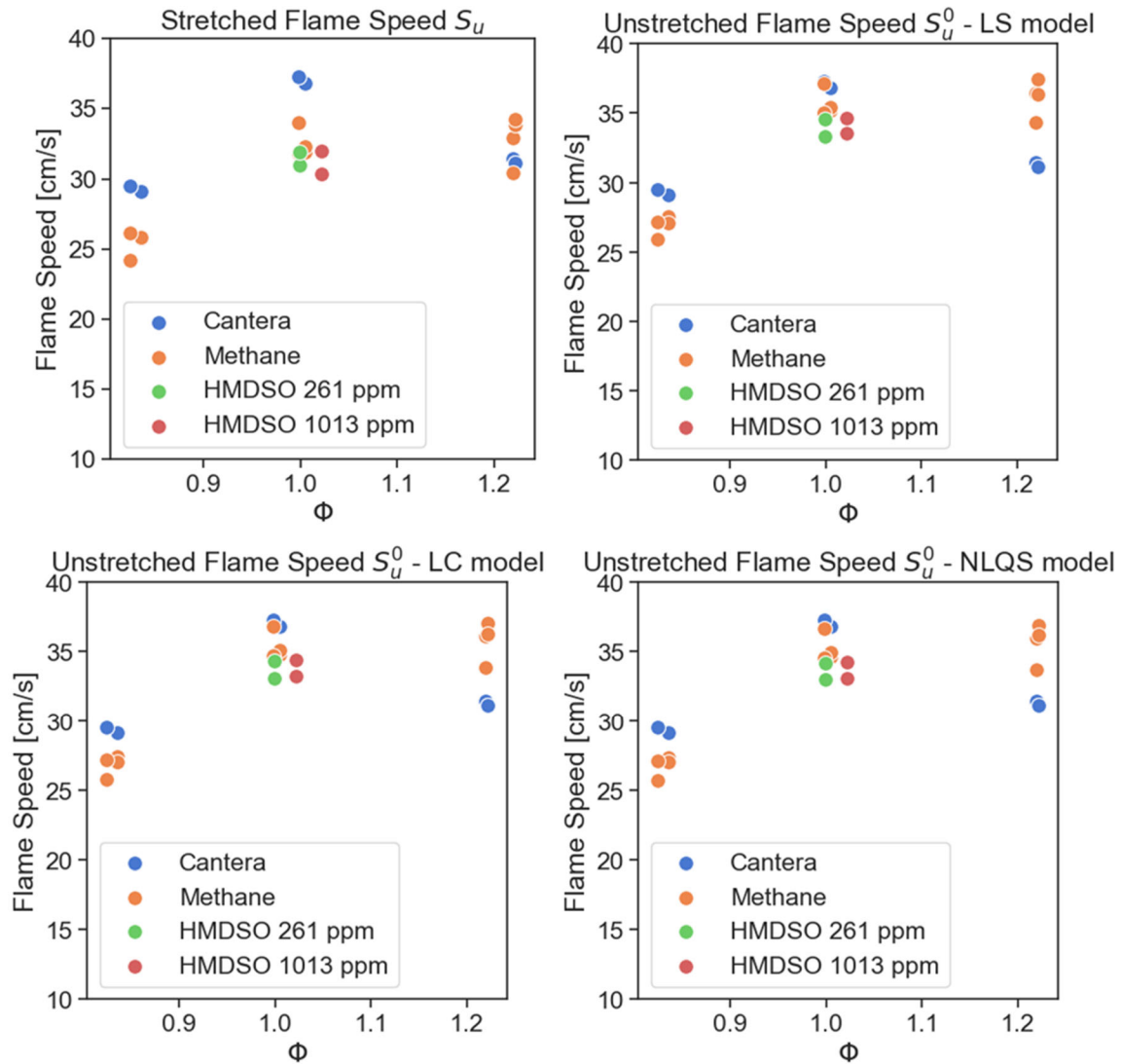**Appendix Figure B.2** Fluorescence signals of flame with no central tube flow.
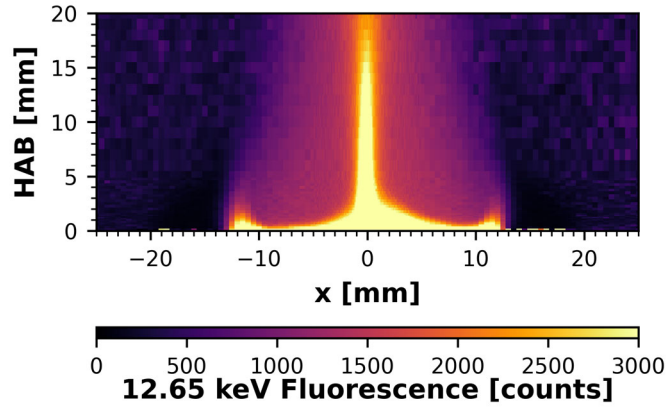
**Appendix Figure B.3** Fluorescence signals of flame with central tube flow.


Appendix Figure B.4 XRF data analysis procedures

Appendix C: Flame Speeds Measurement Supplementary Materials

Appendix Figure C.1 Flame speed measurment results before and after applying flame stretch extrapolation models. LS - Linear stretch model; LC – Linear curvature model; NLQS – Non-linear quasi-steady stretch extrapolation model.
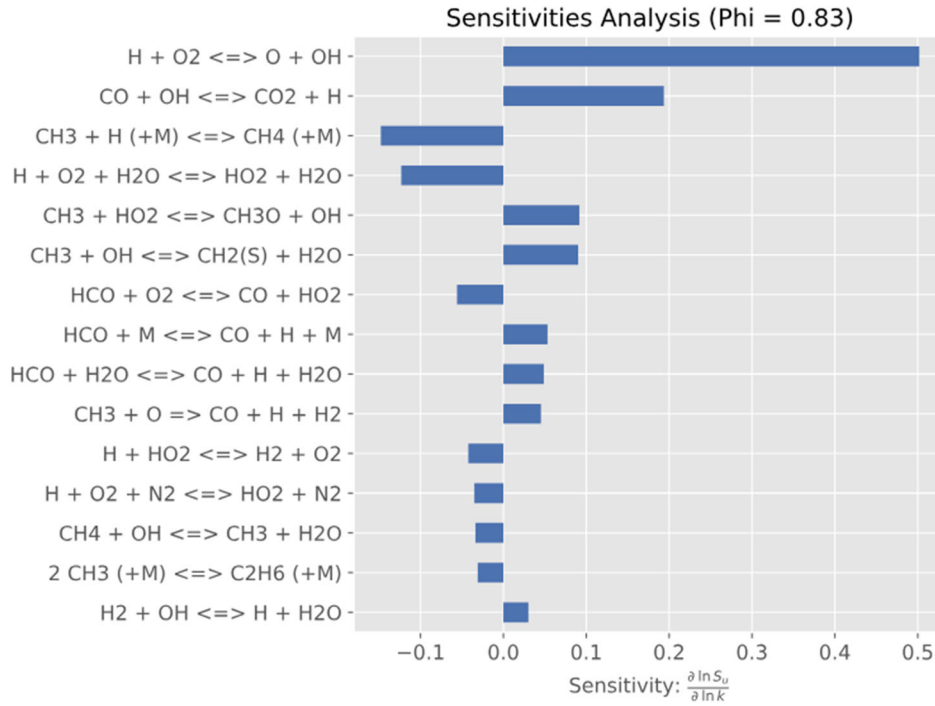
Appendix Figure C.2 Sensitivity analysis results for methane flame speed (lean, Φ = 0.83)
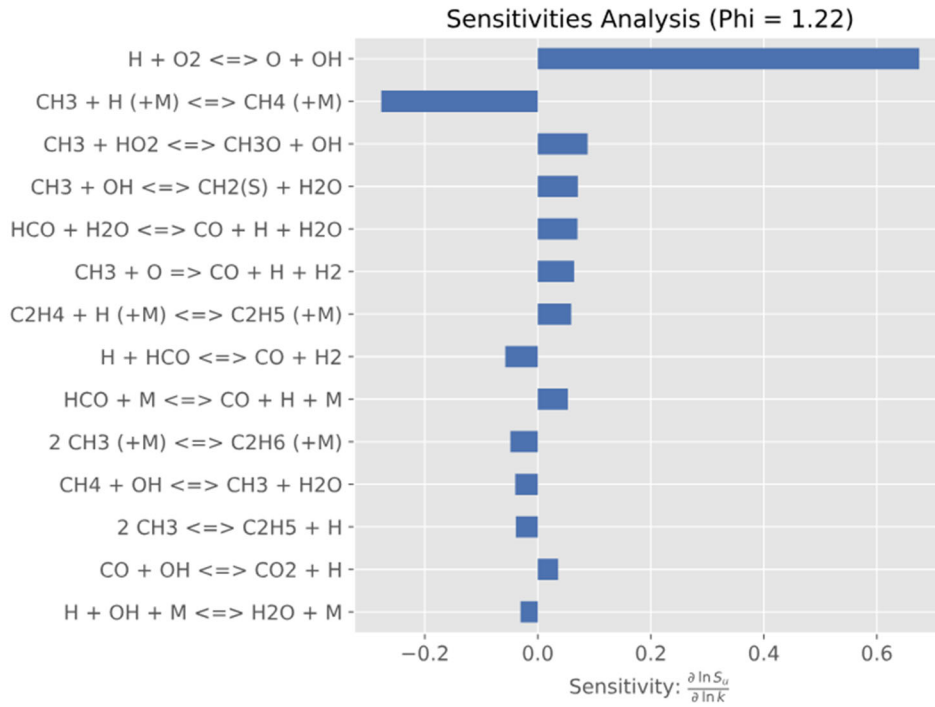
Appendix Figure C.3 Sensitivity analysis results for methane flame speed (rich, Φ = 1.22)